University of Alberta

Nanomechanical Torque Magnetometry and AC Susceptometry of Mesoscopic Magnetic Structures

by

Joseph Edwin Losby

A thesis submitted to the Faculty of Graduate Studies and Research
in partial fulfillment of the requirements for the degree of

Doctor of Philosophy

Department of Physics

Spring 2014
Edmonton, Alberta

Abstract

Nanomechanical torque magnetometry is emerging to become one of the most highly-sensitive methods for measuring magnetostatic interactions in mesoscopic magnetic materials. Here, advances in torque magnetometry are offered for the probing of new physics and extending the functionality of the devices to explore phenomena previously inaccessible using the technique. In early studies, fully magnetic cantilevers were fabricated and the magnetization switching along the length of the devices was mechanically characterized using a simple model to describe the cantilever deflection under the influence of a magnetic torque. Torsional magnetometers were later primarily investigated due to their high responsivity to a magnetic torque applied along the torsion rod axis. A method for the calibration of a torque magnetometer's displacement and magnetic moment sensitivity, through the detection of thermomechanical noise is offered. A vector-based nanomechanical transduction scheme was later developed to investigate the pristine internal three dimensional magnetization present in a micromachined yttrium iron garnet disk. Finally, a new method for the simultaneous detection of DC magnetization and low-frequency AC susceptibility was developed, bringing nanomechanical magnetometry toward the realm of magnetization dynamics.

Acknowledgements

I would like to thank my collaborators (many of whom have become good friends) for their contributions and sharing of knowledge: Miro Belov, Jacob Burgess, Shawn Compton, John Davis, Zhu Diao, Fatemeh Fani Sani, Tayyaba Firdous, Alastair Fraser, Dylan Grandmont, Chris Holt, Wayne Hiebert, Ning Liu, David Mitlin, Lance Parsons, Vincent Sauer, Oleksiy Svitelskiy, Doug Vick, and Jocelyn Westwood.

I am grateful for the technical, support, and administrative staff that have helped me immensely over the years: Lynn Chandler, Sarah Derr, Eric Flaim, David 'Flying Kick' Fortin, Peng Li, Marek Malac, Don Mullin, Greg Popowich, and Tony Walford.

Although there are too many names to list here, I'd like to offer my gratitude for my friends and family - especially Mom, Dad, and Lisa. Thank you for the support and good times.

I am indebted to the taxpayers of Canada for allowing me to conduct great research in a great country.

Finally, I would like to offer my sincere thanks to my supervisor and mentor, Mark Freeman, for offering a clean canvas on which to conduct my research. The freedom I was offered was extraordinary and enriching. Among many things, Mark has taught me to be patient with science and helped me gain an appreciation for many scientific fields outside of condensed matter physics.

Contents

Appendices

List of Tables

List of Figures

List of Symbols

$\mathcal{H}$ The Heisenberg exchange Hamiltonian 14

μ_0 The magnetic permeability of free space 12

ω_1 Fundamental resonance frequency of a mechanical oscillator 8

ω_c Angular drive frequency 8

$\phi n(x)$ The shape function of the nth mode of a mechanical beam, where x is along the length 41

ρ Mass density 7

a_n Amplitude coefficients of the mechanical displacement amplitude 8

c_n The damping coefficient in a mechanical oscillator 41

$f(x)$ Force distribution across a mechanical resonator 8

f_0 Uniform force distribution across a mechanical resonator 8

k_B The Boltzmann constnat 10

k_{eff} The effective mechanical spring constnat 10

k_n The spring constant of a mechanical oscillator 41

m_n The modal mass of a mechanical oscillator 41

m_x, m_y, and m_z The direction cosines of magnetization 14

$p_n(x,t)$ The time-dependent force distribution along the length x of a cantilever 40

$u(x,t)$ Time-dependent displacement of a mechanical oscillator 7

$u_n(x)$ Eigenfunctions of the mechanical displacement amplitude 8

AFM Atomic force microscope/microscopy 11

BOE Buffered oxide etch solution 29

BOx The buried oxide layer in an SOI wafer 58

EBL Electron beam lithography 25

FIB Focused ion beam 25

FMRFM Ferromagnetic resonance force microscope/microscopy 11

HSQ Hydrogen silsesquioxane, a high-resolution negative tone electron beam resist 27

IPA Isopropyl alcohol 29

LLG Landau-Lifshitz-Gilbert 18

MEMS Microelectromechanical Systems, mechanical devices with functional structures in the micrometer range 6

MFM Magnetic force microscope/microscopy 11

MRFM Magnetic resonance force microscope/microscopy 11

NEMS Nanoelectromechanical Systems 1

NMP N-Methyl-2-pyrrolidone 134

Permalloy $Ni_{80}Fe_{20}$, A soft magnetic alloy often used in micromagnetic investigations 2

PMMA Poly(methyl) methacrylate, a polymer used as a positive tone electron beam resist 27

RF Radio frequency 28

RIE Reactive ion etch 28

rms root-mean-square 3

SEM Scanning electron microscope 28

Si Silicon 11

SOI Silicon-on-insulator wafer architecture 28

SQUID Superconducting quantum interference device, a highly sensitive magnetometer 11

SU-8 A biologically compatible negative tone electron beam resist 27

TEM Transmission electron microscope 30

CHAPTER 1

Introduction

1.1 Organization of this Thesis

The work described in this Thesis is organized around advances in nanomechanical torque magnetometry. These were accomplished by virtue of a fortuitous convergence of advancements over recent years in the various fields that together form the core of research herein. These are: the birth of the field of nanomechanics (the advent of nanoelectromechanical systems, NEMS); ever-advancing nanofabrication techniques; and breakthroughs in micromagnetism which give rise to continuing technological demand. This confluence has yielded the amazing capability to fabricate nanomechanical magnetometers for the sensitive characterization of single, mesoscopic magnetic elements. The mechanical oscillators can be magnetically active through their volume, or non-magnetic structures that have a means of rigidly housing the magnet.

The key interaction in torque magnetometry is the torque that magnetic moments in a material experience due to an external field. This torque, transferred to the mechanical subsystem, causes a measurable mechanical deflection. The exquisite sensitivities of nanomechanical resonators allow for the investigation of phenomena owing to local magnetic inhomogeneities that are often blurred by traditional array-based measurements (such as magnetic domain

wall or vortex pinning), which is necessary for realizing their optimal implementation in future spintronic devices. In this Thesis, nanoscale mechanical magnetometers were fabricated for the investigation of various quasistatic magnetic processes (domain wall motion in cantilevers, magnetic vortex motion with applied field, etc.). New experimental techniques were also developed to extend the functionality of nanomechanical torque magnetometers. They are the vector magnetometry method for probing mesoscale magnets with three-dimensional structure, and a frequency-mixing technique for the simultaneous measurement of DC magnetization and low frequency AC susceptibility. The latter opens the path to a broadband detection of magnetization dynamics.

The main body of this Thesis is divided into chapters that chronologically present published and soon-to-be submitted (for peer review) results (Chapters 3 through 6). As it was the case that further interesting results were found and extra analyses performed, which either couldn't fit within the publication length limitations or were done post-publication, additional relevant information has been appended to the final sections of the Thesis.

In the first Chapter, an introduction to nanomechanics and micromagnetism, in the context of nanomechanical torque magnetometry, is offered. Also included in this Chapter is additional background information for the topics covered in Chapters 3 through 6 (dissipative processes in nanomechanical systems and AC magnetic susceptometry).

A discussion of nanofabrication and experimental methods is given in Chapter 2.

Described in Chapter 3 is the fabrication and characterization of nanoscale permalloy ($Ni_{80}Fe_{20}$) cantilevers magnetic through their entire volume. Domain switching along the length of the cantilevers was shown through the hysteresis in their magnetization curves. A simple finite element model was proposed, which modelled the deflection of the cantilever beam as a straight, two dimensional magnetic domain wall propagating along the length. The experimental results were also compared to the transformation of the Landau-Lifshitz-Gilbert based simulation results, through the model, to a proportional

mechanical deflection.

A method to calibrate the thermomechanical noise of a nanomechanical torque magnetometer with a root-mean-square (rms) mechanical deflection amplitude is discussed in Chapter 4. This ultimately allows for the calculation of the displacement and magnetic moment sensitivities of the device.

In Chapter 5 are the results from a culmination of studies involving the investigation of a single crystal, mesoscale, yttrium iron garnet (YIG) disk with cubic magnetocrystalline anisotropy. One of the motivations behind this study was to study the effects of geometric confinement in monocrystalline micromagnets. However, due to the templated epitaxial techniques that are required for YIG (and most single-crystal magnet) growth, it is very difficult to localize and shape the magnet on a nanomechanical resonator. This was overcome with the use of three-dimensional focused ion beam milling of a micromagnetic disk (600 nm in radius and 500 nm tall) from a bulk crystal of YIG, and nanomanipulation onto a mesoscale mechanical resonator. The disk exhibits a rich three dimensional magnetization texture comprising of a magnetic vortex extending through its thickness. A vector nanomechanical magnetometry technique was developed to characterize the in- and out-of-plane components of magnetization.

In Chapter 6, a new method for the simultaneous detection of DC magnetization and low-frequency AC susceptibility is developed using multifrequency nanomechanical detection. The resonator is driven simultaneously by two orthogonal AC magnetic fields, which have sum or difference frequencies at its mechanical resonance. The resonator, acting effectively as a signal mixer, yields information of the magnetic susceptibility and its higher order harmonics.

Concluding remarks and a discussion of future prospects for the exciting area of research presented in this Thesis are provided in Chapter 7.

The Appendices contain results that are not yet published and supplemental material. These include a proposal of a multimodal mechanical magnetometry

technique and an examination of the pristine nature of the YIG disk, which shows no signatures (within our experimental resolution) of Barkhausen steps in the magnetization curve.

1.2 Introduction

The probing of natural forces through their interaction with mechanical objects is ubiquitous through our cultural and intellectual evolution. Perhaps the earliest, and most obvious, of such instruments is the simple mass-weighing scale. The earliest scales date to 2000-3000 BC in the civilizations occupying the Indus river valley and Egypt, where their application was implemented mainly to benefit commerce [1]. Another ancient mechanical tool, the magnetic compass, was sculpted from the "magical" lodestone (rich in magnetite, iron oxide Fe_3O_4), which was likely magnetized by the large currents induced during lightning-strike events [2]. The earliest accounts of their use date to 400 BC China, initially for spiritual or religious purposes. Resembling a spoon, the compass would align with the Earth's magnetic field, dictating the spatial direction for one to orient in order to harmonize their lives. Ancient streets and tombs, for example, were found to be aligned in the direction of the compass needle [3]. The magnetic compass would soon afterwards become a seafaring navigational tool, greatly altering the course of our history.

Through the history of the sciences mechanical instruments were indispensable for the discovery and investigation of fundamental physical concepts. Perhaps one of the most commonly used of such instruments is the torsion spring or balance, which basically consists of a thin fibre or rod, usually under tension, that is allowed to twist along its axis. Attached to the torsion fibre or rod is some suitable medium that is allowed to experience a force. In the case of Charles Coulomb's famous experiment, a charged ball attached to the torsion fibre was brought close to another charged ball. He deduced, through knowledge of the relative charges on each ball and the angle of twist in the fibre, the expression for the force between two charged bodies, now known as

Coulomb's Law [4]. Henry Cavendish performed experiments in the late 1790s using a torsion balance to measure the interaction between two massive bodies, which lead to the determination of the first accurate value for the universal gravitational constant [5].

The torsion spring was also the basis behind the experiments of Samuel Barnett, who observed the change in the magnetization of a suspended steel rod when it was rotated (Barnett effect) [6]. The reverse effect (Einstein-de Haas) was demonstrated by Albert Einstein and Wander Johannes de Haas, where a rod suspended on a torsion spring experienced a mechanical torque as a result of a change in magnetization [7].[1] Both experiments sought to find the link between the magnetic moment of an electron and the associated angular momentum, which is now known as the magnetomechanical ratio. The original Einstein-de Haas experiment apparatus is the basis and one of the earliest scientific uses of the now commonly employed torque magnetometer. The instrument is, in essence, a torsion rod with a sample of interest affixed at one end which is allowed to rotate in an external magnetic field. The response is measured through the deflection of a light source reflected off a mirror attached to the torsion rod.

The basic concept behind the operation of all the aforementioned instruments is elementary: a rigid arm under a force load (or in the case of magnetism, a pure torque) undergoes a measurable mechanical deflection. With miniaturization to the micro- and nanoscale they continue to be extremely powerful probing tools, as has been observed through the developments of atomic/magnetic force microscopy, magnetic resonance force microscopy, and as the basis for the nanomechanical torque magnetometry measurements described in this Thesis.

[1] This experiment is believed to be the only one Albert Einstein ever conducted.

1.3 Nanomechanics

In the late 1990s the field of nanoelectromechanical systems (NEMS) started to gain significant attention with the promise of low power consumption devices, unmatched force-detection sensitivities, on-chip integration, and the prospect of probing fundamental physics through mechanical transduction [8, 9, 10, 11, 12, 13]. The benefits of the scaling-down of the dimensions of mechanical devices come from their higher fundamental resonance (operating) frequencies and higher responsivities (because of their extremely low spring constants). Nanomechanical systems (usually defined as those with functional structures with dimensions in the deep submicrometer range), owe their inception in part to the advancements made in micromachining techniques that began in the mid to late 20th century for the integration of microelectromechanical devices with semiconductor architectures. MEMS (microelectromechanical systems, [14, 15]) devices continue to have numerous applications. Some examples include their use as accelerometers and gyroscopes in automobiles and cellular phones, pressure sensors, biological sensors, micro-mirrors for display technologies and optical switching. For many of these applications, especially those that involve sensing, a further scaling down of their dimensions will increase detection sensitivities. Some amazing milestones have been reached in recent years that continue to test the limits of nanomechanical detection. For mass sensing, where mechanical frequency shifts due to mass loading are measured, it was shown that measurements of masses of individual atoms are possible [16, 17]. Within a few years, yoctogram-scale (1 yg = 10^{-24} g) resolution, which is on the order of the proton mass, was achieved using a vibrating carbon nanotube [18]. Around the same time, the magnetic resonance signal from a single electron was observed for the first time, using force detection [19]. Single spin detection and control was also shown to be capable using nitrogen vacancy centers induced in mechanical resonators [20, 21]. From the mid to late 2000s, researchers began to using clever optical cooling (to suppress quantum back-action) techniques to bring resonators to their quantum mechanical limit (and beyond) [22, 23, 24]. Exciting current

research, which involves the coupling of qubits (quantum mechanical 'bits') to devices, allows for the study of quantum mechanical interactions using relatively 'macroscopic' objects [25, 26]. Optomechanical transduction, where optical gradient forces couple to objects and cause them to mechanically deflect, has proven to be amongst the most sensitive. It is the author's belief that the future of nanomechanical transduction will likely involve this route [27, 28, 29] as will be discussed in more detail in the concluding chapter of this Thesis.

In the following subsections, a general description of the analytical theory behind the motion of a driven, damped nanomechanical oscillator is given (in order to introduce material presented in Chapters 3 and 4), along with discussion of dissipation mechanisms that impose limits on the performance of the device.

1.3.1 Analytical theory of damped, driven motion in nanomechanical resonators

Many nanomechanical structures are based on simple geometries such as cantilevers or doubly-clamped beams. When one dimension (length) of the beam is much larger than the other two (width and thickness), the well-established Euler-Bernoulli theory allows for the treatment of these systems as one dimensional elastic beams [30, 31].

The schematic of a representative cantilever is shown in Fig. 1.1. Limiting its flexural motion to one dimension, the equation of motion for an elastic beam is

$$\rho A \frac{\partial^2 u(x,t)}{\partial t^2} + EI \frac{\partial^4 u(x,t)}{\partial x^4} = f(x) e^{-i\omega_c t} \tag{1.1}$$

where ρ is the mass density, A is the cross-sectional area, E is Young's modulus, and I is the areal moment of inertia perpendicular to the central beam axis. $u(x,t)$ is the time-dependent displacement of the beam, with a maximum value at $x = L$ (the free end of the beam, L is the beam length), while experi-

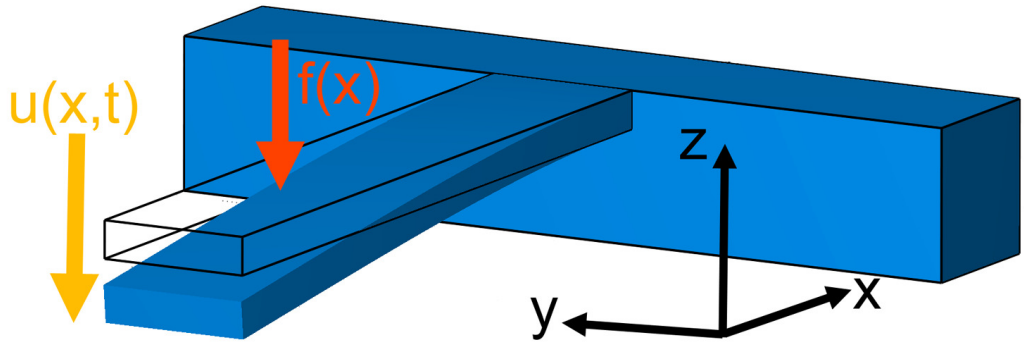

Figure 1.1: A schematic of cantilever beam with a single clamping point with a position-dependent displacement $u(x,t)$ due to a position-dependent, oscillating external force, $f(x)e^{-i\omega_c t}$.

encing a position-dependent force function $f(x)$ at the angular drive frequency ω_c. The complex displacement amplitude may be written

$$u(x,t) = \sum_{n=1}^{\infty} a_n u_n(x) e^{-i\omega_c t}, \tag{1.2}$$

where the summation is over the amplitude coefficients a_n and eigenfunctions $u_n(x)$ [32]. The $n = 1$ amplitude term is given by,

$$a_1 = \frac{1}{\rho A L} \frac{1}{\omega_1^2 - \omega_c^2 - i\omega_1^2/Q} \int_0^L u_1(x) f(x) dx, \tag{1.3}$$

where ω_1 represents the fundamental frequency close to ω_c and Q is the mechanical quality factor. If $f(x) = f_0$, in the case of a uniform force across the beam, the amplitude is is given by

$$a_1 = \frac{f_0}{M} \frac{\eta_1}{\omega_1^2 - \omega_c^2 - i\omega_1^2/Q}, \tag{1.4}$$

where $\eta_1 = 1/L^2 \int_0^L u_1(x) dx$ is the first moment of the eigenfunction $u_1(x)$ and $M = \rho A L$ is the mass. If $f(x)$ is proportional with $u_1(x)$ (ie. $\eta_1 = 1$), the

amplitude is then,

$$a_1 = \frac{f_0}{M} \frac{1}{\omega_1^2 - \omega_c^2 - i\omega_1^2/Q}. \tag{1.5}$$

1.3.2 Thermal Noise Processes and Dissipation

A figure-of-merit for a nanomechanical resonator is the quality factor Q, which is defined to be inversely proportional to the energy lost per cycle ΔE_{mech}

$$\frac{1}{Q} = \frac{1}{2\pi} \frac{\Delta E_{\text{mech}}}{E_{\text{mech}}}, \tag{1.6}$$

where E_{mech} is the total energy stored in the system. The quality factor is affected through various noise sources the resonator experiences, which are equivalently the various dissipation mechanisms through which the resonator exchanges energy with the environment. They can be extrinsic: fluid and atmospheric friction by cause of molecular collisions with the resonator, clamping losses because of acoustic wave reflections occurring at resonator supports and effects due to instrumental methods for transduction. The intrinsic dissipation mechanisms are not as well understood, but thermoelastic effects (where the vibrational motion causes temperature gradients in the system, allowing for heat exchange with the environment [33]) appear to play a large role, as do phononic and electronic interactions (especially as the devices are scaled down in dimension).

These dissipation mechanisms can be formally generalized under the fluctuation-dissipation theory [34, 35]. In the context of a mechanical resonator, the thermalization (fluctuation) of the motion leads to an energy dissipation, which contributes to amplitude and phase noise. The latter are fluctuations affecting the frequency stability of the device, usually described by the Allen deviation [36]. The thermal noise floor is one of the fundamental limits for the operation of nanomechanical systems, and in the absence of drive force, can be equated

to the energy stored in the resonator,

$$\frac{1}{2}k_BT = \frac{1}{2}k_{\text{eff}}\langle x^2\rangle, \tag{1.7}$$

where k_{eff} is the mechanical spring constant, x is the deflection amplitude, k_B is the Boltzmann constant, and T is the temperature of the source undergoing dissipation. The spectral density of the noise produces a mean deflection of the resonator at thermal equilibrium, but the forces experienced at different locations are uncorrelated. The spectral noise density $N_x(\omega)$ can be equated to the mean deflection with the relation

$$\langle x^2\rangle = \frac{1}{2\pi}\int_0^\infty N_x(\omega)d\omega \tag{1.8}$$

where $N_x(\omega)$ can be related to the white spectral density, $S_x(\omega)$ through a resonator response function $G(\omega)$ (in the form of Eq. 1.5) [37, 32],

$$N_x(\omega) = \left|G(\omega)^2\right| S_x(\omega). \tag{1.9}$$

Solving for the force density yields,

$$S_x(\omega) = \frac{2k_BT\omega_0^3}{\pi k_{\text{eff}}Q}\frac{1}{(\omega_0^2-\omega^2)^2 + (\omega_0\omega/Q)^2}. \tag{1.10}$$

For the thermomechanical calibration of torque magnetometers presented in Chapter 3, $S_x(\omega)$ is equated with a measured deflection of the noise to determine their thermal-noise-limited magnetic moment sensitivity.

1.4 Nanomechanical Torque Magnetometry

As mentioned previously, the early works involving the discovery of the Barnett and Einstein-de Haas effects were among the first to use the torque magnetometer design in fundamental scientific experiments. A few years later, K. Beck implemented one to measure the response of a sample which was placed

in various field directions and calculated an energy difference needed to magnetize it along different crystal orientations [38, 39]. This perhaps lead to one of the most popular applications of torque magnetometers, which is the determination of the magnetocrystalline anisotropy present in some magnetic samples. This is usually done by rotating the sample direction relative to the magnetic field and measuring the resulting torque curves, which can be fit to extract the anisotropy constants. The conventional torque magnetometer is rather too macroscopic for use in measurements of mesoscopic materials, and its use has been eclipsed by much more sensitive techniques using Hall Effect magnetometry, SQUIDs, and magnetoresistive sensors. But the advent of micromachining techniques that followed the invention of semiconductor integrated circuits in the 1950s would, in the following decades, give rise microelectromechanical systems. The earliest incarnations can be traced back to the availability of Si strain gauges [14], which were integrated into circuits as mechanical actuators or sensors.

Among the earliest micromechanical devices for magnetic field sensing are the cantilevers employed in magnetic force microscopy (MFM). Derived very quickly from atomic force microscopy (AFM, [40]) in 1987, the MFM operates on a similar principle [41, 42]. The cantilever's deflection characteristics under either static or resonant AC drives can be used to deduce the force between the cantilever's magnetic tip and the sample. In a few years the technique was extended to detect and image electron and nuclear magnetic resonance. Magnetic resonance force microscopy (MRFM) has lead to impressive breakthroughs such as the detection of a single electron spin [19] and the achievement of very high spatial resolution (10 nm) [43]. Another flavour of MRFM is ferromagnetic resonance force microscopy (FMRFM), where the deflection of the cantilever represents proportionally the amplitude of local spin wave modes [44]. FMRFM has successfully been used to image high order spin wave modes in disks [45] and measure dynamic responses in magnetic vortex cores [46, 47]. These techniques offer complementary dynamic information not yet fully accessible using nanomechanical torque magnetometry.

The first microscale torque magnetometers appeared in the early 1990s and through the decade were implemented for the detection of ferromagnetic resonance [48], characterization of magnetic thin films [49], and the micromechanical detection of the Einstein-de Haas Effect [50]. The principle mechanism behind torque magnetometry is expressed by $\boldsymbol{\tau} = \boldsymbol{M}V \times \mu_0 \boldsymbol{H}$, where a magnetostatic torque, $\boldsymbol{\tau}$, is exerted on the magnetic moments ($\boldsymbol{M}V$) by an external field ($\boldsymbol{H}$) where V is the magnetic volume, $\boldsymbol{M}$ is the magnetization and $\mu_0 = 4\pi \times 10^{-7}$ Hm^{-1} is the magnetic permeability of free space. This torque is transferred to the resonator, inducing a mechanical deflection that is proportional to the magnetization. The external field and magnetization orientations for cantilever and torsion paddle geometries are schematically shown in Fig. 1.2.

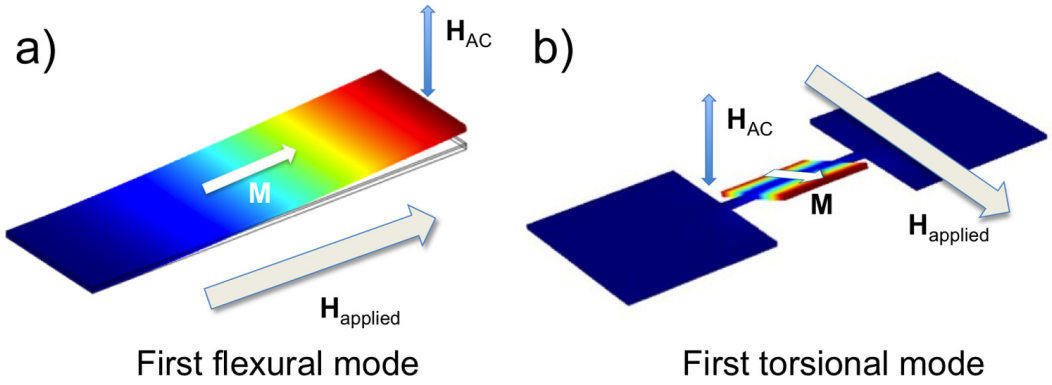

Figure 1.2: Magnetic torque actuation scheme for a) flexural cantilevers and b) torsional resonators. The directions of the magnetization $\boldsymbol{M}$ are shown respective to the applied and drive fields, $\boldsymbol{H}$ and $\boldsymbol{H_{AC}}$, respectively.

The benefits of scaling down the device is evident in the large number of applications available, analogous to macroscopic torque magnetometry measurements. Aside from the aforementioned benefits of decreasing the mechanical resonator's dimensions to detect small torques, the added experimental benefit of higher frequency (audio to radio) electronics further increases the measurement capability. AC lock-in detection can be matched to the driving field, at the natural resonance frequency of the resonator, maximizing sensitivity.

With advances in nanofabrication techniques, the microscale devices continued to further decrease in size, leading to the current era of nanomechanical torque magnetometers.

1.5 Micromagnetic Energies

This section outlines the basic energetic interactions involved in micromagnetic theory, which also give rise to the physically-relevant length scales that must be considered in micro- and nanomagnetic systems. Excellent references for a broader view of micromagnetism are given in [2, 51, 52, 53, 54].

The fundamental issue in the micromagnetics formalism is the development of a continuum description of the short-range atomic interactions (exchange, magnetocrystalline anisotropy) alongside those that occur over the overall magnetic volume, such as the demagnetization energy or the energy due to an external field. The theory, alongside numerical simulations, have become powerful tools for very accurately describing micromagnetic systems and have assisted in the rise of the information storage industry. The overall energy in micromagnetic systems can be given as a sum of the various energy interactions:

$$E_{\text{tot}} = E_{\text{exch}} + E_{\text{ani}} + E_{\text{demag}} + E_{\text{ext}}, \tag{1.11}$$

where is E_{exch} is the exchange energy, E_{ani} describes the magnetocrystalline anisotropy, E_{demag} the demagnetization and E_{ext} is the energy due to the external field. These energy terms will be discussed in the following subsections. Additional terms arising at surfaces, interfaces, and from interactions with electrical and spin currents, need not be considered in the context of this Thesis.

1.5.1 Exchange Energy

The fundamental interaction responsible for ferromagnetic ordering in materials is the exchange. Quantum mechanical in origin, the description entails a modification of the Coulombic interactions between neighbouring electron spins by virtue of the Pauli exclusion principle. In essence, a lowering of the electrostatic energy between two spin states occurs due to a spatial separation caused by the exclusion principle, which dictates that two identical electron states cannot occupy the same orbit. This quantum mechanical phenomenon became known as the "exchange" energy and can be described by the Heisenberg exchange Hamiltonian

$$\mathcal{H} = -2\sum_{i,j} J_{i,j}\boldsymbol{S}_i\boldsymbol{S}_j, \tag{1.12}$$

where the $\boldsymbol{S}_i$ and $\boldsymbol{S}_j$ denote the spin sites pairs the summations are taken over. J_{12} is the exchange constant governing the coupling between the pairs and is dependent on the atomic properties of specific systems. In ferromagnets, $J_{12} > 0$ and the neighbouring spins prefer a parallel alignment. If the angles between them are slightly offset there is an associated energy cost which, in the continuum limit of the crystal lattice can be described as

$$E_{\text{exch}} = A_{\text{exch}} \int_V [(\nabla m_x^2) + (\nabla m_y^2) + (\nabla m_z^2)] d^3r, \tag{1.13}$$

where $A_{\text{exch}} = 2JS^2z/a$ is known as the exchange stiffness constant (a material property), a is the nearest neighbour distance and z is dependent on the number of sites in the unit cell ($z = 1$ for simple cubic, $z = 2$ for body-centered cubic and $z = 5$ for face-centered cubic) [53, 51]. In the continuum approximation the magnetization $\boldsymbol{M}$ is treated as a continuous vector field, usually normalized by the magnitude of the saturation magnetization, that is $\boldsymbol{m} = \boldsymbol{M}/M_s$ where M_s is the saturation magnetization. The unit vector field $\boldsymbol{m}$ has the components m_x, m_y, and m_z (the direction cosines) defining the classical spin orientation as a function of position and is the fundamental en-

tity in the description. The length scale below which exchange is the dominant interaction is given by

$$L_{\text{ex}} = \sqrt{\frac{A}{\mu_0 M_S^2}}. \tag{1.14}$$

This is an important parameter when considering for the cell sizes in numerical simulations of micromagnetics, where sizes larger than the exchange length will provide spurious results [53]. For the magnetic materials studied in the following chapters, the exchange lengths are approximately 5 nm for permalloy and 9 nm for yttrium iron garnet (YIG).

1.5.2 External Field Energy

The energy (often called the Zeeman Energy in the non-continuum model) is associated with the interaction of the external magnetic field and magnetization has the expression

$$E_{\text{ext}} = -\int_V \mu_0 \boldsymbol{M} \cdot \boldsymbol{H} d^3 r \tag{1.15}$$

which shows a preference for the magnetization to align with the external field.

1.5.3 Magnetocrystalline Anisotropy

The preference of the magnetization to align along certain directions in a material (known as the easy axes) is a result of the magnetic anisotropy present in most ferromagnetic materials. In bulk ferromagnets, the anisotropy is responsible for the exhibited magnetic hysteresis and dictates domain wall widths (in competition with the exchange). The origin of the magnetocrystalline anisotropy is dominantly the effect of the spin-orbit coupling of the electronic wavefunction. Other contributions to the anisotropy, although relatively weak, are induced effects due to the creation of easy axes owing to lattice straining or the introduction of defects in magnetic systems [2]. The magnetocrys-

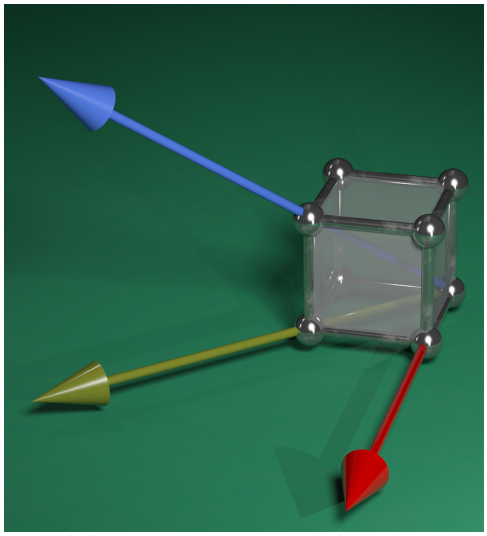

Figure 1.3: The possible magnetic easy directions in a cubic crystal, which are along the ⟨100⟩ (red), ⟨111⟩ (blue), and ⟨110⟩ (yellow) directions.

talline anisotropy is a quantum mechanical effect due to the symmetry breaking that occurs when the potential of the crystal lattice distorts the atomic orbitals. The spin-orbit interaction creates a stable configuration of the magnetic moment along a particular crystal axis direction. The expressions for the anisotropy energy are thus dependent on the properties of the lattice. For the case of uniaxial anisotropy, where a single axis defines the preferential magnetization directions ($\theta = 0$ or π), the energy has the form

$$E_{\text{ani}} = K_1 \sin^2\theta + K_2 \sin^4\theta \tag{1.16}$$

where K_1 and K_2 are known as the uniaxial anisotropy constants and θ is the angle between the magnetization and easy axis. For many monocrystalline materials the underlying lattice symmetry gives rise to a cubic anisotropy. In this case the anisotropy energy is at a minimum along three crystal directions representing the easy axes. The possible magnetic easy axes directions are

shown in Fig. 1.3. The energy is given as

$$E_{ani} = K_{C1}(m_x^2 m_y^2 + m_y^2 m_z^2 + m_x^2 m_z^2) + K_{C2}(m_x^2 m_y^2 m_z^2), \tag{1.17}$$

where K_{C1} and K_{C2} are the cubic anisotropy constants. For micromagnetic calculations in this work, magnetocrystalline anisotropy is neglected for polycrystalline permalloy thin films (where it is essentially 0). Cubic anisotropy must be considered for the YIG single crystal micromagnetic disk discussed in Chapters 5 and 6, where the easy axis is oriented along the $< 111 >$ directions.

1.5.4 Demagnetization Energy

The demagnetization energy (also known as the magnetostatic or dipolar energy) is a consequence of the shape of the magnetic material and describes the interaction of its magnetization with a self-generated field, known as the demagnetization field. The demagnetization energy is

$$E_{\text{demag}} = -\frac{\mu_0}{2}\int_V \boldsymbol{M} \cdot \boldsymbol{H}_D d^3 r \tag{1.18}$$

where $\boldsymbol{H}_D = N \cdot \boldsymbol{M}$ is the demagnetizing field and N is a tensor known as the demagnetizing factor. This long range interaction is responsible for domain formation, which is a consequence of a competition between the dipolar and domain wall energies. The dipolar field measured outside the sample is known as the stray field, which can be quite large in many single domain configurations. The stray field energy can be minimized, at the cost of introducing more domains. If the stray field is nearly completely eliminated, a flux-enclosed domain structure forms.

The determination of the demagnetization field is quite difficult, especially for more complicated geometries beyond simple shapes. This is due to $\boldsymbol{H_D}$ and $\boldsymbol{M}$ usually not being uniform within the material. The demagnetization calculation is normally performed numerically. It is also the most memory

and computation-intensive energy component in micromagnetic simulations, as interactions of each cell with every other across the sample geometry must be taken into account. This implies that n^2 energy terms are needed for the demagnetization calculation, thereby dictating the maximum grid size allowed in a simulation as the number needed for the exchange and anisotropy terms scales with n.

1.5.5 Landau-Lifshitz-Gilbert Equation

The fundamental dynamical system in magnetism is given by the Landau-Lifshitz-Gilbert (LLG) equation,

$$\frac{d\boldsymbol{M}}{dt} = -\gamma(\boldsymbol{M} \times \boldsymbol{H}_{\text{eff}}) + \frac{\alpha}{M_S}(\boldsymbol{M} \times \frac{d\boldsymbol{M}}{dt}) \tag{1.19}$$

where α is the phenomenological damping parameter and γ is the gyromagnetic ratio. The model describes the interaction of the magnetic moment with an effective external field $\boldsymbol{H}_{\text{eff}}$. The effective field can be calculated by taking the derivative of the above energy terms as a function of magnetization. In this system, after the moment aligns itself with the external field at some angle from its equilibrium position, it is allowed to precess. The damping assures that eventually the moment will come to rest.

Finite element (or difference) micromagnetic simulations are the most practical method for solving the LLG equation.

1.5.6 Micromagnetic Simulation

The unprecedented rise in computation power has benefitted greatly the speed and accuracy of numerical simulations. Their results have, in many cases, been found to be astonishingly matched to experimental results. For this reason, micromagnetic simulation is a powerful tool for device design, as various computation parameters can easily be adjusted. The extension to parallel graphics

processing unit architectures has allowed calculation results for large systems to be produced orders of magnitudes faster compared to only a few years ago [55]. The simulations done for the results presented in this Thesis are based on the calculation of the finite-difference time-domain formulation of the LLG equation. The simulation volume is divided into finite cells, each representing a single macro-spin where their magnetization directions are usually represented as direction cosines. During the time integration, the array of macro-spins is allowed to evolve under the various short and long-range energy interactions mentioned in the preceeding sections. A convergence criterion is checked at each time iteration step, and the simulation is stepped when the change in the angles of direction cosines falls below the set threshold.

1.6 Magnetic susceptibility and AC susceptometry

In cases of linear response of magnetization to applied magnetic field, a magnetic susceptibility χ is defined through

$$\boldsymbol{M} = \chi \boldsymbol{H}, \tag{1.20}$$

The susceptibility value can vary depending on material, and is not always scalar. For many materials χ is represented as a second-rank, symmetric tensor. Near the Curie temperature, T_C, demarcating the onset of ferromagnetism, the susceptibility diverges at the transition to spontaneous ordering.

In the present work we are interested in the susceptibilities which govern the evolution of volume-averaged magnetization (net magnetic moment) of mesoscopic structures versus applied field. In the magnetization evolution with external field, there are many regions which exhibit nonlinear transitions. In ferromagnetic materials these are often associated with irreversible events that occur through hysteresis (switching) but can also be a result of the effects of

magnetization depinning from defects, the Barkhausen effect, eddy-current dissipation or thermodynamic phase transitions. These nonlinear events are manifest as variations in differential susceptibility,

$$\chi_{ij} = \frac{\partial M_i}{\partial H_j}, \tag{1.21}$$

where M_i are the components of magnetization induced, H_j the applied field along a coordinate j, and χ_{ij} are the coefficients of the susceptibility tensor.

One can deduce the susceptibility from the numerical derivative of DC magnetization curves. By applying a small oscillating field on top of the DC field, the induced time-dependent magnetization response of the sample can also be measured. This technique is called AC (or dynamic) susceptibility. For a small AC field, $H_{AC}\cos(\omega t)$, the induced magnetization is

$$\boldsymbol{M_{AC}} = \chi_{AC}\boldsymbol{H_{AC}}\cos(\omega t). \tag{1.22}$$

The AC susceptibility measurement offers high sensitivity in regions where there are small changes in magnetization. A dynamical component can be captured through the differences in phase or temporal evolution between the drive field and magnetization response. Usually, this is done experimentally by lock-in detection of the real and imaginary parts of susceptibility, $\chi = \chi' + i\chi''$ corresponding to the in-phase and in quadrature signals with the driving field. AC detection inherently reports only reversible response. Dissipation appears in the out-of-phase, imaginary component detection channel. Slow dynamics can also be observed on very different time scales than the inverse drive frequency.

AC susceptometry applications are described in Chapter 5. There, an extension of AC susceptibility measurements to nanomechanical magnetometry is discussed, in an effort also leading towards exploration of the magnetization dynamics in single, mesoscopic elements. A new technique is introduced, which allows for the extraction of the AC susceptibility component while also recording the DC magnetization. The method can be extended to broadband

magnetization-response measurements.

Bibliography

[1] K. M. Petruso, *M Bulletin (Museum of Fine Arts, Boston)* **79**, 44 (1981).

[2] J. M. D. Coey, *Magnetism and Magnetic Materials* (Cambridge University Press, Cambridge, 2010).

[3] I. Charvátová, J. Klokočník, J. K. J. Kolmaš, *Stud. Geophys. Geod.* **55** (2011).

[4] C. A. Coulomb, *Histoire de l'Académie Royale des Sciences* p. 569 (1785).

[5] H. Cavendish, *Phil. Trans. Roy. Soc* **88**, 469 (1798).

[6] S. J. Barnett, *Physical Review* **6**, 239 (1915).

[7] A. Einstein, W. J. de Haas, *Koninklijke Akademie van Wetenschappen te Amsterdam, Proceedings* **18**, 696 (1915).

[8] H. G. Craighead, *Science* **290**, 1532 (2000).

[9] K. L. Ekinci, M. L. Roukes, *Rev. Sci. Inst.* **76**, 061101 (2005).

[10] X. M. H. Huang, C. A. Zorman, M. Mehregany, M. L. Roukes, *Nature* **421**, 496 (2003).

[11] P. S. Waggoner, H. G. Craighead, *Lab Chip* **7**, 1477 (2007).

[12] K. L. Ekinci, Y. T. Yang, M. L. Roukes, *J. Appl. Phys.* **95**, 2682 (2004).

[13] K. L. Ekinci, *Small* **1**, 786 (2005).

[14] C. Smith, *Phys. Rev.* **94**, 42 (1954).

[15] W. P. Mason, R. N. Thurston, *J. Acoust. Soc. Am.* **29**, 1096 (1957).

[16] K. Jensen, K. Kim, A. Zettl, *Nat. Nanotechnol.* **3**, 533 (2008).

[17] H. Y. Chiu, P. Hung, H. W. C. Postma, M. Bockrath, *Nano. Lett.* **8**, 4342 (2008).

[18] J. Chaste, A. Eichler, J. Moser, G. Ceballos, R. Rurali, A. Bachtold, *Nat. Nanotechnol.* **7**, 300 (2012).

[19] D. Rugar, R. Budaikan, H. J. Mamin, B. W. Chui, *Nature* **430**, 329 (2004).

[20] F. Jelezko, J. Wrachtrup, *Phys. Status Solidi* **203**, 3207 (2006).

[21] J. R. Maze, P. L. Stanwix, J. S. Hodges, S. Hong, J. M. Taylor, P. Cappellaro, L. Jiang, M. V. G. Dutt, E. Togan, A. S. Zibrov, A. Yacoby, R. L. Walsworth, M. D. Lukin, *Nature* **455**, 644 (2008).

[22] A. Naik, O. Buu, M. D. LaHaye, A. D. Armour, A. A. Clerk, M. P. Blencowe, K. C. Schwab, *Nature* **443**, 193 (2006).

[23] M. Poot, H. S. J. van der Zant, *Phys. Rep.* **511**, 273 (2012).

[24] J. D. Teufel, T. Donner, M. A. Castellanos-Beltran, J. W. Harlow, K. W. Lehnert, *Nat. Nanotechnol.* **4**, 820 (2009).

[25] A. N. Cleland, M. R. Geller, *Phys. Rev. Lett.* **93**, 070501 (2004).

[26] S. Etaki, M. Poot, I. Mahboob, *et al.*, *Nat. Phys.* **785**, 785 (2008).

[27] M. Eichenfield, R. Camacho, J. Chan, K. J. Vahala, O. Painter, *Nature* **459**, 550 (2009).

[28] D. V. Thourhout, J. Roels, *Nat. Photonics* **4**, 211 (2010).

[29] M. Li, W. H. P. Pernice, H. X. Tang, *Nat. Nanotechnol.* **4**, 377 (2009).

[30] S. P. Timoshenko, J. N. Goodier, *Theory of Elasticity* (McGraw-Hill, New York, 1970).

[31] L. D. Landau, E. M. Lifshits, *Theory of Elasticity* (Butterworth-Heinemann, St. Louis, 1986).

[32] A. N. Cleland, *Foundations of Nanomechanics - From Solid-State Theory to Device Applicatins* (Springer, Berlin, 2003).

[33] R. Lifshitz, M. Roukes, *Phys. Rev. B* **61**, 5600 (2000).

[34] H. B. Callen, T. A. Welton, *Phys. Rev.* **83**, 34 (1951).

[35] H. Nyquist, *Phys. Rev.* **32**, 110 (1928).

[36] D. Allen, *Proc. IEEE* **54**, 221 (1966).

[37] T. R. Albrecht, P. Grutter, D. Home, D. Rugar, *J. Appl. Phys* **69**, 660 (1991).

[38] K. Beck, *Vierteljahrschr* **63**, 116 (1918).

[39] H. J. Williams, *Rev. Sci. Instr.* **8**, 56 (1937).

[40] G. Binning, C. F. Quate, C. Gerber, *Phys. Rev. Lett.* **56**, 930 (1986).

[41] Y. Martin, H. K. Wickramasinghe, *Appl. Phys. Lett.* **50** (1987).

[42] J. J. Sáenz, N. García, P. Grütter, E. Meyer, H. Heinzelmann, R. Wiesendanger, L. Rosenthaler, H. R. Hidber, H. Güntherodt, *J. Appl. Phys.* **62**, 4293 (1987).

[43] C. L. Degen, M. Poggio, J. J. Mamin, C. T. Rettner, D. Rugar, *Proc. Nat. Acad. Sci.* **106**, 1313 (2008).

[44] I. Lee, Y. Obukhov, G. Xiang, A. Hauser, F. Yang, P. Banerjee, D. V. Pekekhov, P. C. Hammel, *Nature* **466**, 845 (2010).

[45] G. Guo, L. M. Belova, R. D. McMichael, *Phys. Rev. Lett.* **110**, 017601 (2013).

[46] B. Pigeau, G. de Loubens, O. Klein, A. Riegler, F. Lochner, G. Schmidt, L. W. Molenkamp, *Nat. Phys.* **7**, 26 (2011).

[47] G. de Loubens, A. Riegler, B. Pigeau, F. Lochner, F. Boust, K. Y. Guslienko, H. Hurdequint, L. W. Molenkamp, G. Schmidt, A. N. Slavin, V. S. Tiberkevich, N. Vukadinovic, O. Klein, *Phys. Rev. Lett.* **102**, 177602 (2009).

[48] M. Löhndorf, J. Moreland, P. Kabos, *Appl. Phys. Lett.* **76**, 3099 (2000).

[49] R. D. Biggar, J. M. Parpia, *Rev. Sci. Instr.* **69**, 3558 (1998).

[50] T. M. Wallis, J. Moreland, P. Kabos, *Appl. Phys. Lett.* **89**, 122502 (2006).

[51] S. Blundell, *Magnetism in Condensed Matter* (Oxford University Press, Oxford, 2003).

[52] S. Chikazumi, *Physics of Ferromagnetism, 2nd ed.* (Oxford University Press, Oxford, 2009).

[53] A. Aharoni, *Introduction to the Theory of Ferromagnetism* (Oxford University Press, Oxford, 2000).

[54] D. Jiles, *Introduction to Magnetism and Magnetic Materials* (Chapman and Hall/CRC Press, Boca Raton, 2000).

[55] L. Lopez-Diaz, D. Aurelio, L. Torres, E. Martinez, M. A. Hernandez-Lopez, J. Gomez, O. Alejos, M. Carpentieri, G. Finocchio, G. Consolo, *J. Phys. D.* **45**, 323001 (2012).

CHAPTER 2

Fabrication and Measurement Methods

2.1 Nano-fabrication of magnetometers for measurement of single, mesoscale elements.

The advances in nanomechanics and micromagnetism have developed alongside those in nano-fabrication, which over the recent years have allowed for the creation of structures with feature sizes in the tens of nanometers. These have come in the form of improving traditional methods and the invention of new techniques. Photolithography, a mainstay application in the 1960s integrated circuits industry [1], is still employed as resolutions are pushed to the nanometer regime with the use of optical wavelengths into the deep [2, 3] and extreme [4] ultraviolet. Electron beam lithography (EBL), initially performed using modified scanning electron microscopes, is now done using dedicated instruments with improved stability and pattern transfer from software design. Electron beam lithography resist chemistries have also improved to allow for sub-10 nm line-width exposures, limited by proximity and backscattering effects of the incident electrons [5]. Another technique involves the direct milling of materials using a focused beam (FIB) of ions (usually gallium, though the use of helium ions is gaining attention [6, 7]), which can also be used for the sputtering of materials locally to produce three dimensional struc-

tures [8, 9]. Soft lithography methods involve the imprinting of prefabricated molds (usually an elastic polymeric material like PDMS) to create patterns of structures with sizes from 30 nm to 100 µm [10]. Some 'bottom-up' methods involve self-assembly of materials using block copolymers [11, 12] or "dip-pen" nanolithography [13], in which molecules on an atomic force microscope cantilever tip transfer to a surface (forming monolayers) due to capillary forces in a liquid meniscus between the tip and surface. Perhaps the ultimate limit is the direct manipulation of atoms to create the smallest devices, of which hints have been observed through the use of scanning tunneling microscopes [14, 15]. Many of these techniques provide the means for fine-tuning device geometries to further increase sensitivity and transduction efficiency for micro- and nanomechanical resonators. In the following subsections two primary fabrication routes, through the use of electron beam lithography and focused ion beam milling, will be discussed. Both provide fast high-resolution pattern definition in their respective media, though are limited in terms of write areas because of increased exposure times. For areas below 2–300 μm^2, both are ideal for producing devices down to the nanometer scale relatively quickly.

Of particular interest for this thesis is the fabrication of high quality nanomechanical magnetometers for the capability of measuring only a single, micromagnetic element. The difficulties encountered in the placement of the magnetic material onto a mechanical resonator stems from several issues: 1. The incompatibility of the magnetic material with processing steps that involve strong acid-based etching to release the resonator 2. The effects of stiction (the collapse of the device onto the substrate layer) that often occurs when post-processing released devices. 3. Certain magnetic materials (such as epitaxial yttrium iron garnet) require template-assisted growth, which is a method that is difficult to localize to the surface of a resonator and to grow in arbitrary mesoscopic shapes. A number of different methods were devised within our research group to partially or completely bypass these limitations. For the fully (throughout the volume) magnetic permalloy cantilevers which were studied for the material presented in Chapter 3, a chemical modification of the acid solution was done to release the resonator by reducing its selectivity of

the magnet during etching. Magnetometer paddles have also been cut into silicon nitride membranes around pre-deposited magnetic disks using FIB milling [16]. For the device presented in Chapter 4, a commercial SiN membrane with a predefined array of equally spaced holes was used as a deposition shadow mask to apply thin-film magnetic disks onto resonators. A recently developed procedure for the lithographic definition of arbitrary magnetic shapes onto released devices is outlined in [17].

The material presented in Chapters 5 and 6 are results from the study of a single-crystal yttrium iron garnet disk, manually affixed onto a nanomechanical resonator. In order to obviate the difficulties mentioned above in creating mesoscopic single crystal magnets and placing them on nanomechanical resonators, a focused ion beam (FIB) instrument with the ability for nanomanipulation was employed. The disk was milled out of an epitaxial thick-film YIG using the FIB. The disk was then attached to a nanomanipulation arm and transferred to the resonator. In the following sections, the EBL and FIB methods for the fabrication of nanomechanical magnetometers are discussed.

2.2 Device Fabrication

EBL, through its ability to allow nanoscale pattern generation, is an essential fabrication tool. Although based on principles similar to photolithography, the shorter wavelengths of the electrons (typically 5–40 keV) allow for much finer write resolutions. The electrons interact within an electron-sensitive medium known as a resist, which consist of polymeric chains. The interacting electrons impart energy into the resist, enabling a cross-linking (or scission) of the polymeric chains and thus changing its solubility properties. Resists are available in two tones, positive and negative. In the former, the electron-exposed areas are removed when the resist is developed and remain in the latter type. Positive tone resists often used are PMMA (poly(methyl methacrylate)) and ZEP 520A. SU-8 and HSQ (hydrogen silsesquioxane) are popular negative resists. The operation of the EBL instrument is similar to that of a scanning electron

microscope (SEM), but with the added features of an electron beam-blanker, interferometrically aligned laser stage, and pattern-generation hardware. In most systems the beam is scanned based on the output of the pattern generator, which interprets the geometries defined in a user-created file (usually in GDSII format). For a standard operating procedure available at the University of Alberta Nanofab, please see [18]. For recent reviews discussing the operating principles and current status of EBL, see references [19, 20, 21].

Fabrication of the devices used herein began with the selection of silicon-on-insulator (SOI) substrates, which consist of silicon layers separated by an insulating oxide layer. The Si device (top) layer is usually thin (in our case 145 or 300 nm) and provides the material for the resonator. The buried oxide (SiO_2, 1 µm thick) forms a sacrificial layer. For our case, the specific thicknesses were selected in order to form an ideal interferometric cavity for the detection laser wavelength (more information is presented in Appendix D regarding the selection of the cavity depth). A 2% solution of HSQ, was spun onto 1 cm^2 SOI dies using a 100 rpm acceleration for 2 s and 4000 rpm spread for 30 s (Headway Resist Spinner). The dies were baked at 180° C for three minutes with the samples covered with a shield made from aluminum foil. It is crucial to transfer the dies to the EBL load-lock soon after the resist spinning step, as the HSQ's sensitivity changes over short time periods [22]. The electron beam lithographer used was a Raith 150-two system. Focusing, aperature alignment, and stigmation corrections can be accomplished by either using homogeneously sized gold nanoparticles (nominal diameters of 20 nm) dispersed in a solution and applied lightly to the corner of a die, or by a small scratch created by a diamond scribe. The use of a burn spot is not recommended in this case as the sensitivity of the resist does not allow for sufficient time for the focusing procedure. Post EBL exposure, the dies were developed in 25% tetramethylammonium hydroxide (TMAH) for 60 s. The exposed resist remained to act as a mask for the reactive ion etch (RIE) of the device layer, in which ions generated from a plasma in an RF field are accelerated towards the sample. The anisotropic etch of the silicon is caused by the physical bombardment of the ions, which alternate with a passivation process in order to

coat the trench sidewalls to avoid lateral etching (see [23] for a review of Si dry etching processes). The wet etching of the buried oxide layer was then done to release the device. This was accomplished using a buffered oxide etching (BOE) solution (10:1 volume ratio of 40% NH_4F in water to 49% HF in water), which has an etch rate of 55 nm/s. It is advisable to pattern 'freely floating' structures for verification (under an optical microscope) that the devices are released, as the non-clamped structures should be washed away during the etch. Such inspections should be carried out while the device substrate is in a liquid (such as distilled water or isopropyl alcohol (IPA)). The released devices were transported in IPA to a critical point dryer used to prevent stiction of the devices, accomplished by raising CO_2 gas to its sublimation point in order to remove the liquid/gas meniscus that causes an attractive force between the device and handle layers [24]. The released devices were removed from the critical point dryer and prepared for further lithography steps in order to apply magnetic material. Electron beam lithography recipes and detailed fabrication procedures are given in Appendix C.

2.2.1 Application of Thin-film Based Mesoscopic Magnets onto Devices

Permalloy (derived from 'permeability' and 'alloy') was used often because of its high magnetic permeability, relatively low coercivity, and a near-zero magnetostriction coefficient. These factors assist in the ability to induce changes in the material's magnetization using relatively low magnetic fields. The permalloy was applied onto the resonator using a collimated electron beam deposition system (UHV Evaporator EFM 3, Omicron Vakuumphysik GMBH, base pressure is 8×10^{-10} Torr). A high voltage is supplied to the evaporant source, which is in the form of a rod placed near a filament. A resulting electron bombardment causes a heating of the tip, resulting in evaporation of the source material. A collimation tube guides the evaporated material onto the resonators. The flux rate was monitored during deposition, and was typically

3.5 nm/min. The resulting smooth films have approximately a 0.3 nm root-mean-square roughness, with an overall thickness of 35–80 nm, calibrated by AFM.

Two methods were used to create deposition masks for the application of magnetic films onto the resonators. The first, for the devices presented in Chapter 4, a careful alignment of holes in a commercially available TEM silicon nitride window (DuraSiN, DTM-252321 1-2 µm dia. holes, 12 µm pitch, 100 nm thick) was done. The mask was placed over the devices using a vacuum tweezer (with a nozzle small enough to pick up the window by an edge) housed on a micromanipulator while observing under an optical microscope. Although the devices were of high quality, in the end only two (of the 15 total) resonators held a complete disk due to the difficulty of aligning such small features manually under an optical microscope. The second method involves a recently developed technique that allows for lithographic patterning of arbitrary shapes onto many mechanical resonators. The fabrication trick involved supporting the just-released devices in an electron-sensitive resist. The shapes were defined by electron beam lithography, and the developed resist provided the deposition mask. After permalloy was deposited onto the resonators, the resist was lifted off, leaving only the magnetic shape element. The fabrication method was successful largely by virtue of the ability to fabricate (with high yield) sensitive torque magnetometers, each housing a single mesoscale magnetic element [17]. No results from the latter devices are presented in this Thesis, but they are yielding very nice results in ongoing measurements.

2.2.2 Focused Ion Beam

The FIB was developed in the late 70s and early 80s and have found many applications in the semiconductor industry. These include the analysis of failure mechanisms in integrated circuits or the repair of photolithography masks, owing to its ability to locally mill or deposit material. FIB systems became commercially available in the early 90s, and have since been used for the fab-

rication of micro to nanoscale mechanical devices [8, 25]; from the milling of full devices to the fine tuning of their geometries. The FIB systems operate similarly to SEMs, but use a finely focused beam of gallium ions instead of electrons. At low currents, the ions can be used for imaging while milling and deposition are done with higher currents (typically in the tens to hundreds of picoamperes). The milling process involves the displacement of neutral or ionized atoms, along with secondary ions and electrons, in a material incident of the focused ion (or electron) beam. The ejected material can accumulate in the proximity of the milled area. The instrument's ability to deposit various materials is due to the ion beam induced chemical decomposition of a precurser material; which can be in solid, liquid, or gas form. The precurser is injected as a vapour or sputtered into the chamber, which is then adsorbed onto the surface of the substrate material. The energetic ions dissociate the molecular bonds, and the volatile products are released into the vacuum. The deposition of many materials, such as tungsten, platinum, gold or carbon are done through flowing organometallic gases into the instrument. In this fashion, two and three dimensional nanostructures can be created [26, 9]. Some systems implement a micromanipulation arm used for the transfer of materials.

The FIB is an indispensable tool for the fabrication of mechanical and magnetic structures. Devices have been made that involve the direct milling of magnetic material such as YIG or permalloy films on Si or SiN-membrane substrates. Many are shown and summarized in the Appendices. For the device that was used in studies presented in Chapters 5 and 6, the three-dimensional milling capabilities of the FIB is used to form a micromagnetic YIG disk from a bulk film. The micromanipulation arm was then used to transfer the disk onto a torsional resonator. This process is discussed in Chapter 5.

2.3 Measurement Apparatus

The measurement of the motion of nano and micro-mechanical devices consists of two components, the mechanism that causes the mechanical displace-

ment and the method to acquire the displacement change. The transduction process must overcome certain challenges, some of which are inherent to the system. The deflections, which can be on the order of picometers, are beyond the resolution of traditional diffraction-limited optical methods and electronic sensing. The scaling of the device resonance frequencies with size also necessitates electronic instruments be capable of high frequency (radio to microwave) operation. The measurement must also allow for data acquisition above the fundamental noise floors that the signals from these devices encroach. Optical interferometry (discussed in the next section), through its ability to resolve sub-nm motion [27], offers a means to tackle the hurdle of very small displacement sensing. The light is focused onto the edge of the resonator with the highest displacement amplitude allows for the light reflected from both the moving device and stationary substrate to interfere. With the tuning of the separation between the mechanical resonator and substrate (which form a Fabry-Perot cavity), constructive interference can be optimized. The modulated reflection is detected through the use of photodetectors and a high frequency lock-in amplifier.

In this setup, shown in Fig. 2.1 the laser (HeNe 632 nm, Melles Griot) is directed through a beam splitter, and then partly focused onto a device through an objective lens. The split beam can be used for the subtraction of common mode laser background. Rough alignment can be achieved through the observation of the reflected image through the objective. The photoreceiver (New Focus 1801) AC-coupled output is connected directly to a high frequency lock-in amplifier (Zurich Instruments HF2LI/UHFLI or Stanford Research Systems SRS844) and the DC signal is acquired through an auxiliary input. The lock-in output signal provides the reference (and drive) and is connected to a power amplifier (ENI 620L), which provides the current to the "dither" coils which provide in (and out) of plane driving fields. The coils are wound from insulated copper wire and, for the case of the in-plane coil, an aluminum frame in a Helmholtz coil geometry (Chapter 6) was used. The magnetization in the resonator is biased based on its distance from a strong permanent magnet housed on a motorized stepper rail. The stepper motor position is computer-controlled

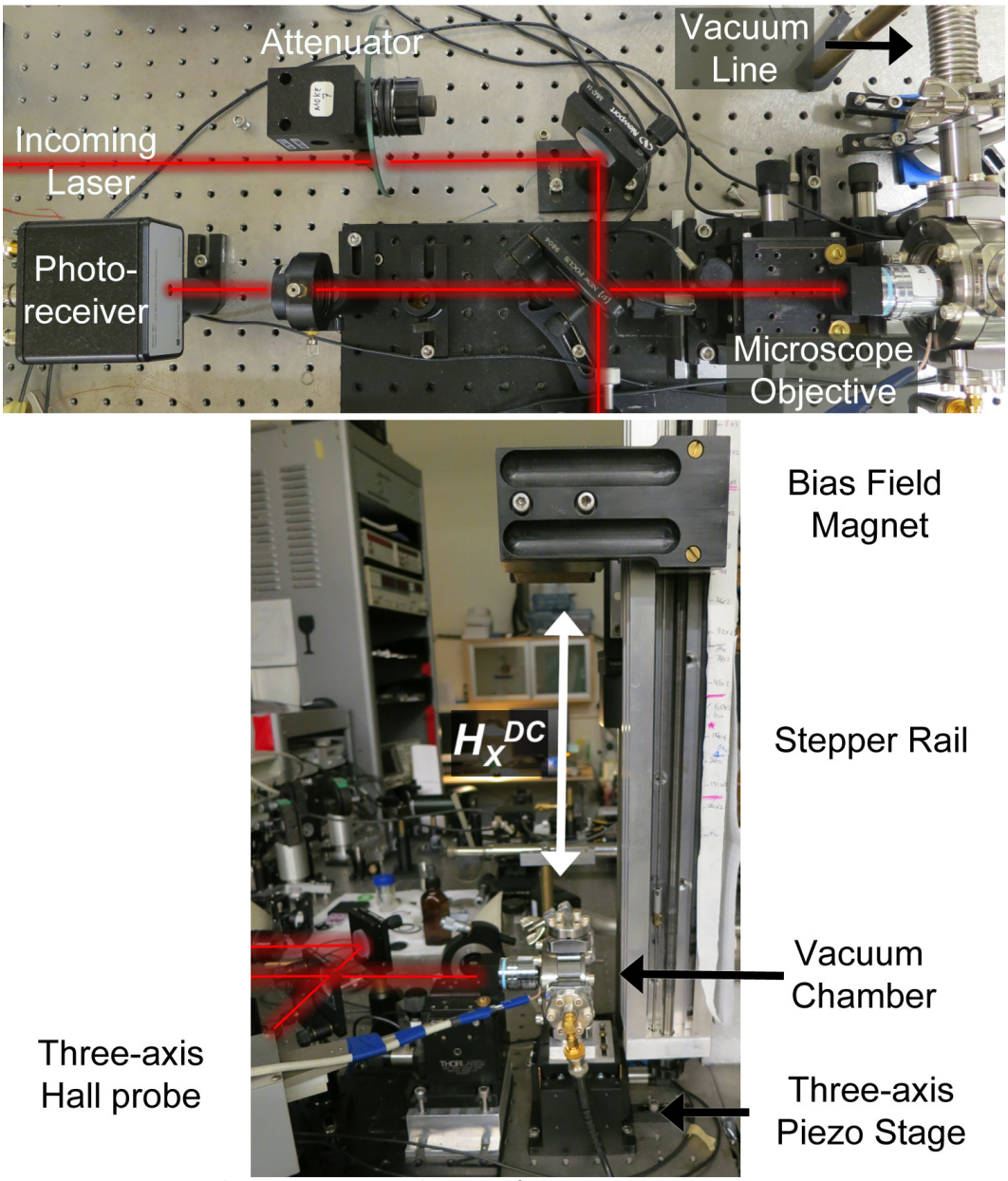

Figure 2.1: The experimental setup for torque magnetometry measurements (Top: top down view, Bottom: side view). The incoming laser (HeNe 632 nm) is directed through a microscope objective using a beam splitter and the signal is acquired at the photo-receiver. The AC coupled signal is connected directly to a lock-in amplifier input and the DC signal is used to acquire reflective intensity scans. A stepper rail is used to control the magnetic bias field at the device housed in a home-built vacuum chamber while the field magnitude is continuously read using a three-axis Hall probe.

based on a feedback routine using the readout from a three-axis Gauss meter sensor placed in the proximity of the resonator. Alternatively, the motor can run in continuous mode and the field magnitude can be calibrated later. The bias field range is from 0.1–40 kA/m. The drive signal is usually in sinusoidal form at the resonance frequency of the mechanical mode of interest, such that detection sensitivity is increased. For conducting magnetic hysteresis sweeps, the bias magnet is translated while the lock-in signal (magnitude, phase, x [in-phase] and y [quadrature]) is acquired at each field step.

The chip with the devices and 'dither' coils are housed on a small homemade chamber under approximately 10^{-6} Torr. The chamber is mounted on a piezo controlled three axis stage, which allows for the fine-tuning of the laser spot location and raster scanning for spatial signal mapping. Initial pumping of the chamber is done using a pumping station (with both roughing and turbo pump stages) until the pressure is adequate for an ion pump to safely function. The use of the ion pump minimizes external vibrations and can adequately keep the vacuum in the chamber under 10^{-6} Torr.

Bibliography

[1] J. R. Nall, J. W. Lathrop, *IEEE Transactions on Electron Devices* **5**, 117 (1958).

[2] B. J. Lin, *J. Vac. Sci. Technol.* **12**, 1317 (1975).

[3] P. Dumon, , W. Bogaerts, V. Wiaux, J. Wouters, S. Beckx, J. V. Campenhout, D. Taillaert, B. Luyssaert, P. Bienstman, D. V. Thourhout, R. Baets, *IEEE Photonics Technology Letters* **16**, 1328 (2004).

[4] C. W. Gwyn, R. Stulen, D. Sweeney, D. Attwood, *J. Vac. Sci. Technol. B* **16**, 3142 (1998).

[5] A. E. Grigorescu, *et al.*, *Microelectron. Eng.* **84**, 822 (2007).

[6] S. A. Boden, Z. Motadir, D. Bagnall, H. Mizuta, H. N. Rutt, *Microelectron. Eng.* **88**, 2452 (2011).

[7] J. J. Yang, D. C. Ferranti, L. A. Stern, C. A. Sanford, J. Huang, Z. Ren, L.-C. Qin, A. R. Hall, *Nanotechnology* **22**, 285310 (2011).

[8] S. Reyntjens, R. Puers, *J. Micromech. Microeng.* **11**, 287 (2001).

[9] S. Matsui, *J. Vac. Sci. Technol. B* **18**, 3181 (2000).

[10] Y. Xia, G. M. Whitesides, *Annu. Rev. Mater. Sci.* **28**, 153 (1998).

[11] M. Park, C. Harrison, P. M. Chaikin, R. A. Register, D. H. Adamson, *Science* **276**, 1401 (1997).

[12] S. O. Kim, H. H. Solak, M. P. Stoykovich, N. J. Ferrier, J. J. de Pablo, P. F. Nealey, *Nature* **424**, 411 (2003).

[13] R. D. Piner, J. Zhu, F. Xu, S. Hong, C. A. Mirkin, *Science* **283**, 661 (1999).

[14] J. A. Stroscio, D. M. Eigler, *Science* **254**, 1319 (1991).

[15] F. Chiaravalloti, L. Gross, H.-H. Reider, S. M. Stojkovic, A. Gourdon, C. Joachim, F. Moresco, *Nature Materials* **6**, 30 (2007).

[16] J. P. Davis, D. C. Fortin, J. A. J. Burgess, W. K. Hiebert, M. R. Freeman, *Appl. Phys. Lett.* **96**, 072513 (2010).

[17] Z. Diao, J. E. Losby, J. A. J. Burgess, V. T. K. Sauer, W. K. Hiebert, M. R. Freeman, *J. Vac. Sci. B* **31**, 051805 (2013).

[18] U. of Alberta Nanofab, *http://www.nanofab.ualberta.ca/site/wp-content/plugins/download-monitor/download.php?id=140* (2013).

[19] A. A. Tseng, K. Chen, C. D. Chen, K. J. Ma, *Electronics Packaging Manufacturing, IEEE Transactions on* **26**, 141 (2003).

[20] A. N. Broers, A. C. F. Hoole, J. M. Ryan, *Microelectron. Eng.* **32**, 131 (1996).

[21] M. Altissimo, *Biomicrofluidics* **4**, 1 (2010).

[22] F. C. M. J. M. van Delft, *Papers from the 46th International Conference on Electron, Ion, and Photon Beam Technology and Nanofabrication* **20**, 2932 (2002).

[23] B. Wu, A. Kumar, S. Pamarthy, *Journal of Applied Physics* **108**, 051101 (2010).

[24] I. H. Jafri, H. Busta, S. T. Walsh, *MEMS Reliability for Critical and Space Applications* **3880**, 51 (1999).

[25] A. A. Tseng, *Small* **1**, 924 (2005).

[26] G. Boero, I. Utke, T. Bret, N. Quack, M. Todorova, S. Mouaziz, P. Kejik, J. Brugger, R. S. Popovic, P. Hoffmann, *Applied Physics Letters* **86**, 042503 (2005).

[27] D. Vilkomerson, *Applied Physics Letters* **29**, 183 (1976).

CHAPTER 3

Nanomechanical torque magnetometry of permalloy cantilevers

This chapter was published in the Journal of Applied Physics ***108****, 123910 (2010) by J. E. Losby, J. A. J. Burgess, C. M. B. Holt, J. N. Westwood, D. Mitlin, W. K. Hiebert, and M. R. Freeman. The extension of the magnetically driven cantilever flexure model to multimodal analysis is presented in Appendix A.*

Abstract

There is mounting interest in bridging the fields of nanomechanics and nanomagnetism. Metallic nanocantilevers, which are magnetic throughout their volume, were fabricated using permalloy in order to detect domain switching along the cantilever length through mechanical deflection driven by magnetic torque. A finite element model describing the interaction of the magnetization of the cantilever with an external driving field is discussed and illustrated for the simple example of magnetization reversal via propagation of a straight domain wall. The interferometrically obtained cantilever deflection through the magnetic actuation of the fundamental mode exhibits magnetic hysteresis. The experimental results are also compared to the finite element mechanical transformation of the output from a Landau-Lifshitz-Gilbert based micromagnetic simulation of the hysteresis.

3.1 Introduction

Micro- and nanomechanical systems have proven successful in providing a means to probe ultrasensitive phenomena such as quantum-limited displacement [1, 2], photonic interactions with resonators [3, 4] and minute frequency shifts due to atomic mass loading [5, 6]. These devices usually operate in their mechanical resonance modes and have been implemented as micro-scale torque magnetometers [7, 8, 9, 10] and as probes in MRFM [11, 12, 13]. The mass loading and deflection characteristics of cantilevers and doubly-clamped beams have been well-studied since the mid-18th century (Euler-Bernoulli theory) and their extension to nanoscale dimensions has been very successful [14]. Due to high sensitivity and a simple geometry, a magnetic nanocantilever could provide an advantageous means to mechanically observe dynamics, through phenomena such as magnetization switching and ferromagnetic resonance, of the magnetic microstructure [15].

Here, the magnetic cantilever experiences a deflection through a mechanical load caused by a torque due to an external field acting on its magnetization, $\boldsymbol{M}$, described by $\boldsymbol{\tau} = \boldsymbol{M}V \times \mu_0 \boldsymbol{H}$, where V is the volume of the magnetic material. In this study, a model is developed to describe the deflection of a magnetic cantilever due to a distributed load arising from the interaction of a non-uniform magnetization with an external field. Afterwards, the fabrication and mechanical resonance measurements of metallic cantilevers composed entirely of permalloy ($Ni_{80}Fe_{20}$), is presented. Finally, magnetization measurements of a nanocantilever, magnetically actuated at the fundamental resonance mode, are described and compared to results from micromagnetic simulations which have been transformed by the mechanical deflection model.

3.2 Model of magnetically-driven cantilever flexing

In this study, mechanical motion of the magnetic cantilevers are actuated by torque from a time-varying external magnetic field perpendicular to the plane of the film from which the beam is fabricated. Interacting with the magnetization along the length of the cantilever, this field generates a torque causing flexure out of the plane. The magnetization, applied field and mechanical torque directions are shown in Fig. 3.1a. In-plane magnetization across the width of the cantilever leads to torsion of the beam. Specifically here we are interested in sinusoidal driving of the fundamental nanomechanical flexural resonances, and assume that the AC magnetic field is weak enough to not disturb the orientation of the magnetization (which is dictated by the shape anisotropy of the beam). The continuum bending theory of cantilevers involves modelling the load as a point or a distributed force. When the cantilever is uniformly magnetized along its length, the net magnetic dipole can be represented by equal and opposite magnetic charges at the fixed and free ends. In this case the actuation is effectively a point force at the free end, $\boldsymbol{F}(L,t)$. For the general case of a non-uniformly magnetized cantilever, discretizing the volume into finite element cells allows the torque interaction to be cast as two distributed forces per unit length, $p^+(x,t)$ and $p^-(x,t)$, where the moment of each cell is modelled by appropriate magnetic charges, $+m$ and $-m$, lining each cell boundary and the force per unit length on each calculated as $\boldsymbol{F} = m\boldsymbol{H}/\Delta x$, were $\boldsymbol{H}$ is the AC field amplitude and Δx is the width of the cell [16]. The amplitude of displacement as a function of angular frequency ω and position x for the cantilever of length L driven by such a distributed force is given by

$$z(x,\omega) = \sum_{n=1}^{\infty} \frac{p_n(\omega)}{-m_n\omega^2 + ic_n\omega + k_n}\phi_n(x), \tag{3.1}$$

where the sum is made over all of the eigenmodes of free flexural vibration of the cantilever, x is the position measured from the clamped end, m_n, c_n, and k_n are the coefficients for the modal mass, damping, and spring constant, and $p_n(\omega)$ is the Fourier transform of

$$p_n(t) = \int_0^L p(x,t)\phi_n(x)\,dx. \tag{3.2}$$

Here, $\phi_n(x)$ is the shape function of the nth eigenmode [17]. These functions have the form $\phi_1(n) = a_n(\cos\kappa_n x - \cosh\kappa_n x) + b_n(\sin\kappa_n x - \sinh\kappa_n x)$, where in particular $\kappa_1 L = 1.875$ is the modal wavenumber of the first mode and the relative amplitudes a_1/b_1 = -1.3622 [18]. Restricting consideration to the fundamental mode driven on resonance, the amplitude of response at the free end is

$$z(L) = \frac{p_1^+(\omega_1) - p_1^-(\omega_1)}{ic_1\omega_1}\phi_1(L). \tag{3.3}$$

The calculated first mode curvature for a cantilever fully magnetized in the $-x$ direction is plotted in Fig. 3.1b. A simulation of the simplest case of magnetization reversal, a straight domain wall traversing the cantilever, is easily performed. The cantilever is initially set to be fully magnetized in the $+x$ direction, and a reversed domain grows as the domain wall sweeps along the length. The resulting cantilever deflection amplitude for the first vibrational mode calculated versus domain wall position is plotted in Fig. 3.1c. It is essential to note here that the deflection is not simply proportional to the net magnetization in the x direction as the moments near the fixed end of the cantilever contribute less to the drive than the moments closer to the free end. A further transformation of the measured deflection versus applied field is required in order to render the data as net magnetization versus field.

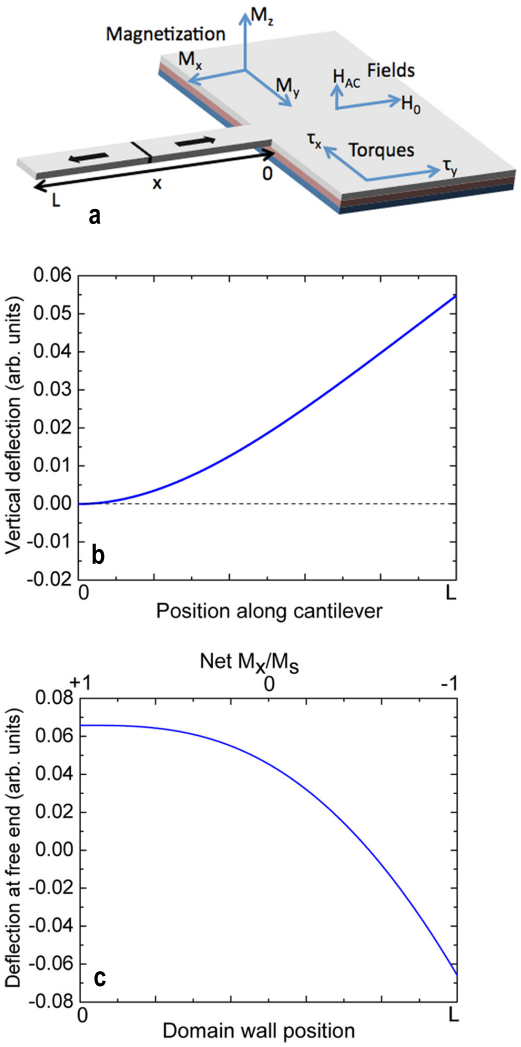

Figure 3.1: (a) Magnetic actuation schematic of a magnetic nanocantilever. The magnetization along the cantilever, M_x, is mediated by the external field $\boldsymbol{H_0}$ while the sinusoidal torquing field, $\boldsymbol{H}_{AC}$, drives the flexural torque. For the simple case of magnetization reversal, a straight domain wall propagates across the cantilever, represented by the black line perpendicular to the length. A twisting torque, τ_y, is induced if a component of magnetization is oriented perpendicular to the cantilever length. (b) First vibrational mode shape calculated using the magnetic actuation model. The dotted line represents the equilibrium position. (c) Calculated deflection profile for the first vibrational mode at the free end of the cantilever as the straight domain wall was swept across the cantilever to switch the magnetization from $+M_x$ to $-M_x$.

3.3 Device Fabrication and Mechanical Properties

The device geometry of an array of permalloy cantilevers with varying lengths (lengths=5 to 2 µm, widths=300,500 nm) were defined using electron beam lithography (EBL) with a bilayer positive resist (PMMA 950/495, total thickness 360 nm) spun on 400 nm thick SiO_2, which was thermally grown on a Si wafer. Permalloy, chosen for its extensive investigation in the field of micromagnetics, was deposited onto the developed substrate using a DC magnetron co-sputtering system as the sample stage continuously rotated. The film compositions were later confirmed using electron dispersive x-ray analysis (EDAX) mounted on a Hitachi S3000N scanning electron microscope (SEM). Afterwards, a lift-off procedure was performed to remove the previously unexposed resist, leaving the magnetic film in the EBL-defined areas. The oxide layer was then etched in a $FeCl_2$-saturated buffered oxide etch solution to release the cantilevers while minimizing the etching of the metal. A SEM micrograph of a completed device is shown in the inset of Fig. 3.2. Since the sputtered deposition is not collimated, shadowing by the resist edge is very significant and determines the final cross-sectional profile of the patterned film. In particular, rather than having a rectangular cross section, the cantilevers are thinner at the edges than they are in the middle as can be seen in the SEM micrograph in Fig. 3.2. In addition, the permalloy film thickness in the pedestal (clamping) area will be greater than the maximum thickness of the cantilever as-deposited, with a tapering down of the thickness near the base of the cantilever over a length comparable to the cantilever width. This thickness variation is accentuated by the oxide etch; as even with the $FeCl_2$-saturated solution, the etch of the metal is not eliminated. The ragged edge along the sides of the cantilever and support structure is from a very thin coverage of sputtered metal on the resist sidewalls prior to lift-off.

The initial search for the fundamental resonance frequencies of the permalloy cantilevers were done using a piezo element, driven through the RF output

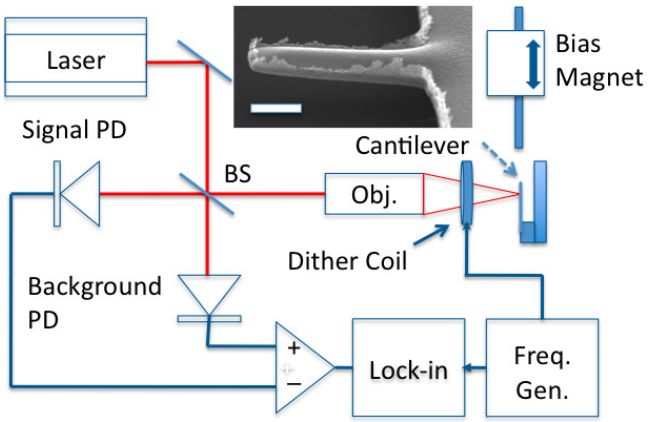

Figure 3.2: Instrumentation for optical interferometric detection and magnetic actuation scheme (PD=photodiode, BS=beam splitter, Obj.=objective lens). The bias magnet is rotatable and situated on an automated translation rail. A 'dither' coil provides the AC magnetic field transverse to the direction of magnetization and the resulting mechanical torque is detected interferometrically. The devices are driven at the cantilever flexural resonance frequency, referenced to a lock-in amplifier. A scanning electron microscope image of a 2 um long, 300 nm wide cantilever is shown in the inset. The scale bar represents 500 nm.

of a network analyzer (HP8752C), mounted underneath the sample chip. All experiments were conducted with the chip placed in a custom built vacuum chamber that maintained a vacuum of $\sim 10^{-5}$ Torr pressure at room temperature. A helium neon laser ($\lambda = 632.8$ nm) was used to interferometrically detect the cantilever motion through small perturbations in the reflected optical power, where the contrast was provided by the top surface of the cantilever and the Si substrate. The set of cantilevers displays resonant frequencies varying approximately with their inverse length squared. The detected resonance frequencies are plotted in Fig. 3.3, in accordance to the continuum mechanics expectation for the fundamental out-of-plane flexural modes,

$$f_{res}^{-1/2} = \sqrt{\frac{2\pi}{3.516}} \left(\frac{\rho A}{EI}\right)^{1/4} L, \tag{3.4}$$

where L is the beam length, E is the effective Young's Modulus, I is the moment of inertia, ρ is the density, and A is the cross sectional area of the cantilever [18]. The solid line is a linear least-squares fit to the measured data (circles), and yields a slope of 0.17 ± 0.01 MHz$^{-1/2}/\mu$m. This indicates that the ratio $\rho A/EI$ for the as-fabricated cantilevers is 1.49 times larger than the ratio calculated using the properties of bulk Ni ($E = 219$ GPa, $\rho = 8900$ kg/m^3) and assuming the cantilever cross-section to be rectangular, 100 nm thick by 300 nm wide, and uniform along the length. The latter ratio was confirmed by finite element modelling (Comsol) with results summarized by the dashed line in Fig. 3.3. The difference might be due in part to the Young's modulus of the sputtered permalloy being lower than that of bulk Ni. The x-axis intercept of the fit line to the measured frequencies reveals a subtle variation over what is ordinarily found. Although we know there is an undercut of the film along the pedestal edges, the film here is sufficiently thicker that this undercut does not make the cantilevers behave mechanically as if they have an effective length greater than the design length. Rather, the linear fit to data points in Fig. 3.3 shows a positive x-intercept, as if the devices have a "negative" undercut. Qualitatively, this is consistent with the tapering of thickness at the cantilever bases due to shadowing. Although for the modelling this thickness variation should be taken into account, we do not consider it further here. It would be a sufficient correction for this purpose to treat the cantilever as having an effectively shorter length. The inset of Fig. 3.3 is the frequency spectrum response, acquired using the network analyzer, of a 5 µm long cantilever and is fitted to a Lorentzian lineshape (red line). The extracted quality factor is 880. The measured quality factors of our devices ranged from 300 to 1000, close to those values acquired in recent studies of metallic nanocantilevers conducted under similar experimental environments (temperature and pressure) [19, 20].

To drive the magnetic cantilever a torque was exerted on its magnetization through a small time varying 'dither' field, $\boldsymbol{H}_{AC}$ of approximately 10 A/m, directed orthogonal to the direction of magnetization. The magnetization was oriented along the length of the cantilever through an external DC field, $\boldsymbol{H}_0$, provided by a permanent magnet. The oscillatory torque τ_x was driven at the

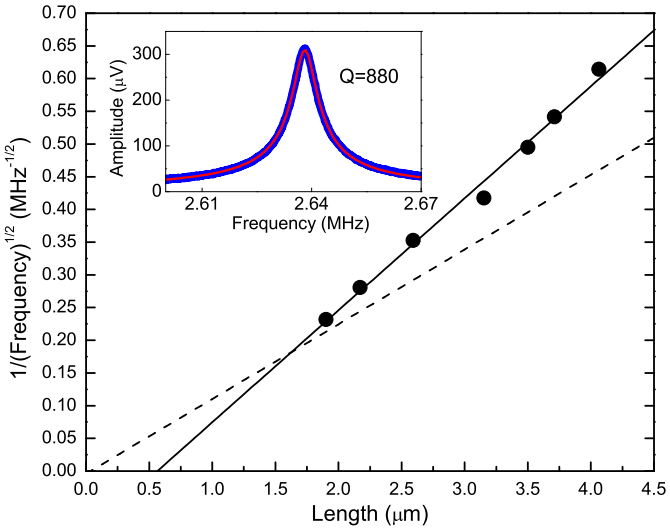

Figure 3.3: Fundamental resonance frequencies of the set of permalloy cantilevers. The solid line is a linear least squares fit to the data (solid circles) and the dashed line is the expectation based on the ideal design geometry and using the mechanical parameters (Young's modulus, density) of bulk nickel. A frequency spectrum for a 4 μm long cantilever is shown in the inset, fitted to a Lorentzian lineshape. The quality factor of 880 was extracted from the fit.

first flexural mode of the cantilever and detected using optical interferometry, as discussed in the previous section. The instrumentation schematic is shown in Fig. 3.2. A frequency generator provided the sinusoidal signal to the AC dither coil (a loop of insulated copper wire with a diameter large enough to allow the passage of a laser) at the resonance frequency of the cantilever and referenced at the lock-in amplifier. A single axis Hall probe was placed near the devices to detect the field from the bias magnet, placed on a translation rail to allow for field sweeping. The instrumentation allows for spatial imaging capabilities through rastering a piezo-controlled, three-axis scanning stage during data acquisition; with a maximum pixel resolution of 256 × 256 and an optical resolution that is limited by the diffraction limit of the microscope

objective. The images in Fig. 3.4 are acquired at the resonance frequency (2.72 MHz) of a 4 µm long cantilever. The reflected intensity is shown in Fig. 3.4a., where the free end of the cantilever is situated near the middle of the panel. The in-phase lock-in signals are shown in Figs. 3.4b. and 3.4c, taken at -12 kA/m and +12 kA/m bias fields, respectively, and show the signal localized to the free end of the cantilever. The bias fields are above the saturation magnetization of the cantilever in both directions, and their signals (as indicated by the colour map, in arb. units) are out of phase; implying that the mechanical torque direction has switched with respect to the drive signal.

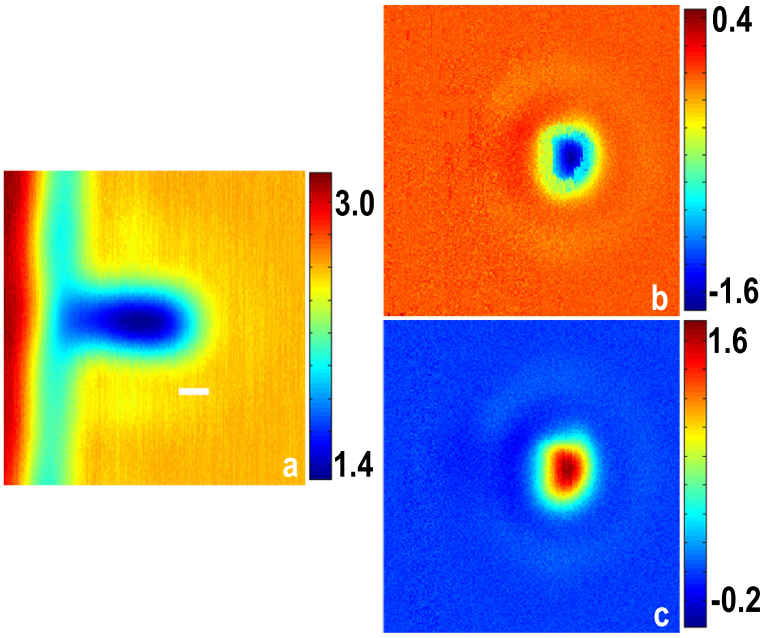

Figure 3.4: Spatial imaging on the resonance frequency of a 4 µm cantilever (a) Raster scanned image of the reflected optical intensity (scale bar = 1 µm). (b),(c) In-phase lock-in signals acquired at -12 kA/m and $+12$ kA/m, respectively. The colour bar scale is in arbitrary units.

3.4 Magnetic actuation and hysteresis measurements

The magnetization reversal process in the cantilever was examined through the phase and magnitude lock-in signals while the cantilever was driven at its resonance frequency, Figs. 3.5a and 3.5b. The signals were acquired from the spatial scans in order to compensate for the effect of the strong bias magnet causing a small systematic drift as it pulled on magnetic components in the vacuum chamber and scanning stage during the field sweep. The bias field was initialized at -9.2 kA/m, ramped to 11 kA/m, and then reversed. The data points for each quarter of the hysteresis loop is represented in order as squares, stars, triangles, and solid circles. When the direction of magnetization along the cantilever is reversed, the torque relative to $\boldsymbol{H}_{AC}$ will be in the opposite direction, resulting in a 180° phase difference with the driving signal; as seen in Fig. 3.5b. The switching fields for this cantilever were approximately 9.3 and -7.0 kA/m. The magnitude indicates that the switching process is not so abrupt and instead goes through slower switching regions as the signal decreases, followed by a sudden jump. The symmetric nature of these regions can be attributed to domain pinning effects, as the domain nucleation is likely to occur in the much larger pedestal for both field directions. The phase and magnitude signals were combined to illustrate a magnetic hysteresis loop that is related to the x-component of magnetization, where the amplitude polarity represents the direction of magnetization, Fig. 3.5c. The amplitude is related to the cantilever deflection due to a propagation of a domain wall across the cantilever, and will be discussed in the next section in comparison to micromagnetic simulations.

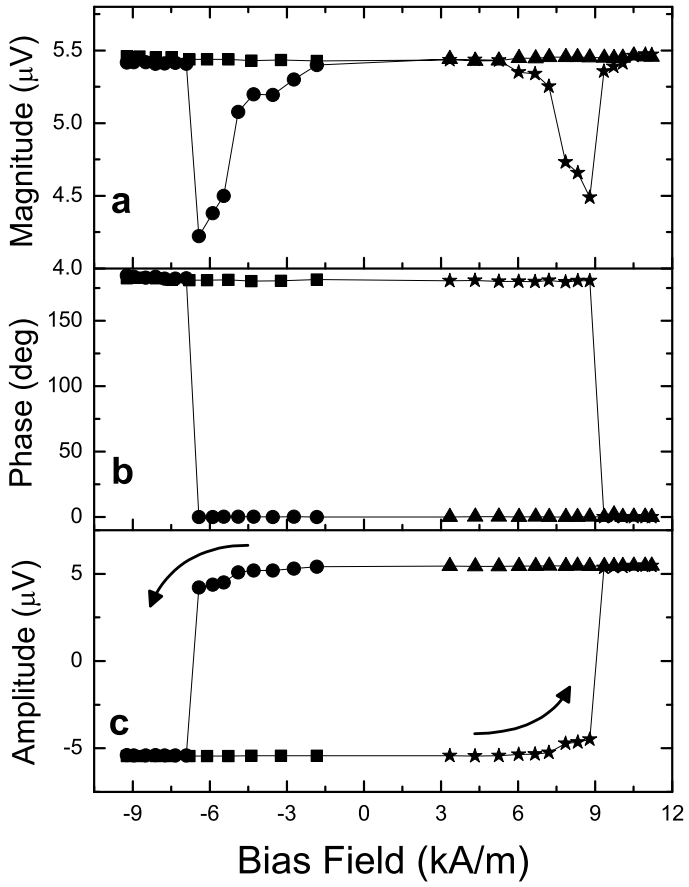

Figure 3.5: Lock-in (a) phase and (b) magnitude signals acquired during the magnetization sweep of a 4 µm long cantilever while driven at its resonance frequency. The symbols represent each quarter of the hysteresis loop (in order: square, star, triangle, and circle). (c) Amplitude through the combination of the phase and magnitude signals

3.5 Micromagnetic simulations

In order to further elucidate the switching process, Landau-Lifshitz-Gilbert (LLG) based micromagnetic simulations were performed on an approximation of the cantilever using LLG Micromagnetics software (v2.0). A rectangular geometry 5 µm long, 500 nm wide and 100 nm thick was used with free boundary conditions on five of the faces and an artificially pinned boundary condition (in the $+x$ direction) on the remaining face to simulate the permalloy pedestal at the base of the device. A grid with spacings of 5 nm in plane was used in order to realistically capture the behavior of vortices and domain walls moving within the cantilever. The cells were 50 nm in length out of plane in order to reduce the computational load to a manageable level. Realistic parameters were used including a saturation magnetization of 800 kA/m, a gyromagnetic ratio of 0.21 MHz/(A/m), a damping parameter of 0.02 and a temperature of 300 K. The switching behaviour of the cantilever was examined by relaxing the magnetic configuration of the cantilever at high positive field, and subsequently sweeping down to negative field. At -400 A/m, the boundary condition representing the pedestal magnetization was reversed while the field sweep was continued in steps of -400 A/m. In addition to the relatively small field steps, particular care was taken to allow long integration times at each field step to allow equilibration of the magnetization distribution in light of the realistic damping parameter. At the reversal a domain was nucleated at the base of the cantilever and was subsequently pushed up the cantilever as the bias field increased, representing the last quarter of a hysteresis loop. Selected simulation steps of the M_x components of the field sweep are shown in the inset of Fig. 3.6. The simulation results were then converted into the mechanical deflection profiles using the methodology presented in Section I and are shown in Fig. 3.6. The experimental amplitude decrease, in the last quarter (circles) of the hysteresis loop in Fig. 3.5c, can be qualitatively understood through the lowering of the calculated deflection, due to the ordering of M_x changing through the switching field. A nearly complete reversal process occurs at approximately -7 kA/m, similar to the measured result.

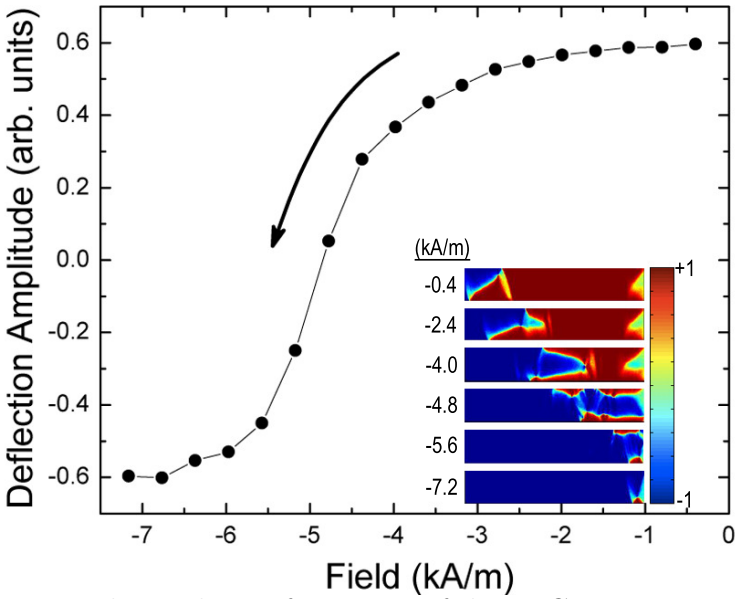

Figure 3.6: Mechanical transformation of the LLG micromagnetics simulation representing the final quarter of a cantilever hysteresis loop. The magnetization was equilibrated at a high positive field with free boundary conditions on five of the cantilever faces and an artificially pinned boundary in the $+x$ direction on the face at the base of the cantilever (x=0). The field was then swept down to negative field. At -400 A/m, the magnetization at the base of the cantilever was reversed while the sweep continued in steps of -400 A/m. The deflection profile was calculated using Eq. 1. In the inset are selected spatial distributions of the x-components of magnetization during the loop. The color bar represents the normalized M_x.

3.6 Conclusion

In summary, we have outlined a magnetic cantilever deflection model as its magnetization interacts with an external field and offered the simple case of a straight domain wall switching the magnetization along the cantilever length. We have also fabricated nanoscale permalloy cantilevers using a process compatible with current Si-based nanofabrication methods and the devices exhibit flexural resonance frequencies that agree with the continuum mechanics prediction. Magnetic domain switching was detected through the mechanical oscillations of the cantilevers, while they were driven at their fundamental resonance frequencies, and their flexural behavior was described through micromagnetic simulations. The simple geometry of a cantilever system and the extensive micromagnetics research background of permalloy may offer an advantage in understanding the interactions of the magnetization with the mechanical properties of the resonator, leading to sensing applications and the investigation of interesting fundamental physical phenomena; such as nanomechanical magnetization reversal [21, 22] . It has been recently shown through a series of theoretical outlines that degenerate mechanical and magnetic modes could occur, and efficiently couple, in the microwave regime. The transduction of cantilevers into the GHz range has been shown to be achievable [23], offering the possibility of implementing magnetic nanoresonator devices similar to those studied herein to study such interactions.

Bibliography

[1] A. D. O'Connell, M. Hofheinz, M. Ansmann, R. C. Bialczak, M. Lenander, E. Lucero, M. Neeley, D. Sank, H. Wang, M. Weides, J. Wenner, J. M. Martinis, A. N. Cleland, *Nature* **464**, 697 (2010).

[2] T. Roscheleau, T. Ndukum, C. Macklin, J. B. Hertzberg, A. A. Clerk, K. C. Schwab, *Nature* **463**, 72 (2010).

[3] M. Eichenfield, R. Camacho, J. Chan, K. J. Vahala, O. Painter, *Nature* **459**, 550 (2009).

[4] M. Li, W. H. P. Pernice, H. X. Tang, *Nat. Nanotechnol.* **4**, 377 (2009).

[5] H. Y. Chiu, P. Hung, H. W. C. Postma, M. Bockrath, *Nano. Lett.* **8**, 4342 (2008).

[6] K. Jensen, K. Kim, A. Zettl, *Nat. Nanotechnol.* **3**, 533 (2008).

[7] J. P. Davis, D. C. Fortin, J. A. J. Burgess, W. K. Hiebert, M. R. Freeman, *Appl. Phys. Lett.* **96**, 072513 (2010).

[8] M. D. Chabot, J. Moreland, *J. Appl. Phys* **93**, 7897 (2003).

[9] D. H. Min, A. McCallum, S. E. Russek, J. Moreland, *J. Magn. Magn. Mater.* **286**, 329 (2005).

[10] Z.-H. Wei, Y.-P. Hsieh, Y.-R. Lee, C.-D. Lin, C.-P. Lee, C.-N. Liao, Y.-J. Chen, C.-J. Hsu, *Jpn. J. Appl. Phys* **48** (2009).

[11] J. A. Sidles, J. L. Garbini, K. J. Bruland, D. Rugar, O. Züger, S. Hoen, C. S. Yannoni, *Rev. Mod. Phys.* **67**, 249 (1995).

[12] D. Rugar, R. Budaikan, H. J. Mamin, B. W. Chui, *Nature* **430**, 329 (2004).

[13] I. Lee, Y. Obukhov, G. Xiang, A. Hauser, F. Yang, P. Banerjee, D. V. Pekekhov, P. C. Hammel, *Nature* **466**, 845 (2010).

[14] A. N. Cleland, M. L. Roukes, *Appl. Phys. Lett.* **69**, 2653 (1996).

[15] A. A. Kovalev, G. E. W. Bauer, A. Brataas, *Jpn. J. Appl. Phys* **45**, 3878 (2006).

[16] S. Chikazumi, *Physics of Ferromagnetism, 2nd ed.* (Oxford University Press, Oxford, 2009).

[17] M. V. Salapaka, H. S. Berth, J. Lai, A. Majumdar, E. McFarland, *J. Appl. Phys.* **81**, 2480 (1997).

[18] A. N. Cleland, *Foundations of Nanomechanics - From Solid-State Theory to Device Applicatins* (Springer, Berlin, 2003).

[19] N. Nelson-Fitzpatrick, C. Ophus, E. Luber, L. Gervais, Z. Lee, V. Radmilovic, D. Mitlin, S. Evoy, *Nanotechnology* **18**, 355303 (2007).

[20] J. Verd, A. Uranga, G. Abadal, J. Teva, F. Torres, F. Pérez-Murano, J. Fraxedas, J. Esteve, N. Barniol, *Appl. Phys. Lett.* **91**, 013501 (2007).

[21] A. A. Kovalev, G. E. W. Bauer, A. Brataas, *Appl. Phys. Lett.* **83**, 1584 (2003).

[22] A. A. Kovalev, G. E. W. Bauer, A. Brataas, *Phys. Rev. Lett.* **94**, 167201 (2005).

[23] N. Liu, G. Giesen, M. Belov, , J. Losby, J. Moroz, A. E. Fraser, G. McKinnon, T. J. Clement, V. Sauer, W. K. Hiebert, M. R. Freeman, *Nat. Nanotechnol.* **3**, 715 (2008).

CHAPTER 4

Thermo-mechanical sensitivity calibration of nanotorsional magnetometers

The material presented in this chapter was published in the Journal of Applied Physics ***111****, 07D305 (2012) by J. E. Losby, J. A. J. Burgess, Z. Diao, D. C. Fortin, W. K. Hiebert, and M. R. Freeman.*

Abstract

We report on the fabrication of sensitive nanotorsional resonators, which can be utilized as magnetometers for investigating the magnetization dynamics in small magnetic elements. The thermo-mechanical noise is calibrated with the resonator displacement in order to determine the ultimate mechanical torque sensitivity of the magnetometer.

4.1 Introduction

The combination of improving nanofabrication and detection techniques, along with technological demand, are providing the means and impetus for further understanding of the micromagnetic structure and dynamics of small magnetic elements. The exquisite sensitivities of nano- and micromechanical resonators have recently been utilized for detecting quantum-limited displacements [1, 2] and ultra-sensitive atomic-scale mass detection [3, 4]. Nanomechanical torque magnetometry allows for direct measurements of single elements [5, 6], offering complementary information to other magnetometry methods, while also allowing for the investigation of details that are often indistinguishable when examining arrays of small elements or larger-scale thin films. Such events can be correlated to surface inhomogeneities and edge defects of the magnetic element, which play a dominant role on the overall magnetization configuration at smaller size scales. For understanding of the local energy landscapes of small magnetic elements, it is necessary to further increase the sensitivities of mechanical resonators.

The thermo-mechanical noise sets a fundamental limit for the sensitivity of resonant mechanical measurements. This Brownian motion is the result of the coupling of the mechanical subsystem to that of a dissipative reservoir, and is generalized as the fluctuation-dissipation theorem [7, 8]. This coupling causes the resonator to experience position fluctuations at its modes of mechanical resonance. Following equipartition, the observed mechanical resonance power spectrum must be proportional to the effective temperature of the mechanical mode. This relationship provides a method for torque sensitivity calibration of torsional resonators.

Here, we briefly present the fabrication procedure of a doubly-clamped nanomechanical resonator with a permalloy ($Ni_{80}Fe_{20}$) disk selectively deposited on a center paddle. A magnetic driving scheme, where the actuation of the resonator's torsional resonance modes are favored, is described and magnetometry measurements are presented. Using observations of the thermo-mechanical

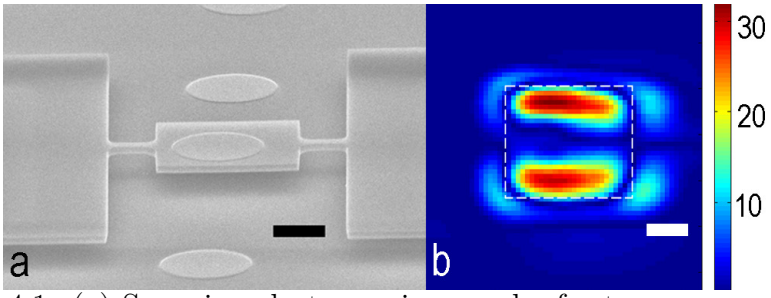

Figure 4.1: (a) Scanning electron micrograph of a torque magnetometer with a permalloy disk deposited on the paddle. The paddle width is w_p=5.8 µm and the width of the torsion rod is w_t=600 nm. The length of one torsion rod is l=1.8 µm and the device thickness is t=300 nm. (b) Spatial raster scan of the lock-in magnitude signal at the torsional resonance frequency of the resonator (top-down view), showing the maximum intensity at the free-edges of the paddle. The paddle position is indicated by the white dashed line. The colorbar scale is in mV_{RMS}. Both scale bars are 2 µm in length.

noise in the un-driven paddle resonators, we offer a calibration method to determine the mechanical torque sensitivity and consequently the magnetic moment sensitivity of the magnetometer, given the strength of the torquing field.

4.2 Torsional Resonator Fabrication

The completed torsional resonator is shown in Fig. 4.1a. The paddle resonators were fabricated from silicon-on-insulator (SOI) wafers with a 300 nm thick Si device layer and a buried silicon oxide (BOx) layer with a thickness of 1 µm. The geometry of an array of paddles was defined via electron beam lithography (EBL) using a negative tone resist (hydrogen silsesquioxane, HSQ). Following EBL resist development, the unmasked device layer was exposed to a reactive ion etch. A subsequent wet-etching of the BOx layer was done to release the resonators. The fabricated torsion bar width is 600 nm and the center paddle dimensions are 5.8 µm x 5.8 µm. A commercial silicon nitride membrane

(Electron Microscopy Sciences) with a square array of circular holes (12 µm pitch) served as a deposition shadow mask and was aligned above the device chip using a vacuum-tweezer micro-manipulator. Collimated electron beam deposition, under 10^{-10} Torr vacuum, of permalloy resulted in the placement of magnetic disks on the paddles of the resonators. The thickness of the disks are approximately 35 nm with a diameter of 3.2 µm, measured through scanning electron microscopy.

4.3 Device Actuation

The torque exerted on the magnetization of the permalloy disk by an external field acts as a mechanical load, resulting in the deflection of the resonator. In order to drive the torsional mode of the resonator, a bias field (provided by a permanent magnet housed on a motorized stepper rail) was oriented in-plane with the disk at a direction to induce a non-zero magnetization component orthogonal to the resonator length. A copper wire coil placed above the devices provided a small time-varying, out-of-plane "dither" field. A high frequency lock-in amplifier (Zurich Instruments Model HF2) provided the sinusoidal drive/reference signal in the range of the resonator's torsional resonance mode. The vertical displacement of the resonator was detected by taking advantage of optical interferometry. The SOI architecture allows for a controlled optical cavity spacing between the resonator and handle layer, providing the interferometric contrast for sensitive displacement measurements. The laser ($\lambda = 632nm$) was focused through an objective lens and the modulation of the reflected intensity was detected using a low-noise, RF photodetector (New Focus Model 1801). The measurements were taken in vacuum under a pressure of $\sim 10^{-6}$ Torr. A spatial raster scan of the interferometric signal is shown in Fig 4.1b., confirming the driving of the torsional resonance mode.

The acquired lock-in magnitude signal of the driven magnetometer is shown in Fig. 4.2 as a unipolar bias field was swept. A magnetic vortex hysteresis loop was captured, where the sharp transitions at the lower and higher

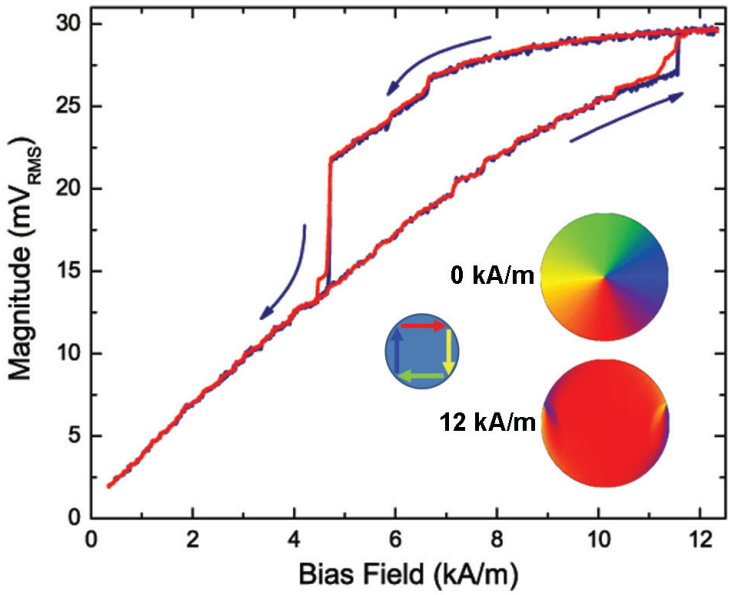

Figure 4.2: Magnetic vortex hysteresis loop in the permalloy disk. The dark blue trace is a single bias field sweep and the red trace is averaged for a $\sqrt{20}$ factor of noise reduction. The drive field was 150 A/m and the lock-in amplifier time constant was 120 ms. The results for the micromagnetic simulations of the disk are shown as colormaps, where the in-plane magnetization vector directions are represented by the color wheel.

fields represent the vortex creation and annihilation fields, respectively. The magnetization states at the different field regions are supported by Landau-Lifshitz-Gilbert based micromagnetic simulations of the hysteresis, shown in Fig. 4.2 at 0 and 12 kA/m. The dark blue trace is a single bias field sweep, while the averaged signal of 20 sweeps is shown in red. The reproducibility of the smaller-scale, Barkhausen-like transitions throughout the measurement, due to inhomogeneities within the permalloy disk, are seen in the single trace with sufficient signal-to-noise. These devices can possibly be implemented to probe and map the potential energy landscapes of small magnetic elements.

4.4 Thermo-mechanical Noise Calibration

With the driving field off, the thermo-mechanical power spectral density, $S_V(f)$, around the torsional resonance was acquired by sweeping the lock-in frequency, Fig. 4.3. The angular displacement spectral density of the thermal vibrations is given by,

$$S_\theta(f) = \frac{2k_BTf_0^3}{\pi k_{tor}Q}\frac{1}{(f_0^2 - f^2)^2 + (\frac{f_0 f}{Q})^2}, \tag{4.1}$$

where T is the effective temperature of the resonator, f_0 is the center frequency, and Q is the mechanical quality factor [9]. θ is the mean angular displacement of the paddle from its equilibrium position. k_{tor} is the torsional spring constant and is, for the resonator geometry, given by,

$$k_{tor} = \frac{4Gt^3(0.33w_t - 0.21t)(0.33w_p - 0.21t)}{0.33(2lw_p + w_pw_t) - 0.21t(2l + w_p)}, \tag{4.2}$$

where G is the shear modulus of the resonator material, t is the thickness, w_t is the width of the torsion rod, w_p is the width of the paddle, and l is the length of a torsion rod [10]. The equipartition theorem allows for the calibration of the power spectral density with the displacement spectral density,

$$\left\langle \theta^2 \right\rangle = \frac{k_BT}{k_{tor}} = \int_0^\infty S_\theta(f)df. \tag{4.3}$$

Solving Eq. 4.3 at $T = 295$ K using the calculated spring constant $k_{tor} = 2.35 \times 10^{-10}$ N m/rad. results in $\langle\theta\rangle = 4.16$ µrad., which equates to a mean edge displacement of the paddle from equilibrium as $\sqrt{\langle x^2\rangle} = 11.8$ pm. Solving Eq. (1) with (3) and assuming a Lorentzian form for the thermo-mechanical noise allows for the calibration of the theoretical displacement spectral density distribution on resonance, $S_x(f_0) = 2Q\left\langle x^2\right\rangle/\pi f_0 = 0.093\text{pm}^2/\text{Hz}$, to the power spectral density, $S_v(f_0)$, as shown in Fig. 4.3.

The responsivity and displacement sensitivity of the magnetometer can be calculated through the determination of the scaling factor, α, between $S_x(f)$ and

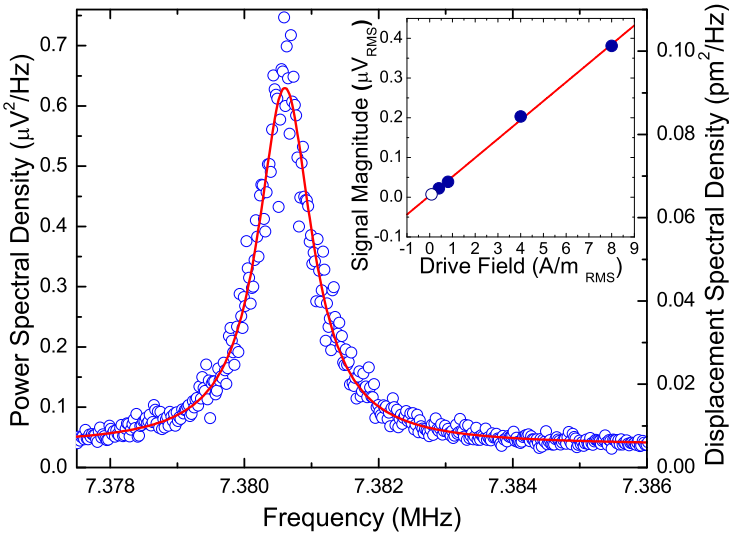

Figure 4.3: Frequency spectrum of the thermo-mechanical power spectral density, S_v, calibrated with the displacement spectral density, S_x. The scan is averaged 16x and the noise-equivalent bandwidth is 9.88 Hz. The solid red trace is a Lorentzian fit, where the values f_0=7.3806 MHz and Q=7775 were extracted. Inset: calibration of the signal magnitude to the driving field. The hollow circle is magnitude of the thermo-mechanical limit superimposed onto the linear fit, corresponding to a thermo-mechanically limited drive of 0.12 A/m.

$S_v(f)$ [11]. That is, $S_v(f) = S_v^{\text{white}} + \alpha S_x(f)$, where S_v^{white} is the white noise floor (the sum of the optical shot noise of the laser and the photodetector dark current). On resonance ($f = f_0$), 0.628 $\mu V^2 Hz^{-1}$ = 0.036 $\mu V^2 Hz^{-1} + \alpha 0.093$ $pm^2 Hz^{-1} \rightarrow \alpha = 6.32(\mu V/pm)^2$. The responsivity is defined as $R = \alpha^{1/2} = 2.5$ $\mu V/pm$. Using the scaling factor to convert S_v^{white} to the displacement spectral density noise floor, $S_x^{\text{white}} = S_v^{\text{white}}/\alpha = 0.0058$ pm^2/Hz, the displacement sensitivity of the cantilever off-resonance can be found, $(S_x^{\text{white}})^{1/2} = 75$ $fm/Hz^{1/2}$. The torque sensitivity away from resonance, upon conversion to an angular displacement, $\tau = k_{tor}\theta$, is 6.2 $aNm/Hz^{1/2}$. At mechanical resonance this value increases approximately by a factor of $\sqrt{Q}$ [12], which gives our magnetometer

a torque sensitivity of $\sim$ 70 zNm/Hz$^{1/2}$.

We define the figure-of-merit (FOM) as the scaling factor of the magnetic moment sensitivity of a thermally-limited magnetometer with driving field. The calibration of the linear signal magnitude with the torquing field is shown in the inset of Fig. 4.3. The thermo-mechanical limit, represented by the hollow circle superimposed onto the linear fit, corresponds to an AC drive field of $H_{tm} = 0.12$ A/m. With the conservative assumption that all of the magnetic moments contribute to the drive at this field, the FOM is then $M_S V \times H_{tm} \sim 2.5 \times 10^9$ μ_B (A/m), where $M_S = 800$ kA/m is the saturation magnetization of permalloy and V is the volume of the disk. For our measurements (Fig. 4.2) the driving field was 150 A/m, leading to a moment sensitivity of $FOM/150$ (A/m) $= \sim 1.5 \times 10^7$ μ_B. A conversion to a torque yields $\boldsymbol{\tau} = \boldsymbol{m} \times \mu_0 \boldsymbol{H} \sim 26.2$ zNm, which is on the order of our mechanical torque sensitivity. The dynamic range of the moment sensitivities ranges from $\sim 2 \times 10^{10}$ μ_B at the thermo-mechanical limit to $\sim 4 \times 10^6 \mu_B$ at the maximum driving field (600 A/m) of our instrumentation. This is approximately an order-of-magnitude improvement in sensitivity to comparable torque magnetometry studies at room temperature using low applied fields [6, 5, 13].

4.5 Conclusion

In this study the fabrication of sensitive nanotorsional magnetometers for the study of single magnetic elements was described, along with magnetometry results of a permalloy disk with a ground-state magnetic vortex. The post-fabrication deposition of the magnetic material provides the added benefit of the magnetic disk remaining relatively 'clean' (that is, unaffected by acid or plasma etching processes that occur during the resonator fabrication). The resonators also provide a sensitive platform for the study of various deposited magnetic materials. We have also demonstrated the capability of calibrating the measured thermo-mechanical noise with the theoretical resonator displacement to determine the ultimate torque sensitivity of the resonators. Through

the tuning of the resonator geometry and transduction scheme it is possible to further enhance the sensitivities of these devices.

Bibliography

[1] A. D. O'Connell, M. Hofheinz, M. Ansmann, R. C. Bialczak, M. Lenander, E. Lucero, M. Neeley, D. Sank, H. Wang, M. Weides, J. Wenner, J. M. Martinis, A. N. Cleland, *Nature* **464**, 697 (2010).

[2] J. D. Teufel, T. Donner, J. W. Harlow, M. S. Allman, K. Cicak, A. J. Sirois, J. D. Whittaker, K. W. Lehnert, R. W. Simmonds, *Nature* **475**, 359 (2010).

[3] M. Li, W. H. P. Pernice, H. X. Tang, *Nat. Nanotechnol.* **4**, 377 (2009).

[4] H. Y. Chiu, P. Hung, H. W. C. Postma, M. Bockrath, *Nano. Lett.* **8**, 4342 (2008).

[5] J. P. Davis, D. C. Fortin, J. A. J. Burgess, W. K. Hiebert, M. R. Freeman, *Appl. Phys. Lett.* **96**, 072513 (2010).

[6] M. D. Chabot, J. Moreland, *J. Appl. Phys* **93**, 7897 (2003).

[7] H. B. Callen, T. A. Welton, *Phys. Rev.* **83**, 34 (1951).

[8] H. Nyquist, *Phys. Rev.* **32**, 110 (1928).

[9] J. S. Bunch, A. M. van der Zande, S. S. Verbridge, I. W. Frank, D. M. Tanenbaum, J. M. Parpia, H. G. Craighead, P. L. McEuen, *Science* **315**, 490 (2007).

[10] N. Lobontiu, B. Ilic, E. Garcia, T. Reissman, H. G. Craighead, *Rev. Sci. Instrum.* **77**, 073301 (2006).

[11] W. K. Hiebert, D. Vick, V. Sauer, M. R. Freeman, *J. Micromech. Microeng.* **20**, 115038 (2010).

[12] A. N. Cleland, *Foundations of Nanomechanics - From Solid-State Theory to Device Applicatins* (Springer, Berlin, 2003).

[13] J. Moreland, *J. Phys. D: Appl. Phys.* **36**, R39 (2003).

CHAPTER 5

Nanomechanical characterization of a three-dimensional micromagnetic vortex state in a single-crystal yttrium iron garnet disk

Some of the material presented in this chapter is in preparation for submission to a peer-reviewed journal by J. E. Losby, Z. Diao, F. Fani Sani, D. T. Grandmont, L. C. Parsons, J. A. J. Burgess, T. Firdous, M. Belov, D. Vick, W. K. Hiebert, and M. R. Freeman. A discussion of the lack of Barkhausen noise (within our experimental resolution) in YIG is presented in Appendix B.

Abstract

Although most of the recent research in nano- and micromagnetism has been focused on one- or two-dimensional systems, three-dimensional magnets can also provide benefits in technological applications and offer additional understanding of the effects of spatial confinement on magnetic properties. To date, the controlled shaping and measurement of pristine three-dimensional mesoscale magnets is limited due to their fabrication techniques not being amendable to traditional lithographic processing. Here, the magnetostatic characterization of an individual, single-crystalline yttrium iron garnet micromagnetic disk is reported. The disk is sculpted from a bulk single crystal by focused ion beam milling, and transferred to a nanomechanical torsional resonator. The crystalline orientation is such that a (111) direction is perpendicular to the disk surface. This places a magnetocrystalline easy axis in alignment with the core of the magnetic vortex state, and the other three easy axes associated with the cubic anisotropy in threefold rotation about the cylinder axis, canted by 19 degrees from the plane of the disk. Nanomechanical vector torque magnetometry was performed to probe both the in- and out-of-plane components of magnetization in the disk. At low fields the disk

exhibits non-hysteretic, linear magnetizing curves with no remanence for both components, as expected from a 3D vortex. In angular measurements of magnetic hysteresis as a function of the in-plane direction of applied magnetic field, it is observed that the field strengths at which vortex annihilation transition occur are significantly less sensitive to magnetic anisotropy than are the vortex nucleation fields. The same measurements may also reveal the presence of magnetic edge roughness around the location where the disk was detached from the nanomanipulator, manifest as high variability of the transition fields over the corresponding range of field angles. Overall, the comprehensive magnetostatic measurements of the individual disk yield an incisive determination of the degree to which ideal micromagnetic response has been approached in the manufactured structure, and of the role of magnetocrystalline anisotropy on vortex behavior. Mastery of experimental monocrystalline manufacturing and measurement will enable new directions in micromagnetics, through control of the interplay of uniform anisotropy fields with magnetization textures. The substantial elimination of background disorder and concomitant Barkhausen-free magnetization response is also promising for experimental studies requiring sensitivity to very small energetic changes, possibly to the level as could be explored by quantum fluctuations.

5.1 Introduction

Driven both by technological necessity and fundamental scientific curiosity, there has been intensive investigation into understanding how geometric confinement affects the magnetization distribution in micromagnetic elements. Such magnetic systems have allowed for spintronics applications [1, 2, 3] and are also ideal platforms for probing mesoscale magnetic phenomena (which are hindered by inhomogeneities exhibited in the magnetization of larger, multi-domain structures) such as vortex dynamics in disks and ellipses [4, 5, 6] and domain wall motion in thin wires [7].

In recent years research has been predominantly confined to one- or two-dimensional magnetic systems, such as nanowires or shape elements derived from thin-film processing techniques. The magnetization and magnetic properties that are a result of spatial confinement in three-dimensional mesoscale systems is still relatively unexplored, although some fascinating experimental [8, 9, 10] and theoretical [11, 12] studies exist.

A reason for this is the difficulty encountered in fabricating magnetic elements that have size scales in all three spatial dimensions in the range of hundreds of nanometers, but not so large that the magnetic microstructure becomes too complex for controlled technological application or micromagnetic model results become suspect. Previous studies have incorporated arrays of three dimensional structures created using electro-deposition methods [13, 14], thick films created from templated self-assembly methods [15], and Fe islands created using pulsed laser deposition techniques [16]. Although providing good insight, there is also a clear need for complementary, detailed measurements of the three-dimensional magnetization response of an isolated, single element. The latter is a necessity, both for understanding how the magnetization is affected by local structural variation (information that is often blurred when measuring arrays) and as a precursor to integration with nanoscale devices.

The ferrimagnetic insulator yttrium iron garnet (YIG) was selected as the magnetic material for this study. YIG has enjoyed wide-scale application in optical

communication and analog signal processing, due to its excellent performance in Faraday isolators and as broadband, magnetically-tunable, microwave oscillators [17, 18]. More recently the field of spintronics, and specifically energy applications in the magnonics of thermally-generated spin imbalances, has pushed a resurgence of research interest in YIG [19, 20, 21]. As a consequence of its low magnetic damping (with the narrowest known ferromagnetic resonance linewidth), spin wave propagation in single-crystal YIG can be observed on centimeter length scales with magnon lifetimes of hundreds of nanoseconds [22]. Such pure spin currents have been exploited as sources for spin transfer torque across insulating magnet-normal metal heterostructures [23, 24] and also in magnonic crystals [25, 26]. The benefit of the low magnetic losses in YIG will allow for their continued implementation in future devices, such as couplers of quantum qubit systems through long range magnetic dipolar interactions [27].

YIG holds promise as a model nanoscale system to examine fundamental quasi-static and dynamic magnetization processes and for their fully quantitative comparison to theory and modeling. Most top-down nanomagnetic elements are produced using processes involving thin-film deposition and patterning, derived from the heritage of integrated circuit fabrication. The vast majority of resulting structures feature polycrystalline material morphologies, giving rise to a myriad of phenomena arising from the concomitant local variation of magnetic properties, including domain wall and vortex core pinning [28, 29, 30]. Such events can be observed as Barkhausen transitions within the magnetization-versus-field hysteresis [31]. Dynamically, crystalline and geometric defects/edges can affect spin wave propagation through surface and volume scattering effects [26, 32, 33, 34]. A complementary class of monocrystalline model structures, lacking magnetic pinning sites introduced by crystalline grain boundaries and other imperfections, would be highly desirable and ultimately allow for control of their quasi-static and dynamic magnetic properties.

This letter describes the prototyping and characterization of a single-crystalline

micromagnetic disk by focused ion beam (FIB) milling of epitaxial thick-film YIG and the successful attachment of this structure to a nanomechanical resonator for torque magnetometry measurements. The ground state of the three-dimensional disk (radius = 600 nm and thickness = 500 nm) exhibits a magnetic vortex through the disk axis, with a broadened core through its thickness. The disk was sculpted such that magnetocrystalline easy axis (111) is normal to the disk surface and aligned with the core. The other three easy axes associated with cubic anisotropy exhibit a threefold symmetry about the disk axis. Torque magnetometry was done to probe both the in- and out-of-plane components of magnetization.

5.2 Device Fabrication

Prior to FIB processing, a YIG crystal (108 µm thickness, grown via liquid-phase epitaxy on a gadolinium gallium garnet substrate [35]) was polished (1 µm grit size) to produce a sharp ninety-degree edge, and then coated with 5 nm of carbon to reduce charging effects during ion milling. A trapezoidal back-trench (on the left in Fig. 5.1a) was first milled to create a YIG wall of width 3.5 µm at the edge of the crystal. The back-trench served as an avenue of escape for the material sputtered away during subsequent milling steps. The crystal was rotated ninety degrees and a similar cavity was milled 1 µm from the other edge. The resulting suspended bar of YIG was thinned to 500 ± 10 nm. A disk with a design radius of 650 nm was then defined by milling a circular channel through the bar, with the ion beam at normal incidence to the crystal surface (Fig. 5.1a). Because of the Gaussian profile of the ion beam, the final measured radius of the disk was 600 ± 20 nm. The milling strategy described here is designed to avoid any direct dose to the final structure other than from the Gaussian wings of the ion beam when the outline of the disk is defined. It has been shown that during the fabrication process to produce the initial free-standing YIG bar, the implantation damage is confined to a layer conservatively under 40 nm [36].

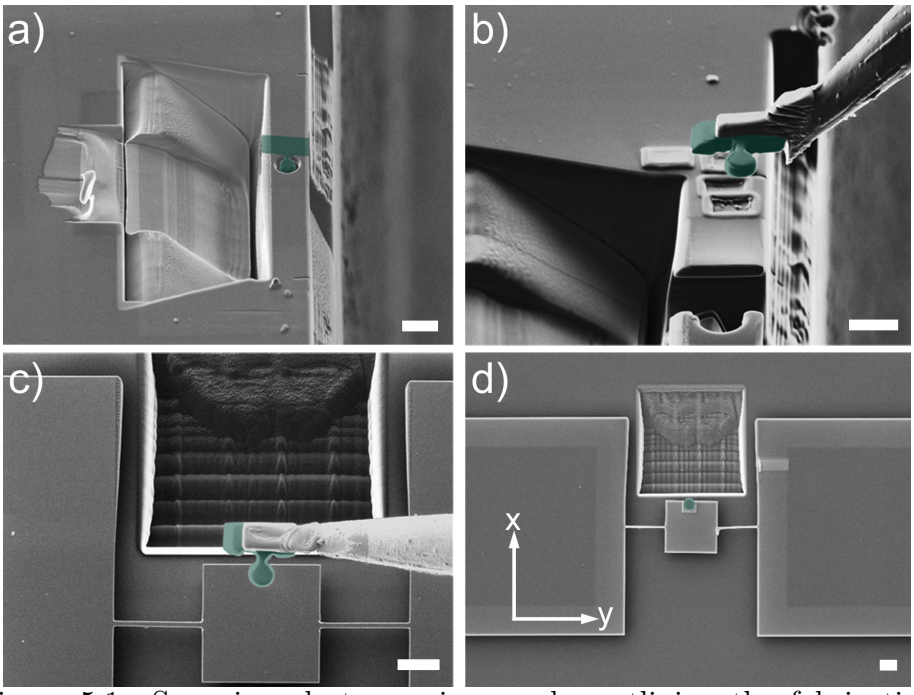

Figure 5.1: Scanning electron micrographs outlining the fabrication process of a torque magnetometer housing a single-crystal YIG micromagnetic disk. (a) The circular trench was defined in the thinned suspended YIG beam by three-dimensional FIB milling. A nanomanipulation probe was attached to the section of the YIG beam (false-colored) adjacent to the disk and the section was removed for transfer to a prefabricated torsional resonator, (b). (c) Top-down image during the approach of the YIG disk onto the resonator. (d) The completed magnetometer after the disk was bonded to the resonator by electron beam-assisted platinum deposition and released from the nanomanipulation probe. All scale bars are 2 µm.

However it is expected that, for a material like garnet, the resultant *magnetic* disk is effectively somewhat smaller than the outside dimensions of the material structure, being encapsulated in a non-magnetic, ion-damaged "dead layer". A tab was left on the edge of the disk for the attachment of a nanomanipulation probe, which was bonded to the YIG bar using an electron-beam induced deposition of platinum from an organometallic precursor gas ((Trimethyl)methylcyclopentadienylplatinum(IV)). This deposition is mediated by secondary electrons which arise from both ion and electron flux, but the electron beam was employed here to minimize ion damage to the specimen. The disk was released from the YIG bar by three small cuts around the manipulator attachment site and transported (while still in the FIB chamber, see Fig. 5.1b), to a silicon torsional resonator.

The mechanical resonator was prefabricated through electron beam lithography and etching of a silicon-on-insulator chip (device thickness = 300 nm, torsion bar width = 300 nm, BOx layer = 1µm). The only FIB modification to the SOI device prior to attachment of the disk was the creation of a cavity in the silicon handle layer to ensure that the micro-manipulator did not contact the substrate. The probe was carefully aligned using alternating FIB and SEM imaging until contact was made with the center paddle, Fig. 5.1c. To ensure minimal ion damage to the resonator, the FIB images were taken with very low current (∼1 pA) and a high scan speed. The two beams provide two imaging perspectives differing by 54 degrees, enabling precise determination of the paddle-disk separation in three dimensions. Once in contact, the YIG disk was attached to the paddle with a platinum film overlapping both the disk and resonator. The attaching stem was finally cut by the FIB, resulting in the completed magnetometer (see Fig. 5.1d).

5.3 Electron Diffraction

The monocrystalline nature of the FIB-sculpted YIG was confirmed by selected area electron diffraction with a transmission electron microscope op-

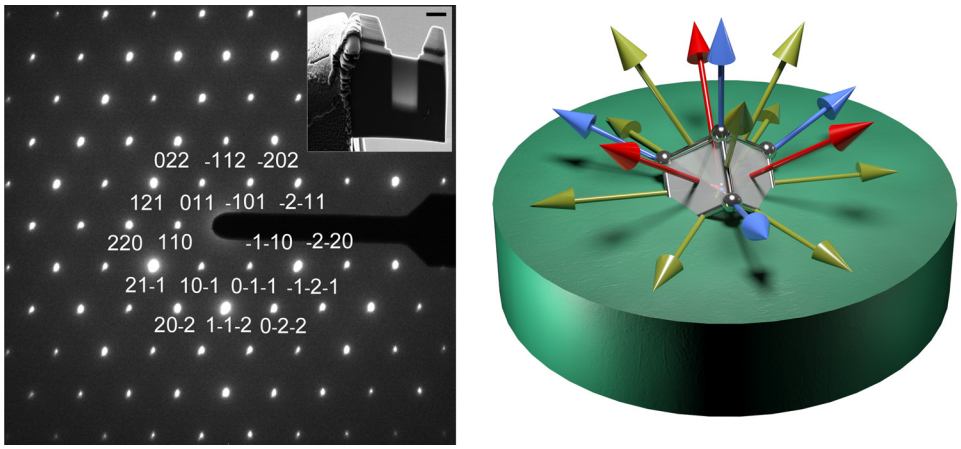

Figure 5.2: Electron diffraction of a YIG reference lamella and crystal structure. The lamella was thinned to about 250 nm to allow for the transmission measurement. Left: Crystal structure of the YIG (inset) acquired with selected area electron diffraction over most of the thinned section. The (h,k,l) crystal plane indices are indicated, consistent with the (111) orientation (the zone axis normal to the disk surface) of the YIG sample. Right: Schematic of the YIG disk showing the cubic anisotropy easy (blue), hard (red), and medium (yellow) axes directions.

erating at 300 kV (Hitachi HF 3300 FE-TEM), Fig. 5.2. A YIG reference lamella was FIB-milled from the same bulk substrate as the disk and thinned to 250 nm for the transmission measurement (Fig. 5.2 inset). The lamella was micromanipulated onto to a copper TEM sample grid in the same method as described previously. The well-defined hexagonal Laue peaks representing an ordered cubic structure are consistent with the (111) crystal orientation (in the direction normal to the disk surface) in YIG, which was also used as the zone axis for plane indexing. For the YIG disk attached to the mechanical resonator, the crystal alignment of the (110) orientation is perpendicular to the torsion bar axis. An accurate placement of single-crystal microstructures is a necessity for studies examining the role of magnetocrystalline anisotropy. We estimate (from the specifications of the YIG wafer [35] and analysis of micrograph images) the upper limit of rotational alignment error to be 1.5 degrees. A schematic of the YIG disk with a the easy, medium, and hard axes

superimposed is shown in the right side of Fig. 5.2.

5.4 Nanomechanical vector torque magnetometry

The mechanical resonator was driven through an alternating torque exerted on the YIG disk by an AC magnetic field. The AC magnetic torque has a contribution $\boldsymbol{\tau_1}^{AC} = \boldsymbol{m}^{DC} \times \mu_0 \boldsymbol{H}^{AC}$, where $\boldsymbol{m} = \int_{vol} \boldsymbol{M} dV$ is the net magnetic moment of the disk and $\boldsymbol{M}$ is the position-dependent magnetization. In addition, there is a second contribution of the same order of magnitude, from the AC response of the magnetization parallel to the alternating field: $\boldsymbol{m}^{\boldsymbol{AC}} = \chi V \boldsymbol{H}^{AC}$, where $\boldsymbol{\tau_2}^{AC} = \boldsymbol{m}^{AC} \times \mu_0 \boldsymbol{H}^{AC}$. (This differs from the situation for thin film Permalloy structures studied earlier, where the shallow aspect ratio and high saturation moment combine to yield demagnetizing fields strong enough to make the second term negligible in the case of perpendicular AC excitation.)

For field-sweep measurements, the magnetization was biased by external magnetic fields either in- or out-of-plane to the resonator surface (H_x and H_z directions shown in Fig. 5.1d) and AC driving fields were supplied by small copper coils perpendicular to the bias field direction, respectively along the z and x axes. This configuration allows for vector magnetometry measurements, where both the in- and out-of-plane components of magnetization in the disk can be torqued to drive the fundamental torsional mode of the resonator. The AC field frequency was set to the fundamental torsional resonance of the magnetometer to provide maximum sensitivity. The sample was placed under a vacuum of $\sim 10^{-5}$ Torr and measurements were conducted at room temperature. Vertical displacement was recorded by lock-in detection (Zurich Instruments HF2LI) of the AC modulated optical reflection (HeNe laser light source, $\lambda = 632$ nm). Interferometric contrast is created by the low-finesse etalon between the device paddle and handle layer.

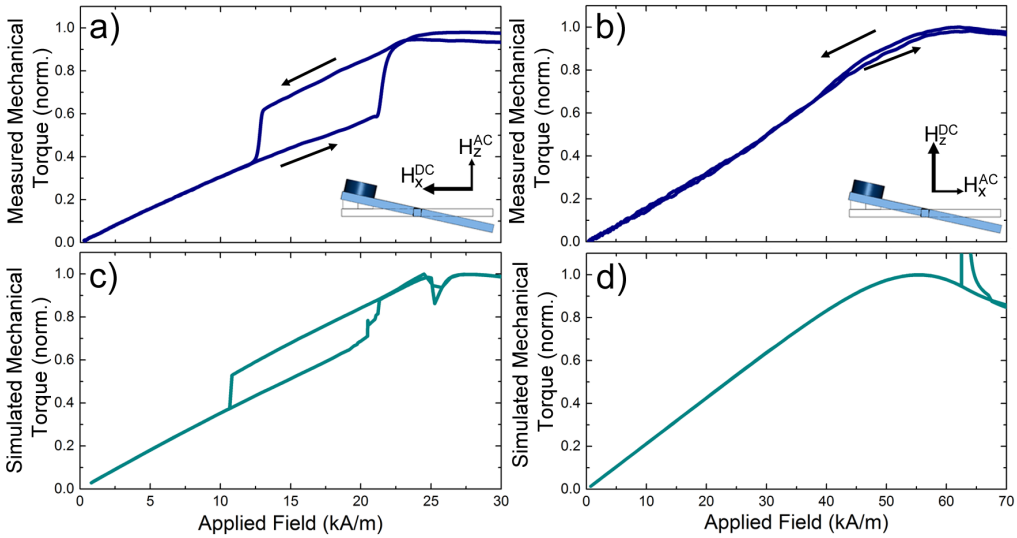

Figure 5.3: Nanomechanical vector torque magnetometry results and micromagnetic simulation of magnetization evolution with field in the YIG disk. (a) The in-plane component was measured by sweeping a DC bias field in-plane to the disk while an orthogonal AC field was applied in a direction normal to the disk surface, as described in the inset. The induced torque on the magnetization results in a mechanical deflection of the resonator. Similarly, by sweeping an out-of-plane DC field and applying an AC field in the x-direction, the out-of-plane component of magnetization can be measured (b). The simulated torque responses are shown in (c) for the in and (d) out-of-plane components of magnetization. These simulations were done for the cases of no magnetocrystalline anisotropy.

The combined $M_{x,z}$, $\chi_{z,x}$ components are measured by sweeping the $H_{x,z}^{DC}$ bias field while driving with an orthogonal $H_{z,x}^{AC}$ field (schematic in inset, Fig. 5.3 a,b). The deflection amplitude of the resonator as a function of bias at low field are shown in Figs. 5.3a and 5.3b for the measured components, respectively. The low field response of the measured components of magnetization can be directly compared to results from simulation after normalization, as shown in Fig. 5.4. The initial, constant slopes at low fields show close agreement for both cases. The departure to lower susceptibility at higher fields in the measurements brings forth an interesting comparison to recent measurements done on thinner disks, attributing it to the anharmonicity of the vortex core potential well [37]. The simulations for this case were performed without including magnetocrystalline anisotropy terms, using open source GPU-based simulation code to tackle the 3D structure in much shorter computation times [38] [1]. The anisotropy terms have a large influence on the field positions of transitions in the magnetization curves as discussed in more detail later, but relatively little on the initial slopes. In addition, as would be expected in a monocrystalline structure, the magnetization traces are free of Barkhausen effect signatures associated with grain boundaries or crystalline imperfections (further discussed in Appendix B).

The full field sweeps through maximum signal and beyond are shown in Figs. 5.3a and 5.3b for the in and out-of-plane components, respectively. A unipolar hysteresis loop is evident in the in-plane component measurement, similar to what is observed in 2D disk structures (where the sharp transitions in higher and lower field represent the vortex annihilation and nucleation fields, respectively). Unlike the 2D case, during the field sweep-down from high bias here the net moment has a sizeable field dependence even before the core nucleation event. This is a consequence of the 3D magnetization texture. Micromagnetic simulation (Figs. 5.3c) confirms that this dependence is in the M_x contribution and not the χ_z term. These features are captured in Landau-Lifshitz-Gilbert-based micromagnetic simulations [38] without including magnetocrystalline

[1] The computation parameters used are M_S=140 kA/m, grid size= 6.25 nm × 6.25 nm × 9 nm, exchange stiffness constant 2 × 10^{-12} J/m, and a damping factor of 1.

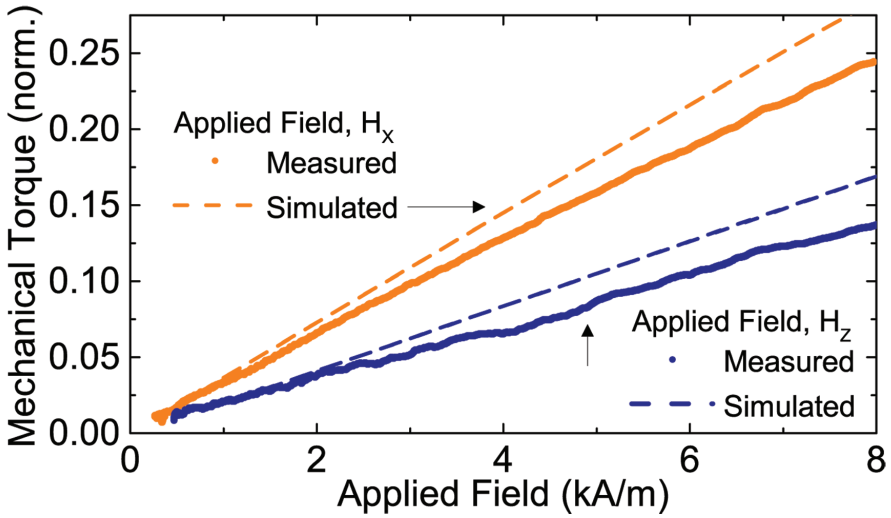

Figure 5.4: The low-field components of magnetization compared to simulation results. The initial susceptibilities are in very close agreement, offering confirmation that the ground-state magnetization structure in the YIG disk is similar to micromagnetic simulation results.

anisotropy terms. The out-of-plane component shows little or no hysteresis, though saturation is achieved.

The components of magnetic susceptibility orthogonal to the bias field direction (along the direction of the driving fields), χ_z and χ_x, are also taken into account in simulation in order to represent the torque magnetometry measurement. The simulation procedure applies a small sawtooth dither field along the bias field direction and fits the response to extract the relevant susceptibility value. There are no free parameters in the simulations and the result is only qualitative agreement with experiment. A unipolar hysteresis is observed for the in-plane field component, with transitions occurring at fields similar the experimental results. The "dip" in the high field region of the simulated in-plane loop is from a softening of M_z (increase of χ_z) near a buckling transition, and is observed in measurement along some bias field directions.

The large peak at high field in the M_z simulation field sweep-up is another occurrence related to more abrupt changes in the numerical derivative of the z-

component of magnetization. Only when such changes have a reversible (AC) component will they be detected by the lock-in measurement. Again, qualitatively similar features are sometimes observed. (In the following chapter, AC susceptometry measurements were developed and performed on the same YIG disk, in part to provide an experimental means of discriminating the reversible and irreversible contributions to otherwise ambiguous slope variations in the magnetization curves.) Recently, we have converted to another micromagnetics package [39] and simulations (including cubic anisotropy) are on-going at the time of this writing.

To examine the effect of anisotropy on the 3D magnetization texture in the YIG disk, full hysteresis loops were recorded in a dense set of measurements as a function of the in-plane direction of bias field. This was achieved through a combination of stepper rail, sample, and bias field polarity rotations while carefully maintaining the respective angular orientation of the field to the torsion rod of the device. Full hysteresis loops were done, with an angular resolution of approximately 1.5° and are shown in Fig. 5.5 for the full 360° rotation. The 0° position refers to the case where the bias field direction is perpendicular to the torsion rod of the resonator and the increasing angles designate a clockwise field orientation around the disk. The center of the plot is the zero-field position, while the outer edge represents the maximum field magnitude, 25 kA/m. The sweeps of increasing field were subtracted from the sweeps down in order to emphasize only the open part of the loop: the inner and outer boundaries of the blue area correspond to the vortex nucleation and annihilation fields, respectively.

One of the evident qualitative features is the striking departure from rotational symmetry (angular independence) of the nucleation fields, indicating the possibility that the magnetocrystalline anisotropy (ie. the directions of the magnetic easy, medium, and hard axes) play a role in affecting the transition from the quasi-single domain state (at the high field saturation) to the vortex state. The annihilation fields, on the other hand, appear not to be affected significantly. The competition and cooperation of anisotropy with the

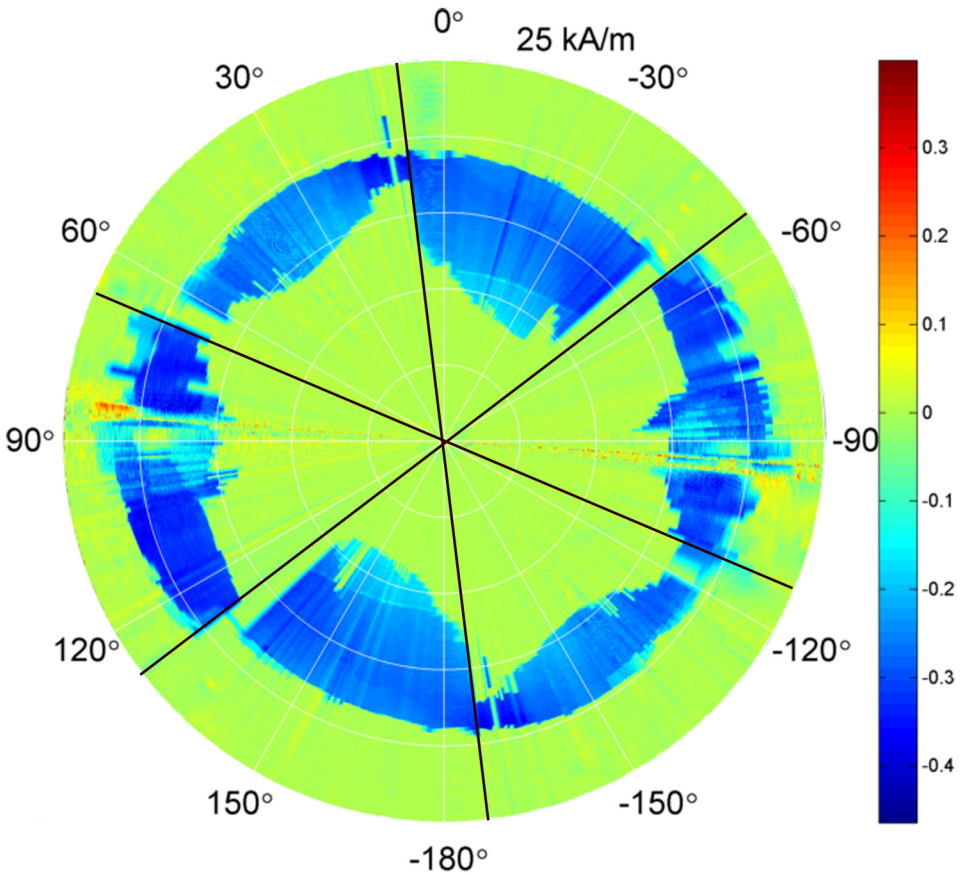

Figure 5.5: Hysteresis measurements of the YIG disk as a function of in-plane bias field direction. The 0° position refers to the $\boldsymbol{H_x^{DC}}$ bias field perpendicular to the torsion rod (along the x-direction in Fig. 5.1d) and the increasing angles correspond to a clockwise bias field rotation. At each rotation angle, full hysteresis loops were done between 25 kA/m (outer edge of the plot) to 0 kA/m (plot center). The upward field sweeps were subtracted from the downward sweeps to accentuate the width of the hysteresis loops (between the vortex annihilation and nucleation fields) with the rotational bias field. The angular resolution is approximately 1.5° and a total of about 1800 loops were taken. Each loops consists of an average of 4 to 8 sweeps, depending on the torque magnitude (signal to noise). The black lines are a guide to the eye indicating a possible six-fold symmetry due to the contribution of cubic anisotropy. The colour scale is arbitrary.

other energy terms is subtle. The magnetocrystalline anisotropy modifies the energy of the states on both sides of a transition, but at lower fields it is a proportionally larger fraction of the total energy. At approximately the 90° and −90° orientations, where the field is nearly-parallel to the torsion rod, the transition fields become more scattered with angle. We attribute this to magnetic edge roughness along the section of disk edge where the nanomanipulation handle was detached (see Fig. 5.1), as the vortex is nucleated and traverses the disk approximately 90° to the applied field direction. The orientation of the anisotropy axes with respect to the disk (see Fig. 5.2) further add complexity to analysis, owing to the alternating easy and hard axes not being in the plane of the disk, but instead alternating above and below. A possibility of a six-fold symmetry exists due to this configuration, indicated roughly by the thin black line in Fig 5.5 offset by 6.5° to features in the plot where the region between the creation and annihilation fields become narrow. It is likely that the effects of shape anisotropy contribute to additional features observed. A full illumination of the effects of the magnetocrystalline anisotropy on the vortex nucleation, annihilation, and other transitions in the magnetization texture will require a significant amount of additional simulation, and confirmation through measurement of a large enough number of samples to statistically separate the controlled and uncontrolled aspects of the fabrication procedure, and to iterate towards more complete control.

5.5 The Effects of Magnetocrystalline Anisotropy on the Magnetic Ground State

The ground state magnetization distributions for the YIG disk geometry as obtained from LLG-based micromagnetic simulations [40] are shown in Fig. 5.7. Simulations were performed for four specific cases: (i) no cubic magnetocrystalline anisotropy; and also by orienting (ii) an easy; (iii) a medium; and (iv) a hard axis along the direction perpendicular to the disk surface (schematically

shown in Fig. 5.6)[2] . The common feature in each case is the magnetic vortex that arises from the competition of exchange and demagnetization energy similar to that of a two-dimensional vortex pattern found in thin disks.

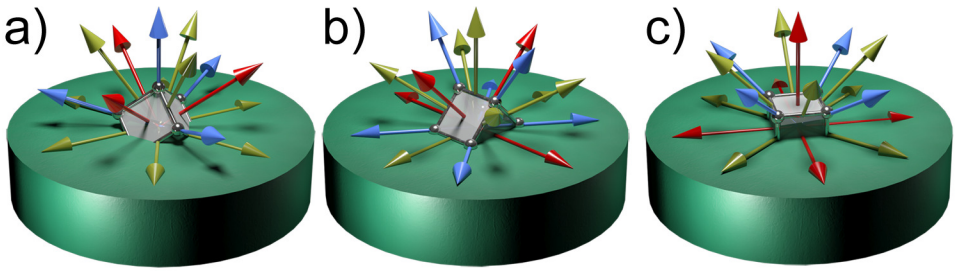

Figure 5.6: Illustrations of the various orientations of the magnetocrystalline anisotropy axes along the cylinder axis (z-direction) of the YIG disk, which can be tuned through the orientation of the micromachined bulk single crystal.

However, the aspect ratio of the YIG disk permits topological variation, allowing for a richer structure in the overall magnetization. In each case, the vortex core is broadened through the center of the disk. In the geometry corresponding the the experiments (easy axis along z), the anisotropy remarkably favours a "2D-ness" of the vortex texture familiar from thin films: the core becomes sightly less bowed; and a skew of the in-plane circulating component of magnetization across the thickness (a demagnetizing energy effect apparent without anisotropy) is reduced by the tilting towards the three easy axes angled only 19 degrees out-of-plane (a slightly buckled hexagon is a crude but still reasonable approximation of a circle). A secondary feature, existing mostly in the configuration where the hard axis is along the z-direction, is that of a revolved Landau state around the central axis of the disk. On the faces, to varying degrees for each case, the radial magnetization of the revolved Landau state mixes with the curling magnetization of the vortex pattern, particularly near the centre of the disk. Such topological features have been shown in ferromagnetic stacks of Co and Py separated by Rh, which mediates the strong

[2]The simulation parameters used are M_S=140 kA/m, grid size=10 nm^3, exchange stiffness constant 2×10^{-12} J/m, cubic anisotropy values of K_1=-6.1 x 10^{-4} J/cm^3 and K_2=-2.6 x 10^{-5} J/cm^3, and a damping factor of 1.

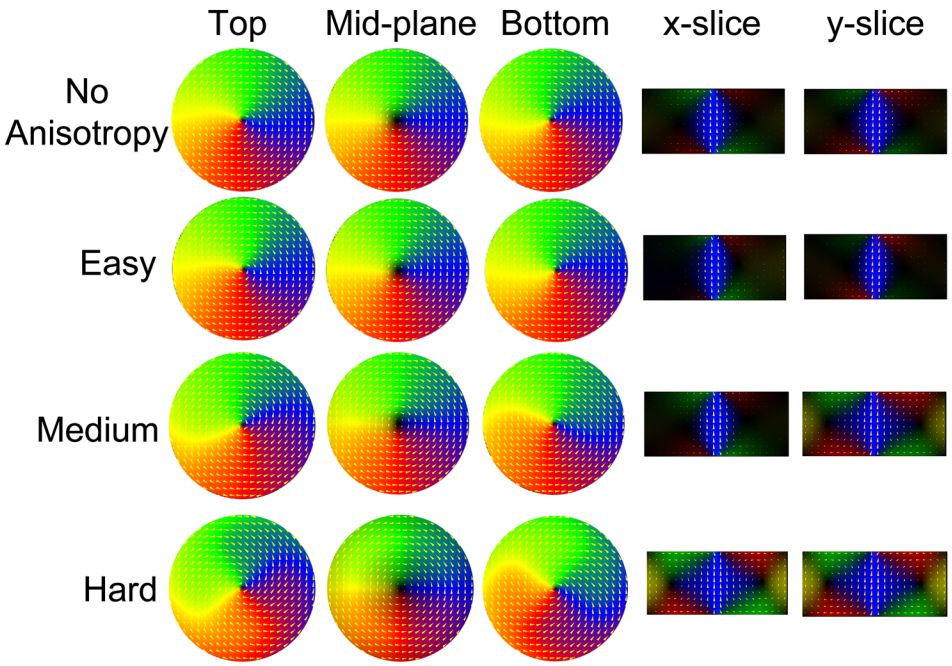

Figure 5.7: Landau-Lifshitz-Gilbert based simulation results of the ground state magnetization configuration of the YIG disk with no anisotropy and with the easy, medium, and hard axes along the disk (z) axis. The top face (z=500 nm), middle plane (z=250 nm), and bottom faces (z=0) are shown, respectively, along with the slices through the center of the disk through the x and y directions.

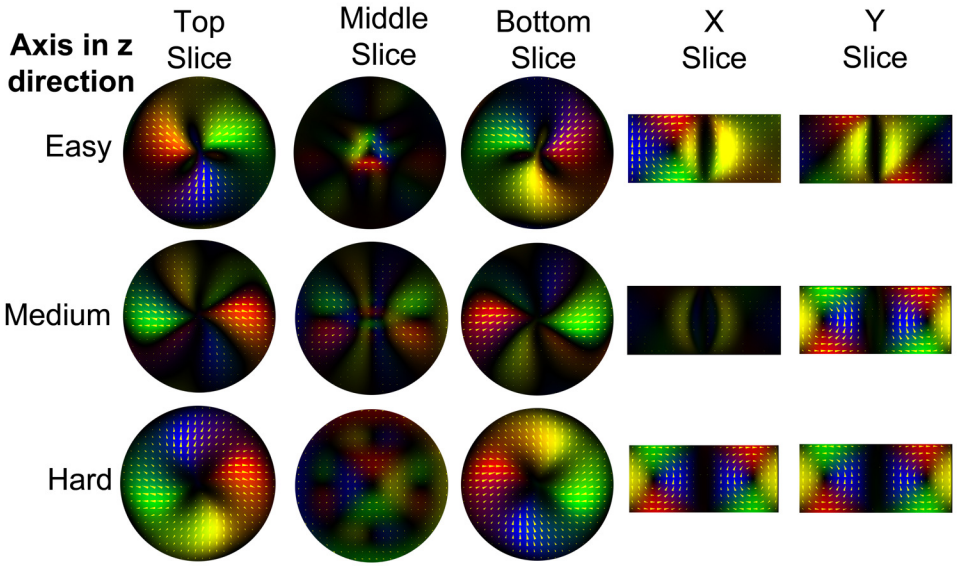

Figure 5.8: The subtractions of the LLG simulation results in 5.7 using no magnetocrystalline anisotropy from the cases where the easy, medium, and hard axes are along the z-axis. The scale for $|\boldsymbol{M}|/M_s$ are: 0 to 0.3616 for the easy axis, 0 to 0.3411 for the medium axis, and 0 to 0.5615 for the hard axis; all along the z-direction.

antiferromagnetic interlayer exchange coupling between the layers [41]. Here, the simulation results show the possibility manipulating such magnetization textures by simply milling a disk out of a bulk single crystal in a different orientation respective to the magnetocrystalline anisotropy directions.

In Fig. 5.8, the LLG simulation using no cubic anisotropy was subtracted from the different axes directions, as shown in 5.7 to further accentuate the effects of anisotropy on the magnetic structure. Here, the interplay of the various anisotropy fields leads to various symmetries associated with the combination of easy and hard axes. With the fabrication process outlined above, it will possible to micro-machine a YIG (or other monocrystalline material from bulk) disk with different configurations of the crystal axes along the cylinder axis. This would allow for additional tuning of both magnetostatic and dynamic properties of the magnetic vortex.

5.6 Summary

In summary, we have demonstrated the sculpting of a three-dimensional micromagnetic disk from bulk single crystal YIG, including its transfer onto a sensitive nanoscale mechanical resonator using a FIB instrument. The magnetic ground state features a vortex with a broadened core through the disk thickness. Nanomechanical vector torque magnetometry measurements probing the M_x and M_z components of magnetization are in qualitative agreement with results given by Landau-Lifshitz-Gilbert based micromagnetic simulations. Hysteresis measurements, where the in-plane bias field is rotated around the disk, show a symmetric relation of the nucleation fields likely due to the effects of cubic magnetocrystalline anisotropy, while the annihilation field is not as affected with rotation angle.

The fabrication technique and comprehensive set of measurements described here opens a way to laboratory investigations of a new class of model, monocrystalline structures in which the role of magnetocrystalline anisotropy can be exploited to further tune the magnetostatic and dynamic magnetization responses in mesoscale materials. The technique also generalizes well beyond the specific ferrimagnetic insulator material considered here. By allowing the shaping and manipulation of a material, the process can be applied to a large variety of bulk single crystal and epitaxially-grown layered materials (which are not amenable to traditional lithography techniques) in addition to island-like structures, which could be isolated and measured singularly.

Bibliography

[1] S. S. P. Parkin, M. Hayashi, L. Thomas, *Science* **320**, 190 (2008).

[2] F. J. Jedema, A. T. Filip, B. J. van Wees, *Nature* **410**, 345 (2001).

[3] S. Nadj-Perge, S. M. Frolov, E. P. A. M. Bakkers, L. P. Kouwenhoven, *Nature* **468**, 1084 (2010).

[4] J. P. Park, P. Eames, D. M. Engebretson, J. Berezovsky, P. A. Crowell, *Phys. Rev. B* **67**, 020403 (2003).

[5] G. de Loubens, A. Riegler, B. Pigeau, F. Lochner, F. Boust, K. Y. Guslienko, H. Hurdequint, L. W. Molenkamp, G. Schmidt, A. N. Slavin, V. S. Tiberkevich, N. Vukadinovic, O. Klein, *Phys. Rev. Lett.* **102**, 177602 (2009).

[6] K. S. Buchanan, P. E. Roy, M. Grimsditch, F. Y. Fradin, K. Y. Guslienko, S. D. Bader, V. Novosad, *Nat. Phys.* **1**, 172 (2005).

[7] R. P. Cowburn, D. A. Allwood, G. Xiong, M. D. Cooke, *J. Appl. Phys.* **91**, 6949 (2002).

[8] R. Engel-Herbert, T. Hesjedal, D. M. Schaadt, *J. Appl. Phys.* **101**, 09K103 (2007).

[9] M. Hehn, K. Ounadjela, J.-P. Bucher, F. Rousseaux, D. Decanini, B. Bartenlian, C. Chappert, *Science* **272**, 1782 (1996).

[10] F. Cheynis, A. Masseboeuf, O. Fruchart, N. Rougemalle, J. C. Toussaint, R. Belkhou, P. Bayle-Guillemaud, A. Marty, *Phys. Rev. Lett.* **102**, 107201 (2009).

[11] V. Vukadinovic, F. Boust, *Phys. Rev. B* **75**, 014420 (2007).

[12] M. Yan, R. Hertel, C. M. Schneider, *Phys. Rev. B* **76**, 094407 (2007).

[13] C. A. Ross, M. Hwang, M. Shima, J. Y. Cheng, M. Farhoud, T. A. Savas, H. I. Smith, W. Schwarzacher, F. M. Ross, M. Redjdal, F. B. Humphrey, *Phys. Rev. B* **65**, 144417 (2002).

[14] A. Knittel, M. Franchin, T. Fischbacher, F. Nasirpouri, S. J. Bending, H. Fangohr, *New J. Phys* **12**, 113048 (2011).

[15] A. A. Zhukov, A. V. Goncharov, P. A. J. de Groot, M. A. Ghanem, P. N. Bartlett, R. Boardman, H. Fangohr, V. Novosad, G. Karapetrov, *J. Appl. Phys.* **97**, 10J701 (2005).

[16] R. Hertel, O. Fruchart, S. Cherifi, P.-O. Jubert, S. Heun, A. Locatelli, J. Kirschner, *Phys. Rev. B* **72**, 214409 (2005).

[17] J. D. Adam, L. E. Davis, G. F. Dionne, E. F. Schloemann, S. N. Stitzer, *IEEE Trans. Microw. Theory Tech.* **5**, 721 (2002).

[18] W. S. Ishak, K. W. Chang, *IEEE Trans. Microw. Theory Tech.* **34**, 1383 (1986).

[19] A. A. Serga, A. V. Chumak, B. Hillebrands, *J. Phys. D: Appl. Phys.* **43**, 264002 (2010).

[20] G. E. W. Bauer, E. Saitoh, B. J. van Wees, *Nature Mater.* **11**, 391 (2012).

[21] Z. Wang, Y. Sun, M. Wu, V. Tiberkevich, A. Slavin, *Phys. Rev. Lett.* **107**, 146602 (2011).

[22] T. Schneider, A. A. Serga, B. Leven, B. Hillebrands, R. L. Stamps, M. P. Kostylev, *Appl. Phys. Lett.* **92**, 022505 (2008).

[23] Y. Kajiwara, K. Harii, S. Takahashi, J. Ohe, K. Uchida, M. Mizuguchi, H. Umezawa, H. Kawai, K. Ando, K. Takanashi, S. Maekawa, E. Saitoh, *Nature* **464**, 262 (2010).

[24] C. Burrowes, B. Heinrich, B. Kardasz, E. A. Montoya, E. Girt, Y. Sun, Y.-Y. Song, M. Wu, *Appl. Phys. Lett.* **100**, 092403 (2012).

[25] S. L. Vysotskii, S. A. Nikitov, Y. A. Filimonov, *JETP* **101**, 547 (2005).

[26] A. V. Chumak, A. A. Serga, S. Wolff, B. Hillebrands, M. P. Kostylev, *Appl. Phys. Lett.* **94**, 172511 (2009).

[27] L. Trifunovic, F. L. Pedrocci, D. Loss, *http://arxiv.org/pdf/1305.2451v1.pdf* (2013).

[28] A. Hubert, R. Schafer, *Magnetic Domains: The Analysis of Magnetic Microstructures* (Springer, Berlin, 1998).

[29] R. L. Compton, T. Y. Chen, P. A. Crowell, *Phys. Rev. B* **81**, 144412 (2010).

[30] G. N. Kakazei, M. Ilyn, O. Chubykalo-Fesenko, J. Gonzalez, A. A. Serga, A. V. Chumak, P. A. Beck, B. Laegel, B. Hillebrands, K. Y. Guslienko, *Appl. Phys. Lett.* **99**, 052512 (2011).

[31] J. A. J. Burgess, A. E. Fraser, F. F. Sani, D. Vick, B. D. Hauer, J. P. Davis, M. R. Freeman, *Science* **339**, 1051 (2013).

[32] A. V. Chumak, A. A. Serga, B. Hillebrands, M. P. Kostylev, *Appl. Phys. Lett.* **93**, 022508 (2008).

[33] J. Callaway, R. Boyd, *Phys. Rev.* **134**, A1655 (1964).

[34] K.-S. Lee, D.-S. Han, S.-K. Kim, *Phys. Rev. Lett.* **102**, 127202 (2009).

[35] S. E. C. Corporation, Shin etsu chemical corporation lot number sew-3571.

[36] A. E. Fraser, Focus ion beam milled magnetic cantilevers, Master's thesis, University of Alberta (2010).

[37] O. V. Sukhostavets, B. Pigeau, S. Sangiao, G. de Loubens, V. V. Naletov, O. Klein, K. Mitsuzuka, S. Andrieu, F. Montaigne, K. Y. Guslienko, *Accepted: Phys. Rev. Lett* (2013).

[38] Mumax2 gpu micromagnetics - http://code.google.com/p/mumax2/.

[39] Micromagnum gpu micromagnetics - http://micromagnum.informatik.uni-hamburg.de/.

[40] Llg micromagnetics (ver. 2.56d online: http://llgmicro.home.mindspring.com).

[41] S. Wintz, C. Bunce, A. Neudert, M. Körner, T. Strache, M. Buhl, A. Erbe, S. Gemming, J. Raabe, C. Quitmann, J. Fassbender, *Phys. Rev. Lett.* **110**, 177201 (2013).

CHAPTER 6

Nanomechanical AC Susceptometry of an Individual Mesoscopic Ferrimagnet

The material presented in this chapter by J.E. Losby, Z. Diao, F. Fani Sani, D. T. Grandmont, M. Belov, J. A. J. Burgess, W. K. Hiebert, and M. R. Freeman has been accepted for publication in Solid State Communications (Special Issue—Spin Mechanics) (2013).

Abstract

A novel method for simultaneous detection of both DC and time-dependent magnetic signatures in individual mesoscopic structures has emerged from early studies in spin mechanics. Multifrequency nanomechanical detection of AC susceptibility and its harmonics highlights reversible nonlinearities in the magnetization response of a single yttrium iron garnet (YIG) element, separating them from hysteretic jumps in the DC magnetization.

6.1 Introduction

Nanomechanical torque magnetometry of quasi-static magnetization processes has sparked recent interest due to its exceptional sensitivity (with room-temperature magnetic moment resolution approaching $10^6\mu_B$) and ability to non-invasively measure single, mesoscopic elements [1, 2, 3]. The study of individual structures is a necessity to probe local effects from variation in the magnetic microstructure due to grain boundaries, vacancies, and other intrinsic or extrinsic inhomogeneities. These are masked in measurements of arrays of magnetic structures but can have a tremendous impact on the magnetization response of single elements. In this technique a magnetostatic torque, $\boldsymbol{\tau}$, is exerted on the magnetization, $\boldsymbol{M}$, by an external field, $\boldsymbol{H}$: $\boldsymbol{\tau} = \boldsymbol{M}V \times \mu_0\boldsymbol{H}$, in which V is the sample volume. If the magnetic material is affixed to a torsional resonator, the induced magnetic torque is converted to a mechanical deflection proportional to its magnetization. For structures with strong in-plane magnetic anisotropy, a small torquing AC (dither) field is applied out-of-plane to the surface while a DC field biases the in-plane magnetization. By ramping the DC field, the quasi-static magnetization evolution with applied field can be recorded.

Techniques to probe time-dependent magnetic phenomena yield information complementary to the DC magnetization. In particular, the AC magnetic response aids in discriminating reversible from irreversible magnetization changes. In the small signal regime, an AC magnetization $\boldsymbol{M}^{\mathrm{AC}} = \boldsymbol{\chi}\boldsymbol{H}^{\mathrm{AC}}$ is induced by an alternating field, where $\boldsymbol{\chi}$ is a susceptibility tensor. In bulk magnetic systems, low frequency susceptibility (including the use of higher order susceptibility [4, 5]) measurements are used extensively to monitor myriad phenomena from the onset of ferromagnetism at the Curie temperature [6, 7], magnetization reversal processes in thin films [8, 9] and patterned nanostructures [10], exchange anisotropy in exchange biased systems [11], and dynamics in spin-glass systems [12]. The advantages offered by nanomechanical transduction have yet to be fully exploited for magnetic susceptibility measurements. It is highly

desirable to develop an experimental technique for measuring both DC and AC components of magnetization, complementary to SQUID measurements [13, 14] by virtue of operating in a wider range of sample environments. Micro Hall magnetometers can also be very sensitive [15, 16], but their low bandwidth will limit applicability to susceptibility measurements. Synchrotron-based XMCD-PEEM has also been utilized to record low-frequency dynamic susceptibility in magnetic thin-films [17, 18].

Here we report a nanomechanical platform for simultaneous DC and AC magnetic measurements through the introduction of an AC field component along the bias field direction, to probe the quasi-static longitudinal susceptibility. Two orthogonal AC fields, if applied at different frequencies simultaneously, give rise to AC magnetic torques at the sum and difference frequencies. These can be tuned to match the natural resonance frequency of the resonator, allowing it to function effectively as a signal mixer. Different frequency components can be extracted from the mechanical signal as the DC field sweeps the magnetization texture to measure simultaneously the DC magnetization, AC susceptibility, and higher order AC susceptibility terms.

6.2 Nanomechanical AC Susceptometry through Frequency Mixing

Determination of the susceptibility requires some level of description of the spin-mechanical coupling, taking in to account the conversion of magnetic torque into mechanical torque. The full tensor analysis will include Einstein-de Haas terms, which we will neglect here to concentrate on the net mechanical torque arising through magnetic anisotropy. Conceptually, we can view the system as two torsion springs connected in series. The geometrically-confined magnetization texture of the disk is the first spring, as is the one acted on directly by the torquing fields. In turn, the net magnetic torque will twist the torsion rod until an equivalent mechanical counter-torque develops. For the

present analysis, we define the effective magnetic torsion spring constants by converting magnetic susceptibilities into angular changes as if the magnetization of the element were a single macrospin. Although far from the real case, the parallel axis theorem allows for the same net torque from the same net magnetization independent of how the magnetization is distributed.

The net magnetic anisotropy (shape plus magnetocrystalline) of the mesoscale magnetization in this simple picture manifests itself through differences in diagonal components of the magnetic susceptibility tensor. If no anisotropy exists, then the equilibrium magnetization will always be parallel to the applied field, with a resultant torque of zero. In general, one will encounter structures with significantly different susceptibilities parallel and perpendicular to the plane of the torsion paddle, but where neither component is negligible. This is the case for the specific example we consider below, a 3D vortex state in a short cylinder of YIG, where the low-field linear in-plane susceptibility is approximately twice the out-of-plane susceptibility [19]. Then, the resultant torque in simultaneous small (for linear magnetization response) fields H_x and H_z is:

$$-\tau_y = \mu_0(M_x H_z - M_z H_x)V = \mu_0(\chi_x - \chi_z)H_x H_z V \tag{6.1}$$

This net torque will transfer to the lattice and twist the resonator. For a low frequency AC field, an AC torque ensues in phase with the field. If the frequency is not too high, the magnetization remains in quasi-static equilibrium with the field at all times. For the vortex structure in the absence of pinning (no slow thermal dynamics), this criterion is satisfied at frequencies in the low MHz regime, convenient for resonant enhancement of the mechanical response in nanoscale torsional structures. In the present experiment, corrections for the applied field angles changing in the frame of reference of the paddle are negligible: the mechanical spring is much stiffer ($\sim 10^6\times$) than the magnetic spring, and the mechanical Q is only 2600.

When two, orthogonal AC fields act simultaneously at different frequencies, f_1 and f_2, AC magnetic torques at the sum and difference frequencies also arise,

according to:

$$\begin{aligned} -\tau_y &= \mu_0(\chi_x - \chi_z) H_x^{ac} \cos(2\pi f_1 t) H_z^{ac} \cos(2\pi f_2 t) V \\ &= \mu_0(\chi_x - \chi_z) \frac{H_x^{ac} H_z^{ac}}{2} (cos(2\pi(f_2 - f_1)t) + cos(2\pi(f_2 + f_1)t)) V \end{aligned} \tag{6.2}$$

With the simultaneous application of a DC field to sweep the magnetization texture through a hysteresis cycle, this becomes the basis of the AC susceptometry measurement, to complement the DC magnetization data.

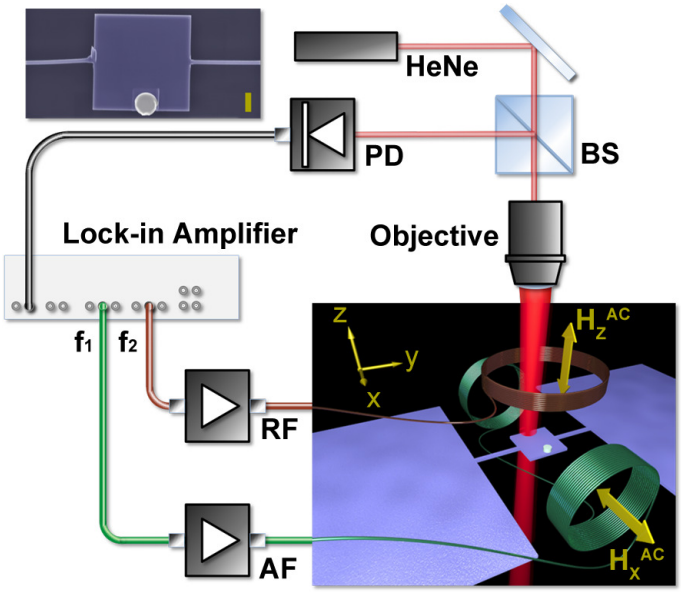

Figure 6.1: Instrument schematic for frequency-mixed nanomechanical detection of AC susceptibility. The lock-in amplifier provides the reference/drive frequencies, f_1 and f_2, which induce orthogonal AC fields through a Helmholtz coil assembly (H_x^{ac}) and single coil (H_z^{ac}), both illustrated in the bottom-right inset). The lock-in output signal is amplified by audio (AF) and radio (RF) frequency power amplifiers, respectively. A HeNe laser is used to interferometrically detect the mechanical motion of the torsional resonator (BS=beam splitter, PD=photodetector). The difference and/or sum frequencies are demodulated simultaneously at the lock-in. Top left inset: false-colour scanning electron micrograph of the device (scale bar = 1 μm)

6.3 Experiment

For demonstration of the technique, a single-crystal, mesoscale YIG disk (radius = 600 nm, thickness = 500 nm) was focused ion beam (FIB)-milled from an epitaxial thick film and nanomanipulated *in-situ* onto a prefabricated torsional resonator [3]. A scanning electron micrograph of the completed device is shown in the inset of Fig 6.1. The FIB milling and 'pick and place' procedures were employed to overcome the difficulty of forming monocrystalline mesoscale objects which are to be measured singularly. The pristine magnetic nature of the YIG disk is exhibited, within experimental resolution, by the lack of Barkhausen signatures in the change of the magnetization with applied field, which are associated with nanoscale imperfections such as grain boundaries in polycrystalline materials. In the present context YIG simplifies interpretation of the demonstration susceptibility signals. Hysteretic minor loops associated with Barkhausen transitions in the magnetization evolution [2], can strongly influence and complicate the AC susceptibility. The YIG disk, on the other hand, was shown to have no observable minor hysteresis.

The resonator was driven by the magnetic torque exerted on the YIG disk. The mechanical deflection was optically detected through the interferometric modulation of the light reflected from the device. The magnetization was biased by a variable external field, (H_x^{dc}, Cartesian coordinates indicated in Fig. 6.1) in the plane of the resonator and perpendicular to the torsion rod. The AC torquing field was supplied by a small copper wire coil which produced an out-of-plane dither field, H_z^{ac}, to complete the field orientations necessary for the torque magnetometry measurement. The AC field was driven at the fundamental torsion frequency to maximize detection sensitivity. The magnetization of the YIG disk with applied bias field is shown in Fig. 6.2, characterized by a unipolar hysteresis similar to what has been observed in two-dimensional disks where the sharp transitions are attributed to the nucleation and annihilation of a magnetic vortex. However, the thickness of the YIG disk promotes additional three dimensional structure in the magnetization texture (detailed

in Ref. 19).

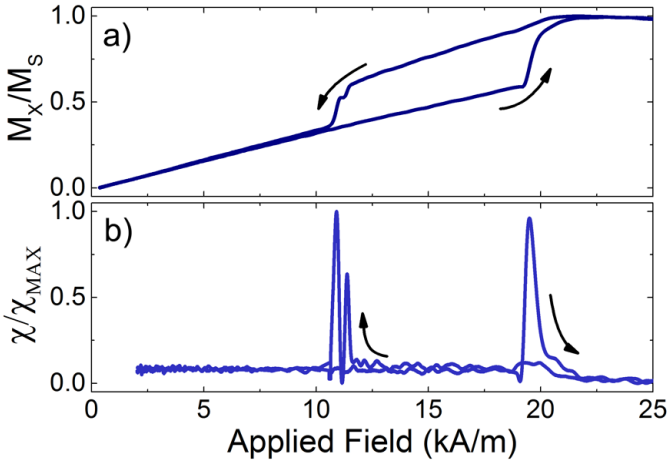

Figure 6.2: DC torque magnetometry of an individual micromagnetic YIG disk, (a) and the corresponding numerical derivative, (b).

A result from the simultaneous acquisition of the DC magnetization and AC susceptibility is shown in Fig 6.3. Features agreeing closely to the numerical derivative of the DC magnetization curve, Fig. 6.2b, are evident with the differences arising from the susceptibility screening out irreversible events in the field sweep. Here, the lock-in amplifier provided both orthogonal ac drive frequencies, f_1 (H_x^{ac}) and f_2 (H_z^{ac}), while recording the response of the resonator through simultaneous demodulation [20] at f_2 and at $f_2 - f_1$ (see Fig. 6.1 for measurement scheme). It is interesting to note that a softening of the magnetization texture (peak in the susceptibility) occurs just after the irreversible annihilation transition on the field sweep-up. The highest field susceptibility is at opposite phase in this measurement consistent with the possibility inherent in Eqn. 6.2 for χ_z contributes to exceed the χ_x contribution as the magnetization approaches saturation in x. This feature is replicated again on the sweep down at a slightly lower field – a hysteretic feature not readily apparent from the DC magnetization.

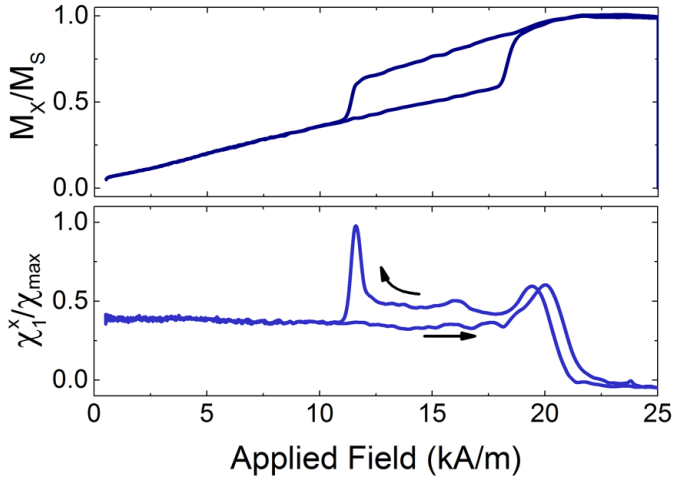

Figure 6.3: Simultaneous acquisition of the DC magnetometry through the driven signal at f_2=f_{res}+f_1, a), and low frequency AC susceptibility detected at the mixing (resonance) frequency, f_{res}, b). Here, f_1 was set to 500 Hz.

6.4 Harmonics of the AC Susceptibility

The technique can easily be extended to detect the harmonics of AC susceptibility arising when the magnetization response is nonlinear in field. For example, for a magnetization describable by a polynomial series in field,

$$M_x = a_1 H_x + a_2 H_x^2 + a_3 H_x^3 + a_4 H_x^4 + a_5 H_x^5 + a_6 H_x^6 + \ldots, \tag{6.3}$$

where $H_x = H_x^{dc} + H_x^{ac}$, multiple harmonics of f_1 arise and also mix with f_2 to generate unique torque terms. For this representation of nonlinear magnetization, Table **??** shows the amplitude coefficients for the first six entries in the Fourier sum for the full nonlinear susceptibility,

$$\chi_x(H_x) = \sum_{n=-\infty}^{\infty} \chi_n^x(H_x) e^{-i(2\pi n f_1)t}. \tag{6.4}$$

A spectroscopic frequency-versus-field mapping of the higher order AC suscep-

Table 6.1: Harmonics of the AC susceptibility

$f_2 \pm nf_1$	Amplitude coefficients	related to
$f_2 + 0$	$a_1 H_x^{dc} + a_2[(H_x^{dc})^2 + \frac{1}{2}] + a_3[(H_x^{dc})^3 + \frac{3}{2}H_x^{dc}]$ $+a_4[(H_x^{dc})^4 + 3H_x^{dc})^2 + \frac{3}{8}] + a_5[(H_x^{dc})^5 + 5(H_x^{dc})^3 + \frac{15}{8}H_x^{dc}]$ $+a_6[(H_x^{dc})^6 + \frac{15}{2}(H_x^{dc})^4 + \frac{45}{8}(H_x^{dc})^2 + \frac{5}{16}]$	$\chi_0^x(H_x)$
$f_2 \pm f_1$	$a_1 + 2a_2 H_x^{dc} + a_3[3(H_x^{dc})^2 + \frac{3}{4}] + a_4[4(H_x^{dc})^3 + 3H_x^{dc}]$ $+a_5[5(H_x^{dc})^4 + \frac{15}{2}(H_x^{dc})^2 + \frac{5}{8}]$ $+a_6[6(H_x^{dc})^5 + 15(H_x^{dc})^3 + \frac{15}{4}H_x^{dc}] - \frac{dM_z}{dH_z}\|_{H_x^{dc}}$	$\chi_1^x(H_x)$
$f_2 \pm 2f_1$	$\frac{1}{2}a_2 + \frac{3}{2}a_3 H_x^{dc} + a_4[3(H_x^{dc})^2 + \frac{1}{2}] + a_5[5(H_x^{dc})^3 + \frac{5}{2}H_x^{dc}]$ $+a_6[\frac{15}{2}(H_x^{dc})^4 + \frac{15}{2}(H_x^{dc})^2 + \frac{15}{32}]$	$\chi_2^x(H_x)$
$f_2 \pm 3f_1$	$\frac{1}{4}a_3 + a_4 H_x^{dc} + a_5[\frac{5}{2}(H_x^{dc})^2 + \frac{5}{16}] + a_6[5(H_x^{dc})^3 + \frac{15}{8}H_x^{dc}]$	$\chi_3^x(H_x)$
$f_2 \pm 4f_1$	$\frac{1}{8}a_4 + \frac{5}{8}a_5 H_x^{dc} + a_6[\frac{15}{8}(H_x^{dc})^2 + \frac{3}{16}]$	$\chi_4^x(H_x)$
$f_2 \pm 5f_1$	$\frac{1}{16}a_5 + \frac{3}{8}a_6 H_x^{dc}$	$\chi_5^x(H_x)$
$f_2 \pm 6f_1$	$\frac{1}{32}a_6$	$\chi_6^x(H_x)$

tibilities for the YIG disk is shown in Fig. 6.4 for the sweep-down portion of the hysteresis cycle (31 to 4 kA/m). Here the frequency response was recorded at each magnetic field step while keeping both f_1 (H_x^{ac}) and f_2 (H_z^{ac}) constant (500 Hz and 1.8095 MHz, respectively). The f_2 drive was shifted from the resonance frequency (1.808 MHz) in order to allow for more susceptibility harmonics to be recorded within the mechanical resonance line-width. The brightest band is the demodulation of the f_2 drive, while the subsequent bands represent the harmonics of the magnetic susceptibility. The features observed in the second half of the field sweep in Fig. 6.3b are reproduced, including the strong susceptibility peak just before (very close to the onset of) the nucleation transition. Through such strong nonlinearities in the magnetization curve, mixing frequencies $f_2 \pm nf_1$ are observed up to $n = 7$ in Fig. 6.4.

The multifrequency responses are all harmonics of the low AC frequency dithering the magnetization, mixed to fall within the mechanical resonance linewidth. High harmonics of susceptibility have been used previously to characterize hysteresis for bulk ferromagnetism and superconductivity. In bulk systems, and in arrays of nanostructures, the strongest nonlinearities in magnetization come from hysteretic features. Typical AC field amplitudes can

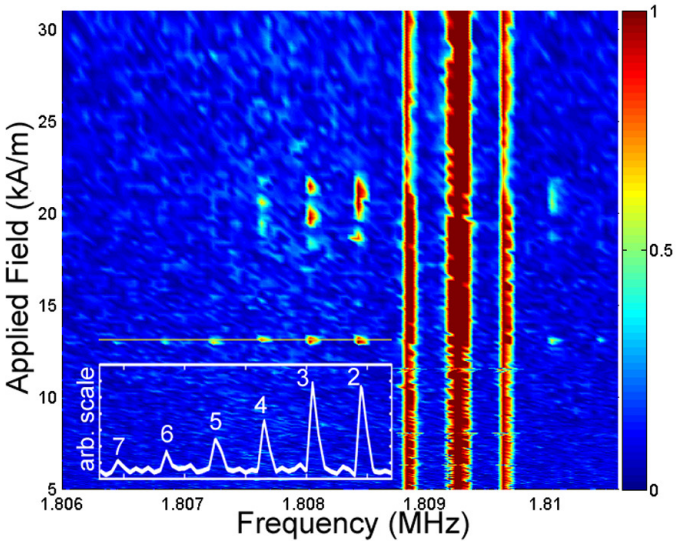

Figure 6.4: Spectroscopic mapping of higher harmonics of the AC susceptibility. f_1 (H_x^{ac}) and f_2 (H_z^{ac}) were each driven simultaneously at constant frequency (500 Hz and 1.8095 MHz respectively) while the frequency response (100 Hz bandwidth) was measured with magnetic field. The image shows the sweep-down portion of the field sweep. The band of highest intensity is the demodulation of f_2, with the successive bands representing the harmonics of AC susceptibility, $f_2 \pm n f_1$. A line-scan thorough the high susceptibility peaks is shown in the bottom left, showing up to the n=7 harmonic. The original intensity scale was cropped to show the highest order signals.

probe minor hysteresis loops [21], or even the full hysteresis close enough to the Curie temperature [4]. By contrast, the single mesoscale structure we examine here exhibits no minor hysteresis, and its magnetization nonlinearities are observed without any diminution from array averaging. The harmonics characterize the non-hysteretic, nonlinear response.

6.5 Conclusion

In summary, nanomechanical detection of the low-frequency AC susceptibility (along with higher order harmonics) of an individual micromagnetic disk was accomplished through frequency mixing of orthogonal AC driving fields manifesting as a mechanical torque on the resonator. In addition to providing further insight into quasi-static magnetization processes in geometrically-confined magnetic elements, this signal-mixing approach, in principle, will enable very broadband measurements of frequency-dependent susceptibility.

Bibliography

[1] J. Moreland, A. Jander, J. A. Beall, P. Kabos, S. E. Russek, *IEEE T. Magn.* **37**, 2770 (2001).

[2] J. A. J. Burgess, A. E. Fraser, F. F. Sani, D. Vick, B. D. Hauer, J. P. Davis, M. R. Freeman, *Science* **339**, 1051 (2013).

[3] J. Losby, J. A. J. Burgess, Z. Diao, D. C. Fortin, W. K. Hiebert, M. R. Freeman, *J. Appl. Phys.* **111**, 07D305 (2012).

[4] C. Rüdt, P. J. Jensen, A. Scherz, J. Linder, P. Poulopoulos, K. Baberschke, *Phys. Rev. B* **69**, 014419 (2004).

[5] S. Prüfer, M. Ziese, *Phys. Stat. Sol.* **245**, 1661 (2008).

[6] B. Heinrich, A. S. Arrott, *J. Appl. Phys.* **64**, 1991 (1982).

[7] H. R. Sydney, D. H. Chaplin, G. V. H. Wilsin, *J. Magn. Magn. Mater.* **2**, 345 (1976).

[8] W. Kleemann, J. Rhensius, O. Petracic, J. Ferré, J. P. Jamet, H. Bernas, *Phys. Rev. Lett.* **99**, 097203 (2007).

[9] U. Stetter, M. Farle, K. Baberschke, W. G. Clark, *Phys. Rev. B* **45**, 503 (1992).

[10] J. A. J. Burgess, D. C. Fortin, J. E. Losby, D. Grombacher, J. P. Davis, M. R. Freeman, *Phys. Rev. B* **82**, 144403 (2010).

[11] V. Ström, B. J. Jönsson, K. V. Rao, D. Dahlberg, *J. Appl. Phys.* **81**, 5003 (1997).

[12] L. Lundgren, P. Svedlindh, O. Beckman, *J. Magn. Magn. Mater.* **25**, 33 (1981).

[13] M. J. Martínez-Pérez, J. Sesé, F. Luis, D. Drung, T. Schurig, *Rev. Sci. Instrum.* **81**, 016108 (2010).

[14] W. Wernsdorfer, B. Doudin, D. Mailly, K. Hasselbach, A. Benoit, J. Meier, J.-P. Ansermet, B. Barbara, *Phys. Rev. Lett.* **77**, 1873 (1996).

[15] K. S. Novoselov, A. K. Geim, S. V. Dubonos, E. W. Hill, I. V. Grigorieva, *Nature* **426**, 812 (2003).

[16] S. Wirth, S. von Molnár, M. Field, D. D. Awschalom, *J. Appl. Phys.* **85**, 5249 (1999).

[17] A. Aspelmeier, M. Tischer, M. Farle, M. Russo, K. Baberschke, D. Arvanitis, *J. Magn. Magn. Mater.* **146**, 256 (1995).

[18] F. M. Römer, F. Kronast, L. Heyne, C. Hassel, A. Banholzer, M. Kläui, R. Meckenstock, J. Linder, M. Farle, *Appl. Phys. Lett.* **96**, 122501 (2010).

[19] J. E. Losby, Z. Diao, D. T. Grandmont, F. F. Sani, J. A. J. Burgess, L. C. Parsons, T. Firdous, W. K. Hiebert, D. Vick, M. R. Freeman, *(In preparation)* (2013).

[20] Zurich instruments hf2li with multi-frequency (mf) option, http://www.zhinst.com.

[21] C. P. Bean, *Rev. Mod. Phys.* **36**, 31 (1964).

CHAPTER 7

Concluding Remarks

7.1 Conclusion

In this Thesis, highly-sensitive nanomechanical torque magnetometry techniques for the characterization of single, nanoscale magnets were developed. Early work was focused on the probing of the magnetostatic evolution of the sample magnetization with an applied field, which continues to yield rich information and allows for a quantitative comparison to micromagnetic simulation. Recently, a frequency-mixing technique has been devised to allow for the nanomechanical detection of low-field AC susceptibility which, when scaled to the appropriate frequency-regime, is the fundamental probe for magnetization dynamics.

In Chapter 1, the historical and theoretical background encompassing nanomechanics, micromagnetism, and nanomechanical torque magnetometry were introduced. The experimental setup, mechanical transduction scheme, and nanofabrication methods are outlined in Chapter 2.

For the material presented in Chapter 3, an early prototypical magnetic cantilever (magnetic through its volume) was fabricated and magnetization switching was mechanically observed as an external field was swept. A simple finite-element model that treats the switching process as a domain wall propagating

across the cantilever length was established and used to transform the output of micromagnetic simulation results to a mechanical deflection of the cantilever, yielding similar results.

In Chapter 4, the thermomechanical noise measured in a nanotorsional magnetometer was used to calibrate the displacement and magnetic moment sensitivity of the device. The room-temperature, off-resonant displacement sensitivity was found to be 75 fm/Hz$^{1/2}$ and the magnetic moment sensitivity was shown to be on the order of $10^6\mu_B$, which is an order of magnitude better than previously reported torque magnetometers.

Chapter 5 presented the characterization of the three-dimensional magnetization in a mesoscale, single-crystal YIG disk. In order to overcome fabrication obstacles for creating localized, geometrically confined structures through traditional lithography-based fabrication methods, the focused ion beam was employed to mill the disk from a bulk single crystal, which was then micromanipulated onto a mechanical resonator. A vector magnetometry method was developed to probe both the in- and out-of-plane components (with respect to the resonator plane) of magnetization in the disk, yielding results similar to micromagnetic simulation.

The nanomechanical detection of low-frequency AC susceptibility and its higher order harmonics was achieved using a frequency-mixing technique, and was proposed in Chapter 6. This technique involves the application of two orthogonally arranged AC magnetic fields which are driven such that their sum or difference signals match the resonance frequency of the resonator, in essence utilizing the device as a RF mixer to mechanically detect the mixed signal, and which yields both magnetization and susceptibility information. The method was demonstrated using a YIG disk affixed to a torque resonator. Both the magnetization and low-frequency AC susceptibility were simultaneously acquired, as were the higher order susceptibility harmonics. The latter results highlight reversible nonlinearities that clearly deviate from hysteretic jumps in the magnetization.

It is the hope of the author that the techniques reported here help open the

door to further investigations of magnetostatic and dynamic phenomena as the sensitivities of nanomechanical resonators are further increased using new transduction methods. The torque magnetometer, although somewhat overlooked through previous years for use in the investigation of micromagnets, will be a valuable tool in the emerging field of "spin mechanics", which involves the coupling of the spin and mechanical degrees of freedom.

7.2 Outlooks for the Future

7.2.1 Future Magnetostatic-based Measurements

There are many possibilities to explore in terms of magnetostatics. Recent investigations have been done to quantitatively map magnetic energy landscapes and energy barriers caused by FIB-induced pinning sites using the vortex core [1]. With higher sensitivity mechanical readout methods, it should be possible to probe intrinsic pinning sites with smaller barriers, down to the Peierl's potential of the atomic lattice [2]. Another area of exploration is that of other types of magnetic systems. So far, mainly soft ferromagnetic materials have been studied using nanomechanical magnetometry. There is also interest to study other thin-film based systems, which could easily be amenable to fabrication techniques developed herein. One example is the ferromagnetic-antiferromagnetic (FM-AFM) layered system, which exhibit exchange bias effects in its hysteresis and Néel transitions that could be mechanically measured. The technique can be extended to also sensitively measure the pinning and transitions exhibited in superconducting materials.

7.2.2 Detection of Dynamical Magnetization

Magnetic Vortex Gyrotropic Mode

The magnetic vortex configuration, representing the lowest-energy state in thin circular disks with radii on the order of a few micrometers and below, has gained considerable interest in recent years. The system consists of a small, out-of-plane, high-energy density core in the center of an in-plane, flux-enclosed, circular magnetization configuration following the disk perimeter. This stable state exhibits a two-fold degeneracy in terms of the vortex polarity (in- or out-of-plane) and chirality (clockwise or counter-clockwise in-plane circulation), which could have promising application as memory storage elements.

A unique dynamical mode in these systems occurs when the vortex is displaced from equilibrium (for example, by a field pulse) and then oscillates in a circular pattern, called the gyrotropic mode. These modes occur approximately in the frequency range of hundreds of MHz, depending on the disk radius and thickness [3, 4], and should be accessible with the aforementioned nanomechanical transduction improvements, possibly in conjunction with the frequency-mixing technique described in Chapter 6. Another exciting possibility is the mechanical observation of the dynamic switching of the vortex core polarity with a large enough excitation amplitude [5]. It would also be interesting to investigate pinning effects dynamically, for example through sites along the core gyration path.

Domain Wall Motion, Pinning, and Resonance

The recent introduction of a domain wall-based logic and memory architecture has gained significant interest [6]. The nature of domain wall motion and their pinning in mesoscopic magnetic wires are not well understood, but could affect the performance of these devices significantly. There have been significant efforts in detecting and modelling [7, 8, 9] domain wall motion in wires, as well

as their interactions with pinning sites, both geometric [10, 11, 12] and FIB-induced [13, 14]. The pinned domain walls also exhibit resonances ([15, 16]) that could possibly affect the dynamical behaviours of the system. Their frequencies have also been shown to be tuneable through the modification of the pinning sites [17], to the tens of MHz. Nanomechanical studies on domain wall pinning in micro- or nanowires have yet to be done, but preliminary work has been conducted. Magnetic cantilevers with geometric pinning sites have been fabricated in order to pin transverse domain walls propagating along the beam length and preliminary results will be discussed in the Appendix A. The investigation of dynamical behaviour of domain walls in thin wires should be feasible using nanomechanical transduction.

7.2.3 Magneto-mechanical Coupling

Perhaps the ultimate goal in spin-mechanics is the pure coupling between the magnetic and mechanical subsystems, where a coherent exchange of energy can occur. In essence, this is the resonant Einstein-de Haas or Barnett Effect. Magneto-mechanical coupling in nanomechanical systems has been proposed [18, 19, 20], but obstacles to achieving it still remain. A main criteria is a system where there exists a crossing of the mechanical and ferromagnetic resonance frequencies, where the latter are still significantly higher than the GHz-range mechanical devices to-date [21]. If achieved, this would pave the way for mechanically assisted magnetization reversal, or vice-vice versa.

7.2.4 Transition to Cavity Optomechanical Systems

Although the nanomechanical transduction methods used throughout this Thesis have achieved very high sensitivity to-date for the detection of the magnetization processes (and low-frequency differential susceptibility) in single mesoscopic magnets, an inevitable 'wall' is approaching. As devices are scaled down towards the optical diffraction limit, the Fabry-Perot-based interferometric detection scheme begins to suffer. Also, the optical finesse, a measure

of the number of photons that circulate in a cavity (where each contribute to a power/signal enhancement) is very low (essentially one). Additionally, direct laser heating of the device and/or magnet can impose a large thermal noise floor, affect the magnetization, or even lead to self-oscillations of the resonator. Another issue is compromised stability because of sample drift under the laser focus spot. All of these aspects can be nearly eliminated by transitioning from the 'traditional' free-space optical readout to optomechanical detection.

Cavity optomechanics is currently a rapidly growing field that is defined by the interaction of the mechanical motion of a resonator and light. Light exhibits a force through two mechanisms: the radiation pressure due to its angular momentum and the gradient forces that exist laterally to a propagating field. The former has been observed since Kepler's observation of comet tails pointing away from the sun [22]. Experiments have been carried out in the early 20th century to measure the momentum transfer of light to macroscopic objects [23]. In micro- and nanometer-scale systems, the radiation pressure was also observed using optical micromirrors [24], photonic crystals [25], micromechanical membranes [26], to name a few. Clever cooling methods relying on optical feedback or quantum backaction have pushed their oscillations into the quantum regime, allowing for highly-sensitive detection of displacements, very small forces, and masses [27, 28, 29]. The ability to create and investigate nonclassical states of light and motion is also enticing. The transverse gradient force, which can be very high in the near-field, has recently been exploited for use in nanomechanical transduction [30]. Since a reflective surface is generally not necessary, it has the advantage for use in planar structures, such as on-chip resonators. The method generally involves the interaction of the evanescent field of light propagating through a medium, generally a waveguide or optical resonator, with that of a nearby (usually within a few hundred nanometers) freely-standing mechanical resonator. The resonator can also be embedded into the waveguide itself, where the interaction of the gradient field occurs with the substrate. The amplitude modulation of the light can be used for both the detection and drive of the mechanical resonator.

The advantages of optomechanical transduction are many-fold over free-space interferometry techniques. When the mechanical resonators are coupled to optical resonators, the optical finesse for the detection cavity can be very high, some on the order of 1×10^4 [26]. The resonators can be relatively large (which is of importance for measuring micromagnetic elements), but still have high responsivity as the tuning of the cavity gap size is more crucial than the resonator size. Direct laser heating of the devices can also be avoided as the thermal coupling of the optical force to the mechanical resonator is very low. Because the coupling of the light to the waveguide or optical resonator are usually done using large Bragg input gratings or by bringing an optical fibre close to a micrometer scale optical resonator, stability is less of an issue than direct laser-spot measurements. A recent comparison at room-temperature has shown that devices measured through optomechanical means have sensitivities that are at least two orders of magnitude better than those measured using free-space optical methods [31].

Current efforts are being pursued to integrate nanoscale magnetic elements with optomechanical systems to create nanomechanical torque magnetometers with exquisite sensitivity and bandwidth, which will allow for both frequency and time-domain operation to detect a wide range of magnetostatic and dynamic phenomena. A couple of prototypical devices fabricated recently are shown in Fig. 7.1: a doubly-clamped mechanical resonator embedded in a waveguide holding a permalloy strip and a torsion paddle which has rods that act as a photonic waveguide with a small section along the paddle edge for magnet placement. With advancing nanofabrication techniques, many of which are tailored to optomechanical systems, there will be great flexibility in magnetometer designs. It is also likely that atomic and magnetic force microscopy techniques will take advantage of optomechanical transduction.

In addition to the transition to optomechanical readout, the current scheme used to apply the AC drive or 'dither' field must be slightly modified. The drive coils used throughout this Thesis are generally limited, mostly as a result of inductive losses, to the high-frequency (3-30 MHz) range. A conversion to

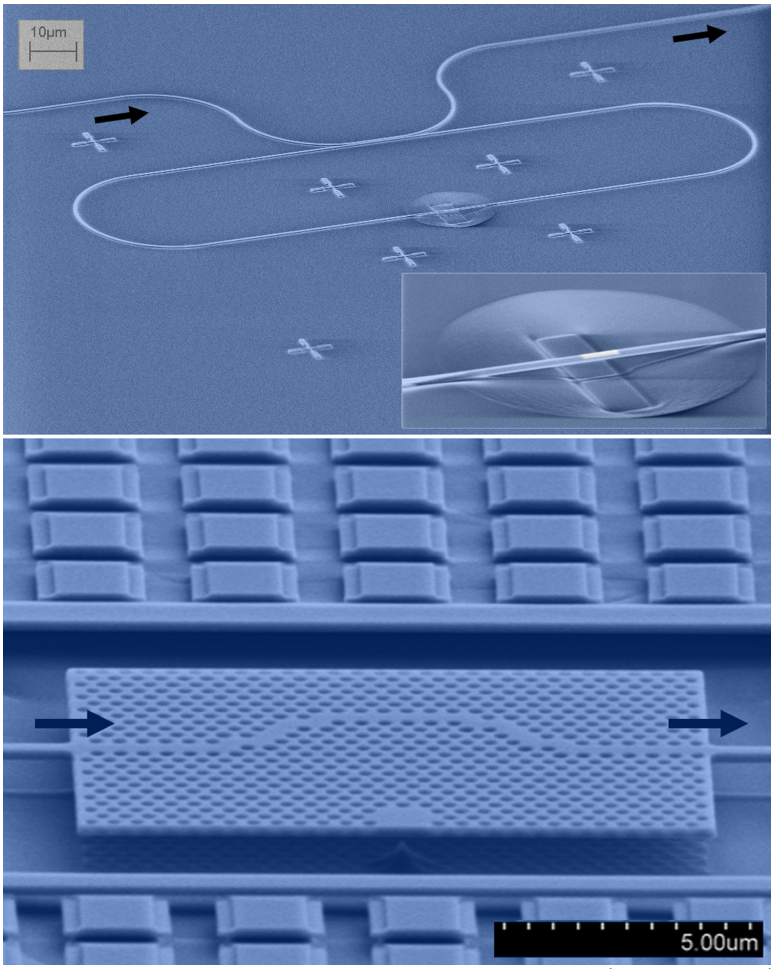

Figure 7.1: Early optomagnetomechanical devices (false colour). Top: A doubly-clamped beam (inset) embedded in a ring resonator holding a permalloy element (shown in white), which is coupled to a waveguide. Bottom: A torsional paddle with rods that also function as a waveguide. Optical input and output paths are shown as arrows.

microwave electronics and the use of broadband, impedance-matched, planar transmission lines to generate pulsed magnetic fields will allow for operation into the UHF band (up to 3 GHz). The recent introduction of digital lock-in amplification technologies (which can currently operate into the UHF band) will also assist in sensitive displacement measurement and minimize the number of instrumentation components (especially compared to traditional time-domain, pump-probe techniques) [32].

Bibliography

[1] J. A. J. Burgess, A. E. Fraser, F. F. Sani, D. Vick, B. D. Hauer, J. P. Davis, M. R. Freeman, *Science* **339**, 1051 (2013).

[2] K. S. Novoselov, A. K. Geim, S. V. Dubonos, E. W. Hill, I. V. Grigorieva, *Nature* **426**, 812 (2003).

[3] E. of vortex state excitations in magnetic submicron-size disks, *K. Yu. Guslienko and B. A. Ivanov and V. Novosad and Y. Otani and H. Shima and K. Fukamichi*, J. Appl. Phys., 2002, 91st edn. (8037).

[4] J. A. J. Burgess, J. E. Losby, M. R. Freeman, A deformable model for magnetic vortex pinning, http://arxiv.org/abs/1208.3797 (2013).

[5] B. V. Waeyenberge, A. Puzic, H. Stoll, K. W. Chou, T. Tyliszczak, R. Hertel, M. Fähnle, H. Brückl, K. Rott, G. Reiss, I. Neudecker, D. Weiss, C. H. Back, G. Schütz, *Nature* **444**, 461 (2006).

[6] S. S. P. Parkin, M. Hayashi, L. Thomas, *Science* **320**, 190 (2008).

[7] A. Yamaguchi, T. Ono, S. Nasu, K. Miyake, K. Mibu, T. Shinjo, *Phys. Rev. Lett.* **92**, 077205 (2004).

[8] T. Ono, H. Miyajima, K. Shigeto, K. Mibu, N. Hosoito, T. Shinjo, *Science* **284**, 468 (1999).

[9] A. Thiaville, Y. Nakatani, J. Miltat, Y. Suzuki, *Europhys. Lett.* **69**, 990 (2005).

[10] M. Kläui, H. Ehrke, U. Rüdiger, T. Kasama, R. E. Dunin-Borkowski, D. Backes, L. J. Heyderman, C. A. F. Vaz, J. A. C. Bland, G. Faini, E. Cambril, W. Wernsdorfer, *Appl. Phys. Lett.* **87**, 1063 (2005).

[11] E. Martinez, L. Lopez-Diaz, O. Alejos, L. Torres, C. Tristan, *Phys. Rev. Lett.* **98**, 267202 (2007).

[12] J. Akerman, M. Munoz, M. Maicas, J. L. Prieto, *Phys. Rev. B* **82**, 064426 (2010).

[13] J. H. Franken, M. Hoeijmakers, R. Lavrijsen, J. T. Kohlhepp, H. Swagten, B. Koopmans, E. van Veldhoven, D. J. Maas, *J. Appl. Phys.* **109**, 07D504 (2011).

[14] A. Vogel, S. Wintz, T. Gerhardt, L. Bocklage, T. Strache, M.-Y. Im, P. Fischer, J. Fassbender, J. Mccord, G. Meier, *Appl. Phys. Lett.* **98**, 202501 (2011).

[15] L. Thomas, M. Hayashi, X. Jiang, R. Moriya, C. Rettner, S. S. P. Parkin, *Nat. Phys.* **4**, 368 (2008).

[16] L. Bocklage, B. Krüger, P. Fischer, G. Meier, *Phys. Rev. B* **81**, 054404 (2010).

[17] S. Lepadatu, O. Wessely, A. Vanhaverbeke, R. Allenspach, A. Potenza, H. Marchetto, T. R. Charlton, S. Langridge, S. S. Dhesi, C. H. Morrows, *Phys. Rev. B* **81**, 060402(R) (2010).

[18] A. A. Kovalev, G. E. W. Bauer, A. Brataas, *Appl. Phys. Lett.* **83**, 1584 (2003).

[19] A. A. Kovalev, G. E. W. Bauer, A. Brataas, *Phys. Rev. Lett.* **94**, 167201 (2005).

[20] A. A. Kovalev, G. E. W. Bauer, A. Brataas, *Jpn. J. Appl. Phys* **45**, 3878 (2006).

[21] N. Liu, G. Giesen, M. Belov, , J. Losby, J. Moroz, A. E. Fraser, G. McKinnon, T. J. Clement, V. Sauer, W. K. Hiebert, M. R. Freeman, *Nat. Nanotechnol.* **3**, 715 (2008).

[22] J. Kepler, *De Cometis* (1619).

[23] R. A. Beth, *Phys. Rev.* **50**, 115 (1936).

[24] O. Arcizet, P. F. Cohadon, T. Briant, M. Pinard, A. Heidmann, *Nature* **444**, 71 (2006).

[25] M. Eichenfield, R. Camacho, J. Chan, K. J. Vahala, O. Painter, *Nature* **459**, 550 (2009).

[26] J. D. Thompson, B. M. Zwickl, A. M. Jayich, F. Marquardt, S. M. Girvin, J. G. E. Harris, *Nature* **452**, 72 (2007).

[27] P. F. Cohadon, A. Heidmann, M. Pinard, *Phys. Rev. Lett.* **83**, 3174 (1999).

[28] A. Naik, O. Buu, M. D. LaHaye, A. D. Armour, A. A. Clerk, M. P. Blencowe, K. C. Schwab, *Nature* **443**, 193 (2006).

[29] J. D. Teufel, T. Donner, J. W. Harlow, M. S. Allman, K. Cicak, A. J. Sirois, J. D. Whittaker, K. W. Lehnert, R. W. Simmonds, *Nature* **475**, 359 (2010).

[30] M. Li, W. H. P. Pernice, C. Xiong, T. Baehr-Jones, M. Hochberg, H. X. Tang, *Nature* **456**, 480 (2008).

[31] Z. Diao, J. E. Losby, V. T. K. Sauer, J. N. Westwood, M. R. Freeman, W. K. Hiebert, *Appl. Phys. Express* **6**, 065202 (2013).

[32] Zurich instruments hf2li with multi-frequency (mf) option, http://www.zhinst.com.

APPENDIX A

Multimodal Mechanical Magnetometry

The model presented in Chapter 3 to describe the cantilever deflection due to distributed magnetic torques along the cantilever length can be extended to higher order flexural modes. It can then be shown that, through the simultaneous measurement of multiple flexural modes, a possibility exists to determine the spatial location of a domain wall as it traverses a cantilever during magnetization reversal (along the length of the beam).

The modal shape functions, $\phi_n(x)$, for the higher order flexural modes (introduced in Eqn. 3.1) are implemented by applying the modal wavenumbers (for n=2–4, the 2nd to 4th flexural modes) $\kappa_n L$=4.694, 7.855, 10.995 and the amplitude coefficients a_n/b_n = –0.982, –1.008, –1.000 [1]. The calculation of the amplitude response at the free end for the 1st to 4th flexural modes (using Eqn. 3.3) is shown in Fig. A.1, and were rescaled relative to the first mode [2].

For the multimodal magnetometry scheme, a simultaneous acquisition of multiple flexural modes and a comparison of their relative magnitudes or amplitudes can be done simultaneously. This is shown in Fig. A.2, where the deflections (amplitude on the left and magnitude on the right) of the 2nd flexural modes are plotted with the 1st. The arrows indicate the path of the domain wall for each case, and can offer (through no observed path-crossings)

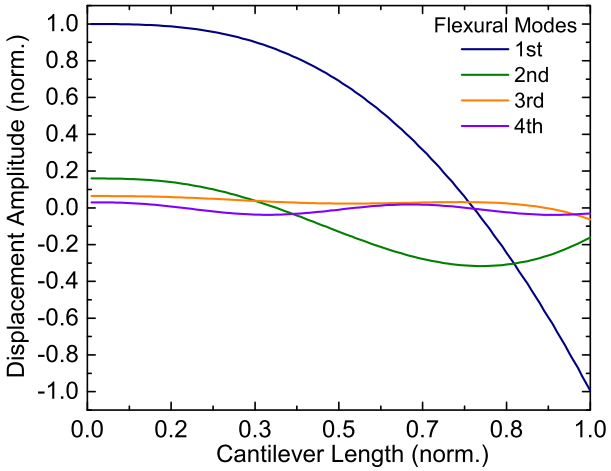

Figure A.1: The free-end deflection calculations of the first four cantilever flexural modes using the magnetic deflection model, Eqn. 3.3, as a transverse domain wall propagates along the cantilever length and changes the magnetization from $+M_X$ to $-M_X$.

positional information of the domain wall during the magnetization reversal process. Multiple magnetization configurations can lead to a similar torque behaviour on the overall cantilever response (especially when measuring a single mode). The multimodal technique offers more constraints on the possible free-end response of the cantilever, especially if more modes are simultaneously measured.

Several earlier devices were fabricated for cantilever magnetometry measurements, and are shown in Fig. A.3. The cantilevers were fabricated using SOI-based lithography and a film of permalloy was deposited afterwards across the entire wafer, covering the devices and cantilevers. Geometric pinning sites were added to some of the cantilevers to pin the domain wall for confirmation of their positions. In others, FIB-induced pinning sites (line exposures perpendicular to the cantilever length) were made in an effort to pin the magnetization. The elliptical pedestals provided the clamped end of the cantilever and also as domain wall injection pads.

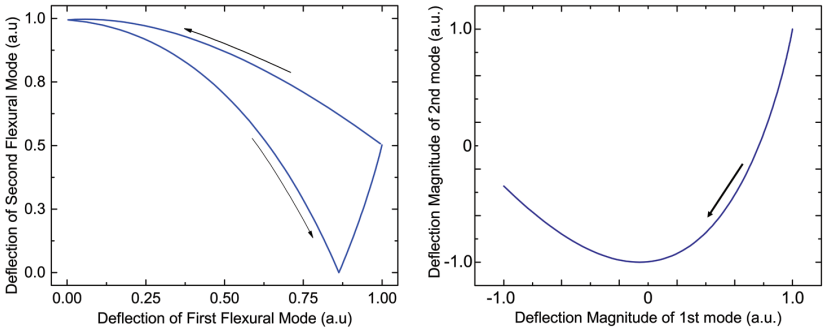

Figure A.2: Amplitude (left) and magnitude (right) components of the calculated 2nd flexural mode response plotted with the 1st mode. The arrows indicate the domain wall propagation path during magnetization reversal along the cantilever length.

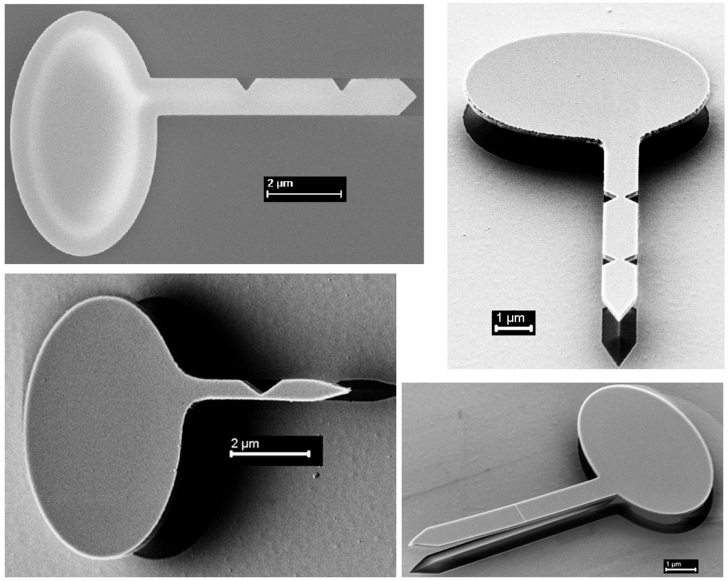

Figure A.3: Representative magnetic nanomechanical cantilevers with geometric notches for domain wall pinning. The exception (bottom right) is a focused ion beam-induced pinning site (false colour) which was done as a line exposure perpendicular to the cantilever length. The permalloy film thickness is approximately 50 to 80 nm.

The results for a single mode measurement of a cantilever is shown in Fig. A.4 , where a single notch is located 2.6 μm from the clamped end. The pinning (and subsequent depinning) of the domain wall is observed through the step-like transitions in the measured curve. The superimposed values calculated from the deflection model shows qualitative agreement with the measured data, with the interaction of the pinning site occurring at about 2.3 μm. Our current measurement scheme cannot probe the actual timescales of the switching event, and thus the magnetization appears to make a sudden jump to saturation.

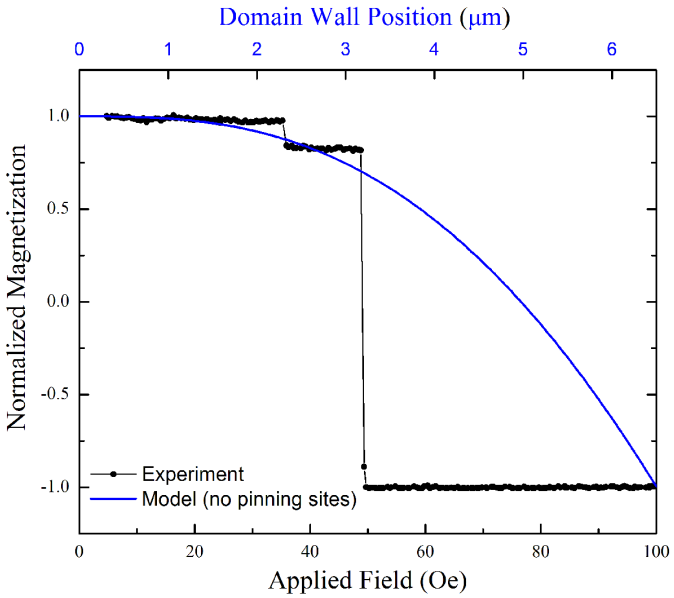

Figure A.4: Measurement (black data points) of the magnetization response ($+M_X$ to $-M_X$) in a single-notched cantilever with applied field. The blue trace is the calculated response of the cantilever using Eqn. 3.3.

The pinning of the magnetization through the focused ion beam-created sites were also observed through mechanical measurements, and are shown in Fig. A.5. The schematics showing the approximate pinning site locations are offered to the right of the respective curves during one section of the magnetization

sweep (+M_X to -M_X). Although the possible pinning of the domain wall with the FIB-line near the clamping point seems to be somewhat consistent, along with the number of pinning transitions with respect to the number of lines, the depinning processes were quite uncontrollable.

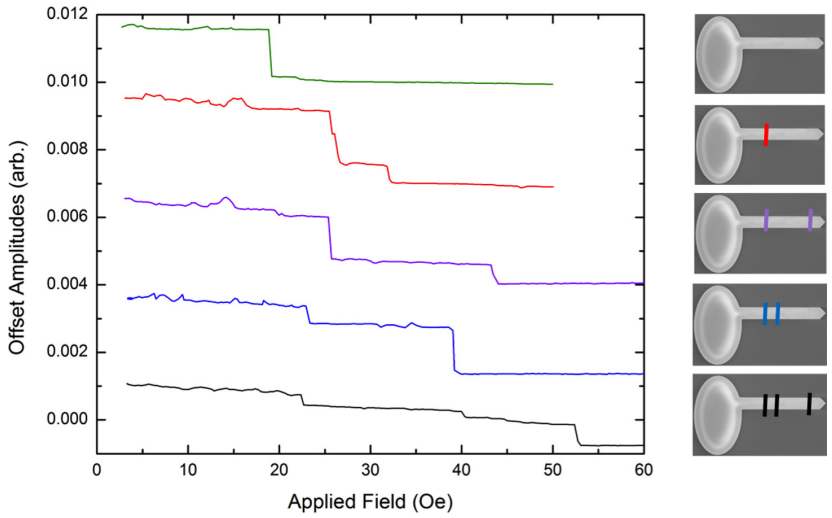

Figure A.5: Mechanical response of cantilevers with pinning sites defined by focused ion beam as the magnetization is switched from one saturated state along the cantilever length to saturation in the polarity. The cantilever diagrams show the approximate locations of the pinning sites.

For multimodal measurements, a simultaneous acquisition of the 1st and 2nd flexural modes (shown in the frequency sweep, Fig. A.6) were done using the MF option of the Zurich lock-in amplifier. Although there is some agreement with the calculated results (Fig. A.2), the response of the relative amplitudes do not appear to approach 0 at the end of the sweep.

There are several reasons why the initial multimodal measurements did not yield quantitative agreement to the deflection model. One is due to the issue of the 2nd flexural mode being much lower in amplitude, creating difficulty in finding an appropriate section on the cantilever for the maximization of signals from both modes. Also, their relative amplitudes are shifted due to the

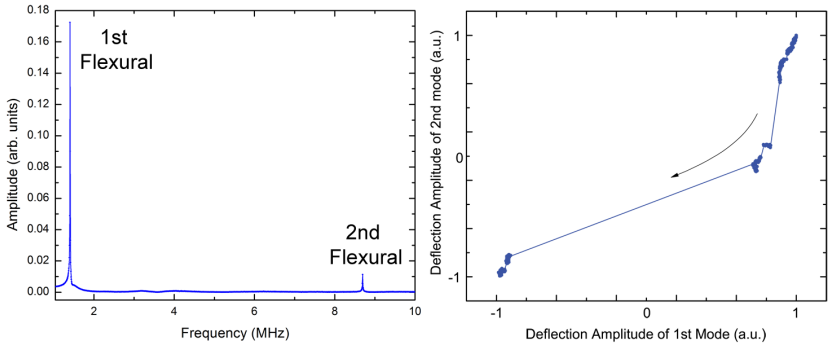

Figure A.6: Frequency response of the first and second flexural modes in a cantilever (left) and the simultaneous response of the 2nd mode plotted against the 1st (right).

fact that our single probe laser cannot measure the highest deflection points along the cantilever for both modes simultaneously. Another issue was the relatively thick films that were deposited on earlier devices, which could likely allow for multi-domain configurations during magnetization reversal (which the deflection model does not account for). Another area of concern was the fact that the permalloy film was deposited across the entire sample substrate, which could cause unwanted coupling between the magnetization of the cantilever and the very large film across the rest of the sample chip. In light of recent discoveries, the correction of the in-plane magnetization signals with the out-of-plane susceptibility (due to the interaction with the driving field) was not taken into account, but become more prevalent in measurements of thicker films. Most of these issues, though, can be and have been remedied, and the multimodal mechanical magnetometry scheme could be an exciting endeavour to revisit.

Bibliography

[1] A. N. Cleland, *Foundations of Nanomechanics - From Solid-State Theory to Device Applicatins* (Springer, Berlin, 2003).

[2] M. V. Salapaka, H. S. Berth, J. Lai, A. Majumdar, E. McFarland, *J. Appl. Phys.* **81**, 2480 (1997).

APPENDIX B

Barkhausen Noise Analysis in YIG

The monocrystalline YIG disk studied in Chapters 5 and 6 has a very pristine structure, and a distinction in its magnetization-versus-field response is the relative absence of Barkhausen-like steps, in comparison to what is observed in polycrystalline materials. It was observed that the degree of pinning experienced by the vortex magnetization due to crystal defects is far below that stemming from polycrystalline defects such as grain boundaries and surface roughness. The numerical calculation of the exchange energy density profile of the YIG disk from the LLG simulation output through the center of the disk is shown in Fig. B.1, where the very high energies in the core exist on the disk surfaces and broaden towards the center plane of the disk.

The vortex core has been shown to be a sensitive probe of magnetization pinning effects [1]. Here, the strength of the pinning is characterized through the fitting of the low-field regions of the hysteresis sweeps, where the magnetization remains in the vortex state and follows a near-linear evolution with external field. This is shown in Fig. B.2 for room and liquid nitrogen temperature measurements, respectively.

The signatures of deviations in the ideal vortex core path (fit to $M = aH + bH^3$, adopting the prediction of the third-order corrected rigid vortex model, [2]) due to pinning effects can be shown by the fit residuals, Fig. B.3. To allow for the

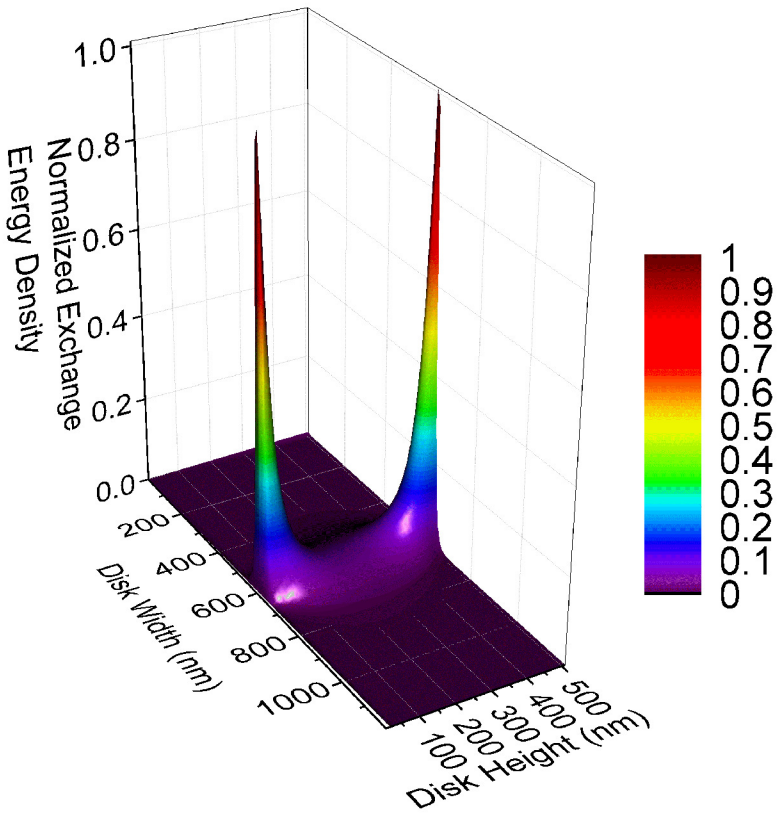

Figure B.1: Normalized exchange energy density in a YIG disk numerically calculated through a plane across the diameter of the disk, from LLG simulation results.

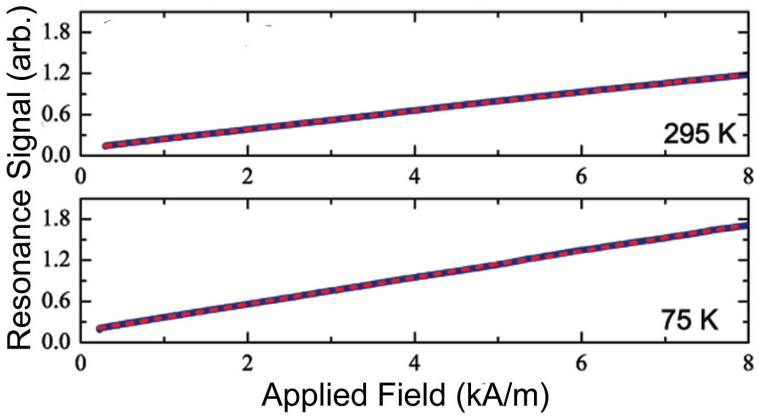

Figure B.2: Low-field magnetization evolution with external field of the YIG disk at room temperature (top) and at 75 K (bottom), fitted to a linear regression.

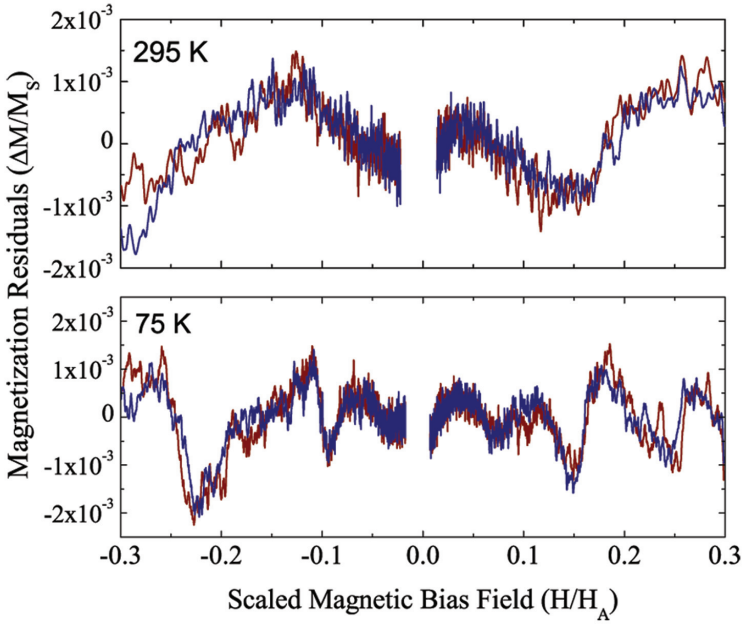

Figure B.3: Room (top, 8x avg) and liquid nitrogen temperature (bottom, 10x avg) magnetization residuals, where the increasing and decreasing magnetic field regions illustrated in Fig. B.2 were fitted individually for both field polarities. The blue trace is for the portion of the increasing field sweep, and the red for the decreasing. The residual amplitude was scaled with the saturation magnetization signal and the field axis was calibrated to the annihilation fields.

intercomparison between the measurements taken at different temperatures, the residual amplitudes were normalized by the saturation magnetization signal and the fields were scaled with the respective vortex annihilation fields, H_A. The individual fitting residuals for both the increasing and decreasing field sweeps across both H_x bias field polarities show the remarkable retracing of features on the order of a tenth of a percent deviation from the model, indicating that the vortex core traverses a similar path for both field directions. A 0.01% residual magnetization corresponds roughly to a magnetic moment ($M_S V$, where M_S=140 kA/m and V is the volume) approaching 10^{-15} Am^2, which is well within the moment sensitivity of the magnetometer [3]. While more bias field dependent features appear in the 75 K trace, the magnetization residuals are of the same order as the room temperature measurement.

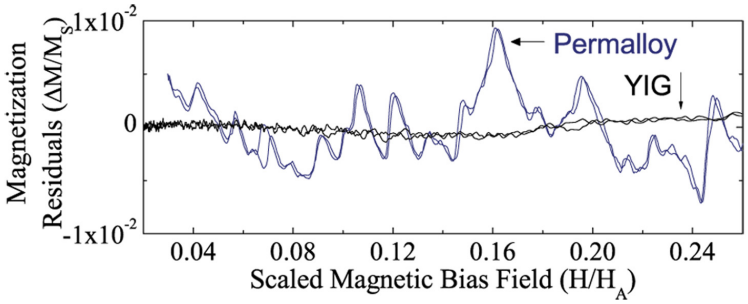

Figure B.4: Room temperature magnetization residuals (for both up and down field sweep regions) of single crystal YIG contrasted with that of polycrystalline permalloy (10x averaged), both measured using similar silicon resonators.

To further extend the discussion of the nature of magnetic Barkhausen-like steps in YIG, a comparison of its room temperature magnetization residuals to that of the polycrystalline micromagnetic permalloy disk studied in Chapter 4, also with a vortex ground state, is presented in Fig. B.4. The smooth, 40 nm thick permalloy ($Fe_{20}Ni_{80}$) disk, with grain sizes of 5-10 nm, was integrated onto a similar nanomechanical resonator via collimated e-beam deposition through a circular shadow mask. The significant contrast shown by the magnetization residuals in permalloy is attributed largely to magnetic pinning

of the vortex core to sites existing at grain boundaries. The crystal structure of both the YIG and permalloy micromagnets were examined by performing selected area electron diffraction with a transmission electron microscope operating at 300 kV (Hitachi HF 3300 FE-TEM). The diffraction pattern of a YIG reference specimen is presented in Fig. 5.2. In contrast, a diffraction signature characteristic of a multi-domain crystal is shown for a 40 nm thick permalloy film, B.5, illustrated by the multiple order of Debye rings.

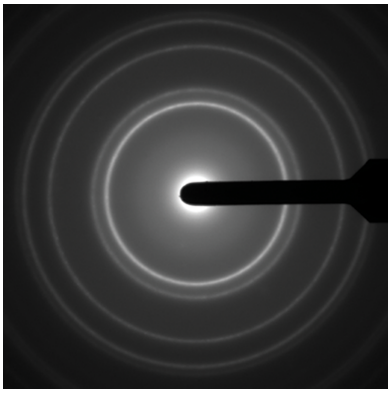

Figure B.5: The selected area electron diffraction pattern is shown for the permalloy element.

Bibliography

[1] J. A. J. Burgess, A. E. Fraser, F. F. Sani, D. Vick, B. D. Hauer, J. P. Davis, M. R. Freeman, *Science* **339**, 1051 (2013).

[2] J. A. J. Burgess, D. C. Fortin, J. E. Losby, D. Grombacher, J. P. Davis, M. R. Freeman, *Phys. Rev. B* **82**, 144403 (2010).

[3] J. Losby, J. A. J. Burgess, Z. Diao, D. C. Fortin, W. K. Hiebert, M. R. Freeman, *J. Appl. Phys.* **111**, 07D305 (2012).

APPENDIX C

Nanofabrication Methods and Recipes

This Appendix section contains processing recipes that have been developed or improved for the fabrication of the torque magnetometers used in this Thesis. It is intended to benefit future users, as nanofabrication development is a lengthy (and often a trial-and-error-based) process.

C.1 Selection and Cleaning of Substrates

For the resonators fabricated in this Thesis, the silicon-on-insulator (SOI) architecture provides an ideal starting point. The triple-layered structure is comprised of thick (handle or substrate) and very-thin (device) Si layers that sandwich a SiO_X (buried oxide or sacrificial) layer. The sacrificial oxide layer is often etched away to release structures defined in the device layer. Unfortunately, SOI wafers with thin device layers (less than 300 nm) are extremely expensive, due to proprietary technological processes for their fabrication, high demand from the semiconductor industry, and due to greater than 80% of the current market share being controlled by one entity. The demand is continuing to rise with the popularity of on-chip photonic and optomechanical devices, where SOI adapts very well. As of the writing of this thesis, there is plenty of SOI in stock with various device layer thicknesses to last a few more years.

Wafers should be diced to appropriate dimensions. A hot piranha clean (3:1 H_2SO_4:H_2O_2) is preferred over acetone sonication for the cleaning of substrates and should be done prior (within a week) to electron beam resist spinning. Substrates should also be heated on a 150° C hot plate for 2 minutes to remove any moisture prior to the spinning of any resist.

C.2 Focused Ion Beam Milling of Nanomechanical Resonators

The focused ion beam (FIB) is a powerful tool for the fabrication of nanomechanical resonators. For the devices presented in this thesis this was done either through direct Ga^+ ion milling of structures into silicon nitride membranes or thin permalloy films, where the former holds a thin magnetic film. Also within the FIB instrument is a nanomanipulator (see Fig. C.1) which allows for the transfer of magnetic material onto prefabricated resonators, which is beneficial for processes that are not compatible with standard lithographic techniques (this procedure was described in Chapter 5). The general description of the FIB process is given in Chapter 2.2.2.

C.2.1 Silicon Nitride Cantilevers

Commercially available low-stress silicon nitride (SiN) membranes, most often used as sample holders in TEM or x-ray spectroscopy, have very exceptional mechanical and optical properties [1, 2] which make them ideal candidates for resonators. Prior to FIB exposure a 30 to 50 nm thick layer of permalloy was deposited on the flat ('membrane') side of the window (Norcada TA301C, the square windows are 100 nm thick with an area of 100 $\times$ 100 μm^2). A thin carbon film (3-5 nm) was then deposited the other side of the window, where the FIB is incident, in order to prevent charging effects. The reason for the permalloy being on the other side of the membrane normal to the FIB milling direction is to prevent excessive ion damage to the magnetic film.

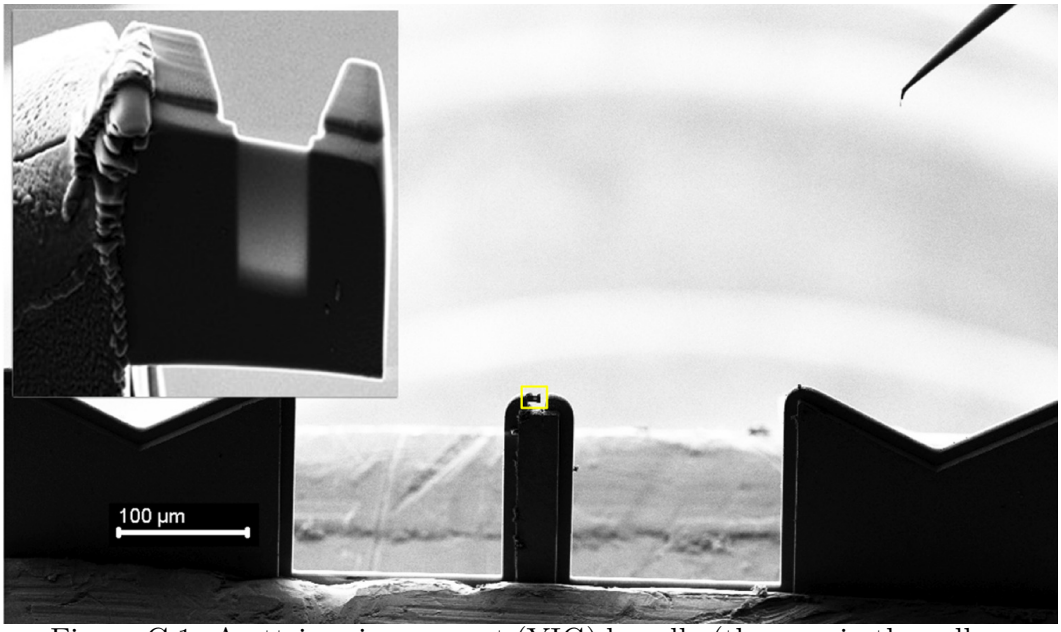

Figure C.1: A yttrium iron garnet (YIG) lamella (the area in the yellow square is expanded in the top left inset) after attachment to a TEM sample-holding finger using the nanomanipulator (top right of image). The lamella was thinned to 250 nm to allow for TEM diffraction measurements (see Chapter 5).

Before the milling procedure, the FIB and SEM columns were aligned to the SiN window through the use of fiducial markers (a 'burn spot' or other feature). Three rectangles were milled to fabricate a cantilever beam: two on each side of the beam and another along the free end to release it. The cantilever was clamped to the rigid silicon frame of the window to minimize clamping losses. The *Mill for Depth* mode was selected in the FIB control software (Raith ELPHY Quantum) for the milling of the rectangular areas with the parameters (others set to default): *Depth*=0.6 μm, *Layers*=1, *Material*=Si, *Milling Current*=30 kV:80 pA. In order to 'clean up' the cantilever, the FIB was narrowly raster scanned along its edges at a milling current of 300 pA. After the FIB procedure, the window is attached to a reflective surface (such as a Si chip) with the 'membrane side' of the window closest to the mirror in order to create an interferometric cavity. Some representative devices are

shown in Fig. C.2.

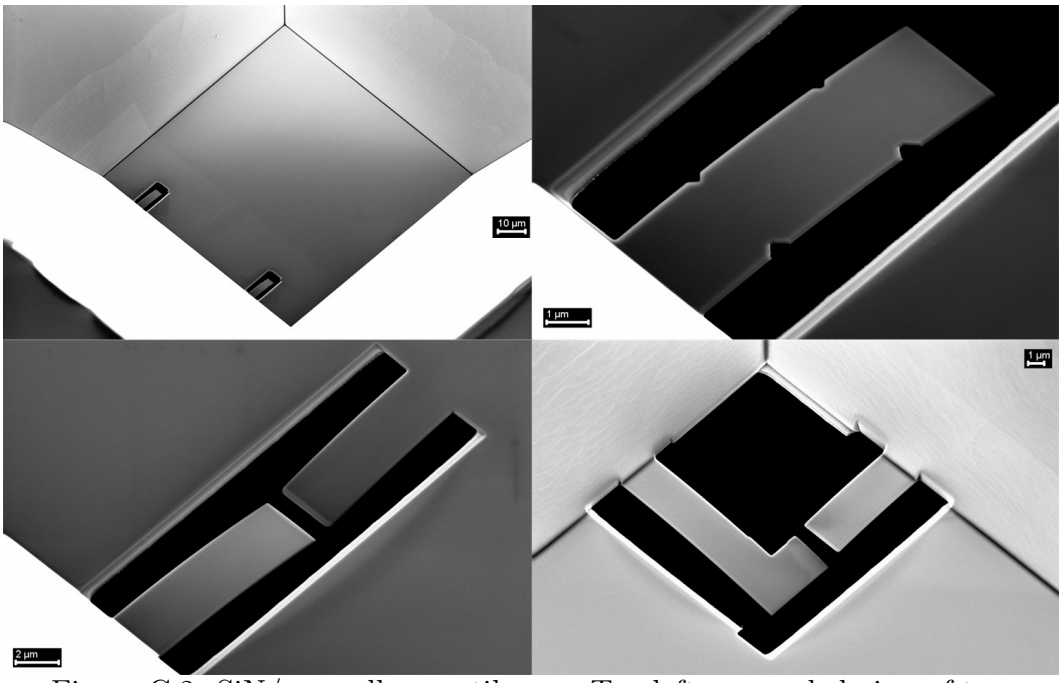

Figure C.2: SiN/permalloy cantilevers. Top left: expanded view of two cantilevers within a square SiN membrane. Geometric notches were were added to the cantilever in the top right to act as magnetic domain wall pinning sites. Bottom left: double cantilever geometry for the coupling of flexural vibrational modes. Bottom right: torsional and flexural cantilevers.

C.3 Electron Beam Lithography Recipes

Although the EBL recipes presented here have been developed and tested through the fabrication of many devices (some representatively shown in Fig. C.3). It is recommended that users always perform a dose-test prior to beginning a new EBL project. Some resists are highly sensitive to atmospheric exposure and aging which will change exposure parameters. The following recipes should be a good starting point, and are listed by resist type.

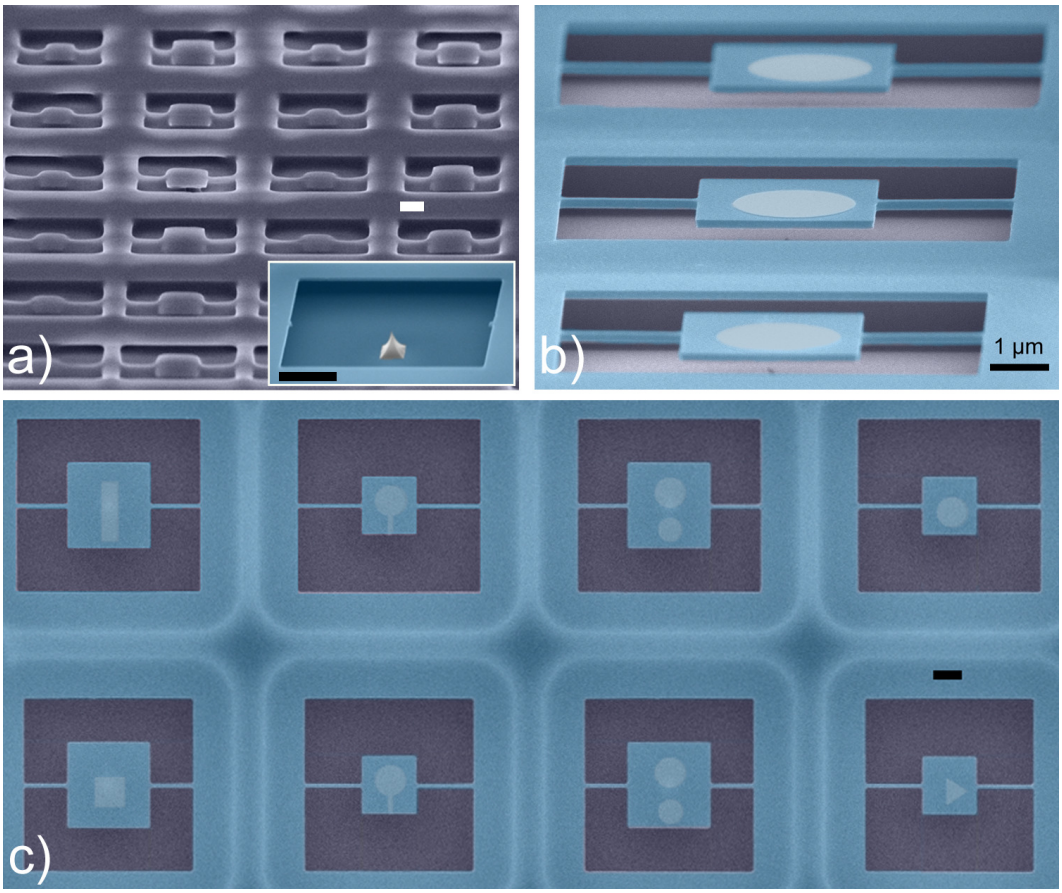

Figure C.3: Fabrication of an array of nanomechanical magnetometers using a two step EBL and liftoff process [3]. (a) Tilted view SEM image of a sample surface covered with PMMA resist after the first EBL process for defining the resonators. The inset is a false coloured SEM image of a pyramidal shaped pillar left intentionally in the buried oxide layer to serve as an inverted dimple, taken after the torsional paddle was removed. (b) False coloured tilted view SEM image of a set of three nanomechanical torque magnetometers with 2 μm diameter disks on them. (c) False coloured top-view SEM image of an array of nanomechanical torque magnetometers. All scale bars are 1 μm.

Hydrogen Silsesquioxane (HSQ)

HSQ, a negative-tone resist, can currently produce the highest resolution linewidths (sub-10 nm, with skill) owed to the relatively small molecular structure. HSQ is a polymeric inorganic resist, where Si-H bonds are scissored and Si-O-Si bonds are created upon e-beam exposure. The patterned resist is amorphous SiO_X, and can easily be removed during the hydroflouric acid-based etching step used to release the resonator. The resist is also popular in on-chip Si-based photonic device fabrication, as the exposed resist forms an ideal cladding due to the index of refraction contrast between Si and SiO_X. HSQ is currently sold by Dow-Corning Corporation (as XR-1541) through subsidiary chemical distributors, and is among the most expensive of e-beam resists.

HSQ has a very short processing window (the period of time between resist spinning and e-beam exposure) due to it readily absorbing water from the atmosphere. It is recommended that resist spinning be done just prior to the EBL session. The resist should be stored in a (dark) chemical freezer and warmed up to room temperature prior to spinning. The shelf life is short (about six months) and performance will degrade very rapidly afterwards. The resist sensitivity is also relatively low, requiring higher exposure doses compared to other types of resists (i.e., longer write times).

HSQ can be diluted (in order to tune the resist thickness) with methyl isobutyl ketone (MIBK) in approximately a 1:1 ratio. A 2% solution of HSQ yields approximately a 70 nm thick resist layer with the following spinning parameters:

1. Spin coating spread step: 100 rpm, acceleration=1 s and time= 1 s
2. Spinning step: 4000 rpm, acceleration= 2 s and time = 30 s
3. Bake on hot plate at 150° for 5 min
4. EBL exposure: 10 kV acceleration voltage, 10 μm aperture, 350-500 $\mu C/cm^2$ dosage, 10 nm step size

5. Development: Slowly swirl substrate for 60 s in 25 % tetramethylammonium hydroxide (TMAH) then rinse for 3 min in DIH_2O
6. Blow dry the substrates

Polymethyl Methacrylate (PMMA)

PMMA is the 'classic' positive-tone, organic, EBL resist with very high contrast and resolution (comparable to that of HSQ). The processing window for PMMA can be over many days and the clearing dose is generally lower compared to that of many types of resists. The etch selectivity (the ability to withstand the etchant compared to that of what material is being etched) of PMMA is relatively poor. PMMA can be purchased in a variety of molecular weights, which determine the clearing dose necessary for adequate scission of polymer chains. The two popular types are PMMA 950A (950 kD in anisole) and 495A (495kD in anisole), and both can be layered for performing lift-off techniques.

1. Spin coating spread step: 500 rpm, acceleration=2 s and time= 5 s
2. Spinning step: 4000 rpm, acceleration= 5 s and time = 30 s (thickness will be approximately 150 nm for PMMA 950A)
3. Bake at 200° for 20-30 min.
4. If a bi-layer resist is desired, first spin and bake PMMA 495A using the first three steps. Repeat with PMMA 950A
5. EBL exposure: 10 kV acceleration voltage, 10 μm aperture, 80-140 $\mu C/cm^2$ dosage, 10 nm step size
6. Development: Slowly swirl substrate for 60 s in 1:3 MIBK/IPA (isopropyl alcohol), 20 s in IPA, then rinse for 20 s dH_2O
7. Blow dry the substrates

Exposed PMMA can be removed in acetone or in an N-Methyl-2-pyrrolidone (NMP) bath at 70-80°. A de-scum process in a reactive ion etcher using an oxygen plasma is also an option (67 mTorr pressure, 20% oxygen flow, 150 W RF power, time=6 s).

If doing a lift-off of a deposited metallic film, soak the substrates in acetone or NMP until the film appears to be removed after inspection under an optical microscope. Ultrasonication is not recommended, as the deposited material will likely be removed without a strong enough adhesion layer.

ZEP 520

ZEP 520 (Zeon Corp., Tokyo) is a positive-tone resist with similar applications and resolution to that of PMMA, but has the advantages of having a higher etch resistance (by approximately 5x) and a lower clearing dose (ie. faster exposure times). The line edge roughness is slightly larger than PMMA, and can be reduced using cold development methods. ZEP 520 is usually diluted in anisole (labeled ZEP 520A) in a 1:1 ratio.

1. Spin coating spread step: 500 rpm, acceleration=2 s and time= 5 s
2. Spinning step: 4000 rpm, acceleration= 5 s and time = 45 s (thickness will be approximately 120 nm)
3. Post-spin bake at 180° C for 2 min.
4. EBL exposure: 15 kV acceleration voltage, 10 μm aperture, 25-35 μC/cm^2 dosage, 10 nm step size
5. Development: Slowly swirl substrate in ZED N50 for 90 s and stop development in 9:1 MIBK/IPA for 10 s
6. Blow dry the substrates

Developed ZEP 520A can be removed in an N-Methyl-2-pyrrolidone (NMP) bath at 70-80°.

SU-8

SU-8, an epoxy-based negative-tone resist, was used more extensively in the past but has been replaced (in our case), for nearly all negative-resist-based processes by HSQ. SU-8 is very sensitive to exposure, and thus minor processing variations can alter results significantly. It also has relatively low resolution (approx. 100 nm) and is difficult to remove. It also requires a post-development bake. SU-8 does have advantages due to being bio-compatible, and its very low clearing dose helps to preserve biological material. It is also relatively inexpensive.

1. Spin coating spread step: 500 rpm, acceleration=2 s and time= 3 s
2. Spinning step: 3000 rpm, acceleration= 2 s and time = 30 s
3. Post-spin bake at 95° C for 1 min.
4. EBL exposure: 2 kV acceleration volrage, 10 μm aperture, 2-5 μC/cm^2 dosage, 10 nm step size
5. Postbake - 1 min at 60° C and 3 min at 160° C
6. Development: Slowly swirl substrate for 30 s in SU-8 Developer and then stop development in IPA for about 10 s.

Developed SU-8 can be removed using an oxygen plasma (60 mTorr pressure, 75 W RF power, 15% O_2 flow) with an etch rate of around 2 nm/s.

C.3.1 Dry Si Etching

After EBL patterning and development of the e-beam resist, the device layer must be etched to define the mechanical resonators. A state-of-the-art method is through the use of an inductively coupled plasma - reactive ion etch (ICP-RIE). This system is configured to allow for fast and deep etching of Si features

with high aspect ratios. As the process has a very high selectivity of Si, most common e-beam resists (and SiO_2) can be used to etch the SOI device layer with nearly vertical sidewalls. Metallic masks are generally not recommended as resputtered metal species can cause micromasking, significantly slowing down the etch.

The Advanced Silicon Etch (ASE) process consists of alternating etching (using sulfur hexaflouride, SF_6) and passivation (of octoflourocyclobutane, C_4F_8) cycles, where a protective polymer is deposited in the latter. During the etch cycle, the plasma of reactive ions is inductively coupled at 13.56 MHz to a coil assembly. The sample chuck is biased at a lower frequency (hundreds of kHz) and allows for control of the ion density (lower frequency allows for ions to escape trenches) and energy as the ions are accelerated towards the sample being etched.

The STS ICPRIE available at the University of Alberta Nanofab has two recipes available for the etching of SOI device layers that are less than 25 μm thick (*precisio* and *prcnprl*). Both recipes are similar, with slightly modified gas concentrations. It is not recommended to alter any recipes, unless by an experienced user. The general ICP-RIE process parameters for the passivation step is 60-100 standard cubic centimeters per minute (sccm) C_4F_8, 15-20 mTorr pressure, 600 W coil power, 0 W bias power, and no bias frequency. For the etching cycle, 80-150 sccm of SF_6 is used with 20 mTorr pressure, 600 W coil power, 20 W bias power, 13.56 MHz bias frequency, and 380 kHz platen (at sample) bias frequency. The etch rate is approximately the same for both processes, around 20 nm/s, though the etch process is not initially linear (likely due to the forming of a native oxide layer or slight contaminants on the device layer). Generally 20 seconds is sufficient for 150 nm thick device layers. It is also crucial to have adequate thermal contact of the sample chip being etched with the handle wafer, as wafer heating can significantly affect the etch process. Usually, after the completion of the ICP-RIE process, a visual inspection will give a good idea of whether or not all of the device layer has been etched as the reflective properties will change. This will be more evident with negative

resists, since most of the Si on the chip will be etched away (for 150 nm device, 1 μm oxide layers the device will appear as dark green from blue if the etch was successful). It is recommended that a chamber conditioning (cleaning) process be done before every ICP-RIE process.

C.3.2 Device Release and Drying

Upon completion of the Si dry etch, the devices must be released. This is generally done through wet-etching of the SiO_2 using a commercially available buffered oxide etch (BOE) solution, which is concentrated hydroflouric acid (HF, 49% in water) and ammonium biflouride (NH_4F, 40% in water), balanced to have a 1:6-10 ratio for each, respectively. The etch rate is approximately 55 nm/s for the BOE with a 1:10 ratio. The devices are usually placed upside down in the solution while gently stirring during the last 30 seconds using the tweezers holding the device. Timing is crucial, as the anisotropic nature of the etch will cause the undercutting of the device supports which can lead to degraded device performance (quality factor reduction). A rough estimate of the total etch time is that needed to release half of the device (along a symmetry axis where the etching can equally occur from both sides), for example half the width of a cantilever. The addition of sacrificial (free, unsupported) structures of the same dimensions as what is to be released can be added to the EBL design, to offer confirmation (if they are completely removed after the oxide etch) that the devices are released. When the etching period is over, the etch must be stopped by immersing the sample in (preferably) a succession of two beakers containing dH_2O. The devices should then carefully be transferred to IPA for the drying step.

A crucial step is the drying of the devices post-release, as the viscous forces and surface tensions present between the released structures and the substrates will cause the devices to collapse (and stiction to the substrate) if attempting to dry with a blow gun or hot plate. Two methods are generally used for sample dehydration: critical point drying or a pentane-based release. In

the former, the critical point dryer can control the temperature and pressure of the IPA-liquid CO_2 mixture to bring it to the critical point where, in the phase diagram, a direct conversion of the mixture to gas is possible. The critical point dryer in the U of A Nanofab is generally a single-button operation system. In the pentane-release, the IPA containing the released devices is slowly replaced with rapidly drying pentane. This can be done using successive beakers with 100% IPA, 70%/30% IPA/Pentane, 50%/50% IPA/Pentane, 30%/70% IPA/Pentane, and 100% Pentane. It is also fine to use two beakers, one with 100% IPA that is slowly mixed with pentane at the appropriate ratios and another beaker with 100% pentane. After removal from the pentane, a very gentle blow gun-drying of the devices will quickly remove the solvent preventing stiction.

C.3.3 Additional Resources

1. The University of Alberta Nanofab Resource Library
2. The process for stiction-free fabrication of nanomechanical resonators holding magnetic thin film elements (Fig. C.3) is offered in [3].
3. An extensive list of etch rates of 53 materials and etchants (a total of 620 combination) is available in [4].
4. The MEMS Handbook contains three books of extensive micro- and nanofabrication information [5].

Bibliography

[1] Y. Toivola, J. Thurn, R. F. Cook, G. Cibuzar, K. Roberts, *J. Appl. Phys.* **94**, 6915 (2003).

[2] B. M. Zwickl, W. E. Shanks, A. M. Jayich, C. Yang, A. C. B. Jayich, J. D. Thompson, J. G. E. Harris, *Applied Physics Letters* **92**, 103125 (2008).

[3] Z. Diao, J. E. Losby, J. A. J. Burgess, V. T. K. Sauer, W. K. Hiebert, M. R. Freeman, *J. Vac. Sci. B* **31**, 051805 (2013).

[4] K. R. Williams, K. Rupta, M. Wasilik, *J. Microelectromech. Syst.* **12**, 761 (2003).

[5] M. G. el Hak, *The MEMS Handbook* (CRC Press, 2010).

APPENDIX D

Optical Interferometry

Optics-based sensing has been successful in measuring the minute displacements of micromechanical devices. The use of a monochromatic light source (usually a laser) in a free-space or fibre-optics based instrument setup provides many advantages. It is generally a non-invasive way to probe the devices, while also allowing for broadband response. The noise introduced by the laser can be accounted for and subtracted from a reference laser beam. The wave nature of light also allows for optical interferometry, where the interference of light due to their relative phase differences allows for sub-nm motion detection.

The propagation of an electromagnetic wave can be described by the wave equation,

$$\nabla \mathbf{u} = c^2 \nabla \mathbf{u}^2 \tag{D.1}$$

where the wavefunction $\mathbf{u} = u(x, y, z; t)$ is both spatial and time dependent and c is the propagation speed of the wave in a medium. Defining the propagation direction along the z-axis (orthogonal and out of plane to the surface of the mechanical oscillator), the solution of the second order partial differential equation is in the form of a harmonic wave,

$$u(z, t) = \sqrt{I(z, t)} \cos(\omega t - \phi(z)) \tag{D.2}$$

with a defined intensity $\sqrt{I}$, angular frequency $\omega = 2\pi f$, and phase ϕ. When

combining waves, the complex form is often advantageous to use:

$$U(z,t) = \sqrt{I}e^{i(\omega t - kz)}, \tag{D.3}$$

where $k = 2\pi/\lambda$ is the wave number, λ is the wavelength of the monochromatic light. In optical measurements the photoreceiver collecting the signal is sensitive to the light intensity, which in our case is collected over the area of a photodiode and measured in W/m^2. This intensity is generally defined as the square of the complex wavefunction, where the time-dependence can be neglected as the intensity is averaged over a time period longer than that of the optical period,

$$I(z) = |U(z)|^2 = U(z)U^*(z). \tag{D.4}$$

Solving for the superposition of two waves, $U_1(z)$ and $U_2(z)$ yields,

$$\begin{aligned} I(z) &= |U_1(z) + U_2(z)|^2 \\ &= (U_1(z) + U_2(z)) + (U_1^*(z) + U_2^*(z)) \\ &= U_1(z)^2 + U_2(z)^2 + U_1^*(z)U_2(z) + U_1(z)U_2^*(z) \\ &= I_1 + I_2 + 2\sqrt{I_1 I_2}\cos(\delta\phi). \end{aligned}$$

The intensity is dependent on $\delta\phi$, the phase difference between the two waves, which forms the basis for interferometric measurements. Our measurement scheme involves the use of an optical cavity between the oscillating structure and a reflective substrate to introduce a phase contrast. The beam-splitting occurs as the focused laser from a microscope objective reflects off two (or more) surfaces, forming what is known as a FabryPerot interferometer. This optical path difference of the reflected light introduces the phase difference, of which the total intensity is dependent. $\delta\phi = kd_1 - kd_2 = (2\pi n/\lambda)(d_1 - d_2)$ with the assumption that both waves are traveling through the same medium and $d_1 - d_2$ is the path difference. Thus, the optical cavity distance should be tuned to offer the optimum constructive interference based on the wavelength of the laser.

Finite difference time domain simulations were done (Lumerical FDTD soft-

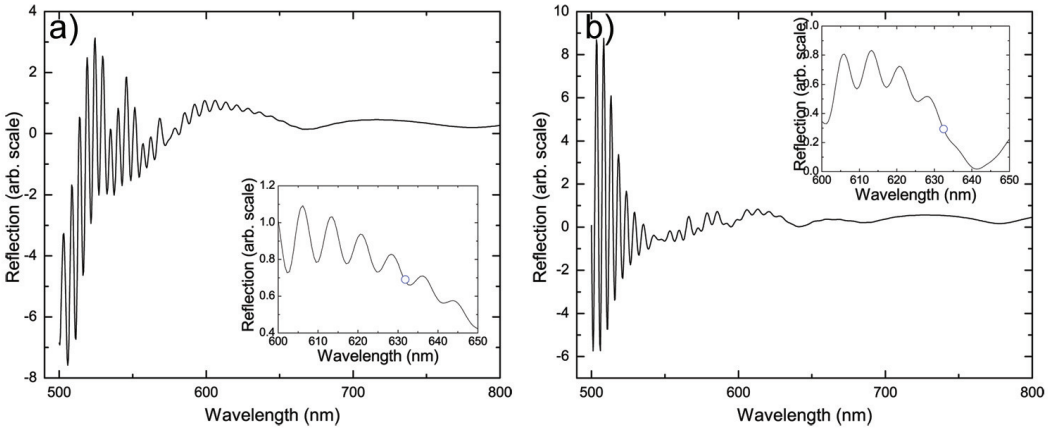

Figure D.1: Finite difference time domain simulations of reflective coefficients for resonators fabricated from SOI wafers with a) 145 nm and b) 300 nm device layers using a 632 nm laser source. In the insets are zoom-ins around the region near the laser source wavelength, indicated by a circle. A maximum slope ensures optimum detection sensitivity of displacement

ware) to calculate the wavelength dependence of the reflection coefficient from devices fabricated from the SOI architecture, Fig. D.1. The released resonator and the surrounding substrate formed the computational domain while the grid size was 10 nm. Silicon was selected as the dielectric material for both the resonator and substrate, with an air gap of 1000 nm. The resonator thicknesses chosen were 145 and 300 nm, according to the SOI specifications. Default software parameters were used for the values of the permittivity, conductance, and permeability of the materials. For the optimum modulation of the reflected intensity, it is ideal to use a wavelength of light that resides on sections of the curve with the highest slope.

APPENDIX E

List of Publications

1. J.E. Losby, Z. Diao, F. Fani Sani, D.T. Grandmont, L.C. Parsons, J.A.J. Burgess, T. Firdous, M. Below, W.K. Hiebert, and M.R. Freeman, *Nanomechanical Detection of Three-dimensional Magnetization in a Single-crystal Yttrium Iron Garnet Disk*, (In preparation, 2013).

2. F. Fani Sani, J.E. Losby, Z. Diao, L.C. Parsons, J.A.J. Burgess, D. Vick, W.K. Hiebert, and M.R. Freeman, *Strong Vortex Core Pinning and Barkhausen-free Magnetization Response in Thin Permalloy Disks Induced by Implantation of* 1×10^4 *Ga Ions*, (Accepted: *Proceedings of MMM, J. Appl. Phys*, 2014).

3. J. Losby, Z. Diao, F. Fani Sani, D.T. Grandmont, J.A.J. Burgess, W.K. Hiebert, and M.R. Freeman, *Nanomechanical AC Susceptometry of an Individual Mesoscopic Ferrimagnet*, (Accepted: *Solid State Commun. SI: Spin Mechanics*, 2013).

4. Z. Diao, J.E. Losby, J.A.J. Burgess, V.T.K. Sauer, W.K. Hiebert, M.R. Freeman, *J. Vac. Sci. B* **31**, 051805 (2013).

5. Z. Diao, J.E. Losby, V.T.K. Sauer, J.N. Westwood, M.R. Freeman, and W.K. Hiebert, *Appl. Phys. Express* **6**, 065202 (2013).

6. J.A.J. Burgess, J.E. Losby, and M.R. Freeman *A Deformable Model for Magnetic Vortex Pinning*, (In review: *J. Magn. Magn. Mater.*, 2013).

7. J. Losby, J.A.J. Burgess, Z. Diao, D.C. Fortin, W.K. Hiebert, and M.R. Freeman, *J. Appl. Phys.* **111**, 07D305 (2012).

8. J. Losby, J.A.J. Burgess, C.M.B. Holt, J.N. Westwood, D. Mitlin, W.K. Hiebert, and M.R. Freeman, *J. Appl. Phys.* **108**, 123910 (2010). Also in *Virtual Journal of Nanoscale Science and Technology* **23**, (2011).

9. J.A.J. Burgess, D.C. Fortin, J. Losby, D. Grombacher, J.P. Davis, M.R. Freeman, *Phys. Rev. B.* **82**, 144403 (2010).

10. N. Liu, F. Giesen, M. Belov, J. Losby, J. Moroz, A. E. Fraser, G. McKinnon, T.J. Clement, V. Sauer, W.K. Hiebert, and M.R. Freeman, *Nature Nanotechnol.* **3**, 715 (2008).